Diss. ETH No. 16261

Complex Multiphase Materials: Microstructure Characterization and Finite Element Property Predictions

DISSERTATION

submitted to the

EIDGENÖSSISCHE TECHNISCHE HOCHSCHULE ZÜRICH

for the degree of

DOCTOR OF SCIENCES

presented by

MARTIN HEGGLI

Dipl. Werkstoff-Ingenieur, ETH Zürich
born 28.09.1973
citizen of Luzern and Müswangen (LU)

accepted on the recommendation of
PD Dr. Andrei A. Gusev, examiner
Prof. Dr. Ulrich W. Suter, co-examiner
Prof. Dr. Hans Christian Öttinger, co-examiner

Zürich, 2005

Contents

Abstract

In the first part of this thesis short fibre reinforced polymer composites have been studied as examples for composites containing particulate inclusions. The 3D fibre orientation state was measured and computer models representing the real microstructure of the material were generated. It was demonstrated that with the finite element method (FEM) used very accurate predictions of the effective elastic properties of these composites are possible.

The widely used in industry micromechanical models of Halpin-Tsai and Tandon-Weng for unidirectional composites were compared to accurate direct numerical predictions. It was shown that the Tandon-Weng approach gives relatively better predictions. However, the accuracy of both models was demonstrated to be not sufficient.

It was shown that the effect of arbitrary fibre orientation states, which can be described by a series of orientation tensors, can be taken into account by orientation averaging of results obtained by direct numerical predictions for unidirectional composites. Comparison with direct numerical predictions for the arbitrary fibre orientation state demonstrated the relatively good accuracy of the orientationally averaged predictions.

In the second part of this work, two different composite materials with complex interpenetrating microstructures have been studied: a melt processed composite of 50 vol.-% low density polyethylene with 50 vol.-% phosphate glass and a porous graphite infiltrated with approximately 15 vol.-% of an aluminium alloy.

The microstructure of both materials has been measured with X-ray microtomography. The resulting images were segmented to discriminate the different phases of the composite. The three-dimensional tomography information has been used to directly build 3-D finite element models. Linear brick elements have been used. Effective materials properties have been calculated by a finite element method (FEM).

The effective electrical conductivity of the low density polyethylene/phosphate glass composites has been calculated as a test for the continuity of the two phases. It was found that both phases are continuous.

Numerically calculated elastic properties are within the rigorous Hashin-Shtrikman variational bounds. However, the experimentally measured stiffness is much smaller. By studying local stresses that develop inside the structure during cooling from production temperature to room temperature in a small

but significant number of elements relatively high tensile stresses were found. This effect probably introduces damage in the stiff glass phase which results in a lower than expected stiffness of the composite and in its high brittleness.

In the graphite/aluminium composites it was found that the representative volume element for the electrical conductivity is very large. However, by calculating an ensemble average over a number of subvolumes accurate predictions for the overall electrical conductivity could be made. By doing this, relatively small models ($100 \times 100 \times 100$ voxels) were sufficient to get accurate results. Therefore computing time could be kept relatively short.

An experimentally observed decrease in the electrical conductivity after a cyclic thermal treatment could be reproduced in the simulation to some extent. By filling the pores in the model of the thermally treated sample it was shown that pores inside the conducting aluminium channels are responsible for the drop in the electrical conductivity.

The numerically predicted Young's modulus was smaller than the measured values. A series of model calculations showed that the numerical results are reasonable. It remains unclear why the measured stiffness is this high, as a matter of fact far above the Hashin-Shtrikman variational bound. Possibly, the materials parameters that were used for the calculations could not be determined accurately enough.

Thermal conductivity and thermal expansion coefficient of the graphite/aluminium composite have also been calculated. They were in relatively good accordance with the experimental results.

Zusammenfassung

Im ersten Teil dieser Arbeit wurden Kurzfaser-verstärkte Polymer Komposite als ein Beispiel für Verbundwerkstoffe mit partikelförmigen Einschlüssen untersucht. Der dreidimensionale Orientierungszustand der Fasern wurde gemessen und Computer-Modelle erzeugt, die repräsentativ für die reale Mikrostruktur des Materials sind. Es wurde gezeigt, dass mit der benutzten Finite Element Methode (FEM) sehr präzise Voraussagen über die effektive elastischen Eigenschaften des Verbunds gemacht werden können.

Die beiden in der Industrie oft verwendeten mikromechanischen Modelle von Halpin-Tsai und Tandon-Weng für unidirektionale Komposite wurden mit präzisen direkten, numerischen Voraussagen verglichen. Es wurde gezeigt, dass der Tandon-Weng Ansatz relativ bessere Voraussagen macht. Allerdings wurde auch gezeigt, dass beide Modelle nicht ausreichend genaue Ergebnisse liefern.

Es wurde gezeigt, dass der Einfluss von beliebigen Faserorientierungszuständen, wie sie durch eine Reihe von Orientierungstensoren beschrieben werden können, mit Hilfe einer Orientierungsmittelung berücksichtigt werden können, indem die Ergebnisse der direkten numerischen Voraussagen für unidirektionale Komposite über die Orientierung gemittelt werden. Der Vergleich mit direkten numerischen Voraussagen für die Strukturen mit einem beliebigen Orientierungszustand hat die relaiv gute Genauigkeit der mittels Orientierungsmittelung erhaltenen Voraussagen gezeigt.

Im zweiten Teil dieser Arbeit wurden zwei verschiedene Verbundwerkstoffe mit komplexer interpenetrierender Mikrostruktur untersucht: ein aus der Schmelze verarbeiteter Verbund von 50 vol.-% Polyethylen (LDPE) mit 50 vol.-% Phosphatglas und ein poröser Graphit, der mit ungefähr 15 vol.-% einer Aluminium-Legierung infiltriert ist.

Die Mikrostruktur der beiden Materialien wurde mittels Röntgen-Mikrotomographie abgebildet. Die erhaltenen Schnittbilder wurden segmentiert, um die verschiedenen Phasen des Verbunds zu trennen. Die dreidimensionale tomographische Information wurde dann dazu verwendet, direkt 3-D Computer Modelle zu erzeugen. Die effektiven Eigenschaften der Komposite wurden mit einer Finite Element Methode (FEM) berechnet.

Die effektive elektrische Leitfähigkeit des Polyethylen/Phosphatglas Verbundes wurde berechnet, um die Kontinuität der beiden Phasen zu testen. Es hat sich gezeigt, dass beide Phasen kontinuierlich sind.

Die numerisch berechneten elastischen Eigenschaften liegen innerhalb der

strengen Hashin-Shtrikman Grenzen. Die experimentell gemessene Steifigkeit hingegen ist deutlich kleiner. Die Berechnung der lokalen thermischen Spannungen, die beim Abkühlen von der Herstell- zu Zimmertemperatur auf gebaut werden, zeigte dass in einer kleinen aber signifikanten Zahl von Elementen relativ hohe Spannungen auftreten. Wahrscheinlich führen diese zu Schädigungen in der steiferen Glas-Phase, was zu einer Komposit-Steifigkeit, die kleiner als erwartet ist, und zu einer grossen Sprödigkeit führt.

Für die Graphit/Aluminium Komposite wurde festgestellt, dass das repräsentative Volumenenlement für die elektrische Leitfähigkeit sehr gross ist. Andererseits konnten durch die Berechnung von Ensemble-Mittelwerten von einer Anzahl Subvolumen zutreffende Voraussagen für die effektive elektrische Leitfähigkeit gemacht werden. Es war daher ausreichend, Berechnung mit relativ kleinen Modellen ($100 \times 100 \times 100$ Voxel) zu machen, um korrekte Ergebnisse zu erhalten. Die benötigte Rechenzeit konnte daher relativ kurz gehalten werden.

Die experimentell beobachtete Abnahme der elektrischen Leitfähigkeit nach einer zyklischen Wärmebehandlung konnte in der Simulation bis zu einem gewissen Grad reproduziert werden. Durch das Auffüllen der Poren in der wärmebehandelten Probe konnte gezeigt werden, dass Poren in den leitenden Aluminiumkanälen für die Abnahme der elektrischen Leitfähigkeit verantwortlich sind.

Der numerisch vorausgesagte Elastizitäts-Modul war deutlich kleiner als die gemessenen Werte. Eine Reihe von Modellrechnungen hat gezeigt, dass die numerischen Ergebnisse vernünftig sind. Es bleibt unklar, warum die gemessene Steifigkeit so gross ist, nämlich sogar deutlich grösser als die obere Hashin-Shtrikman Grenze. Möglicherweise konnten die Materialparameter, die für die Berechnung verwendet wurden, nicht genügend genau bestimmt werden.

Die Wärmeleitfähigkeit und der Wärmeausdehnungskoeffizient der Graphit/Aluminium-Komposite wurde berechnet. Sie stimmten gut mit den experimentell gemessenen Werten überein.

1 Introduction

Numerical prediction of the effective properties of composite materials has become increasingly popular and has found more and more widespread application during recent years. For particulate composites with inclusions such as spheres, fibres, or platelets a finite element method (FEM) to predict their properties has been developed in recent years. [1–3] The method uses a biased Monte Carlo method to generate 3D computer models of particulate composites (i.e. containing inclusions in the form of spheres, fibres, platelets, etc.). Efficient meshing algorithms are used to generate morphology adaptive quality meshes under periodic boundary conditions.

The accuracy and applicability of this method is studied here by applying it to short fibre reinforced polymer composites (Ch. 3). The study was performed in collaboration with Dr. Peter J. Hine, University of Leeds, UK and Dr. Hans Rudolf Lusti, ETH Zürich. A special image analysis technique developed at Leeds allows to determine the 3D fibre orientation state in real fibre reinforced polymer samples. [4] Our finite element method is then used to generate computer models that represent the measured fibre orientation distribution and to compare the predicted thermoelastic properties to experimental values. [5–7]

Having validated the accuracy of our direct numerical prediction against experimental data, in a subsequent step the accuracy of some widely used micromechanical models such as the Halpin-Tsai and the Tandon-Weng model are investigated. [8]

The orientation state of misaligned (i.e. not unidirectional fibres) is concisely described by orientation tensors. We study whether orietational averaging of the thermoelastic properties leads to accurate predictions by comparing the orientational averaged predictions to direct numerical predictions. [9]

The described finite element method has also been successfully applied to a number of other problems found in particulate composites. [1, 2, 10–18]

Considering more complex microstructures that do not consist of particulate inclusions but are for example of a interpenetrating network type of structure we found that the above-mentioned method of microstructure generation reaches its limits. The biased Monte Carlo procedure cannot be applied to realise such microstructures. Therefore it is essential to find another approach to generate computer models of the microstructure of such composite materials. A possible approach is to use modeling methods such as self consistent field theory (SCFT) [19]. Another approach, which is followed in Ch. 7 and Ch. 8 is to image the real

3-D microstructure of a composite material either by serial sectioning [20] or by 3D X-ray microtomography [21, 22]. This method allows to get microstructural information of a composite material with micrometer resolution. From this information it is possible to directly realize 3D microstructural models of the composite.

Two examples of composite materials with complex microstructure have been studied in the present thesis. They cover a wide range of materials classes from polymers to metals. The first example is a composite of low density polyethlyene (LDPE) with a phosphate glass (Pglass) with low glass transition temperature. In this thesis this material is called LDPE/Pglass hybrid. The two phases are in a 1:1 volume fraction. This material was studied in collaboration with Prof. Joshua Otaigbe and co-workers of the University of Southern Mississippi, USA. Results on this material can be found in Ch. 7.

The second example was studied in collaboration with Thomas Etter and Prof. Petter Uggowitzer of the Laboratory for Metal Physics and Technology of ETH Zürich. Porous graphite was infiltrated with a melt of an aluminium alloy. The metal volume fraction is 15 %. Details are discussed in Ch. 8.

X-ray microtomography data was used to build 3-D computer models of the composites. Effective materials properties such as electrical conductivity and Young's modulus are predicted by a finite element method.

2 The Finite Element Method

2.1 Types of Meshes

Meshes for Finite Element Models can be constructed in two principally different ways. So-called unstructured meshes do not have a regular structure but they are usually adapted to the microstructure investigated. Grids, which one could call "structured meshes" as opposed to unstructured meshes, constitute of a regular arrangement of cubic (or cuboid) elements irrespective of the specific microstructure studied.

2.1.1 Unstructured Meshes

In the past, because of restricted computer memory available, but also for limiting computational time regarding the limited processor speed of those days, it was an important issue in the field of finite elements to optimize the number of elements used for calculations. Much effort was therefore put in writing effective meshing algorithms that generate FE meshes that allow to make accurate predictions of effective properties based on a minimal number of elements thus saving computational resources. A method has been developed that uses morphology adaptive tetragonal meshes to predict the effective mechanical and physical properties of particulate composites, i.e. composites comprised of e.g. spheres, spheroids, short fibres, or platelets in a matrix material. [1, 2, 10]. The method has been verified and successfully applied to a large number of different systems [5–9, 12, 14, 15, 18]. It has also been made commercially available [23].

The use of unstructured morphology adaptive meshes has, however, a big drawback. The meshing algorithms used are sophisticated and optimized to achieve good results for a specific type of inclusion. In principle, it is possible to write such a meshing algorithm for every specific type of microstructure one would like to investigate. However, since this is a time consuming task, it may not be advisable to do so. It would be useful to have a generally applicable method.

2.1.2 Grids

More complex microstructures, as compared to particulate ones, are of great scientific and technological interest. Such microstructures are for example block

copolymers, interpenetrating networks (IPN), or foams. They possess interesting mechanical and / or physical properties. It is advantageous to predict their material properties numerically in order to guide the material development. However, the generation of unstructured meshes for such microstructures is either inefficient or even impossible with the existing meshing algorithms. One would therefore be forced to adapt or newly develop the meshing algorithm for each type of microstructure.

A straight-forward way to circumvent the aforementioned problem is to use grids, i.e. regular cubic meshes. It is obvious that in order to reproduce arbitrary microstructures accurately one should use a high grid resolution. This in turn results in a high number of elements for the calculations.

3-D models of complex microstructures can be acquired either through modeling (e.g. Self Consistent Field Theory SCFT [19]) or experimentally by 3-D imaging methods such as X-ray microtomography. These methods generically produce model data in a grid format. Hence, the microstructural information can directly be used to build a grid-based FE model.

Clearly with this approach we save resources on the model building side, but we need more computing resources for the property calculations because the number of elements in the model is much larger than with unstructured meshes.

The FE model was implemented on a cubic grid of serendipity family linear brick elements (Fig. 2.1) [3, 24].
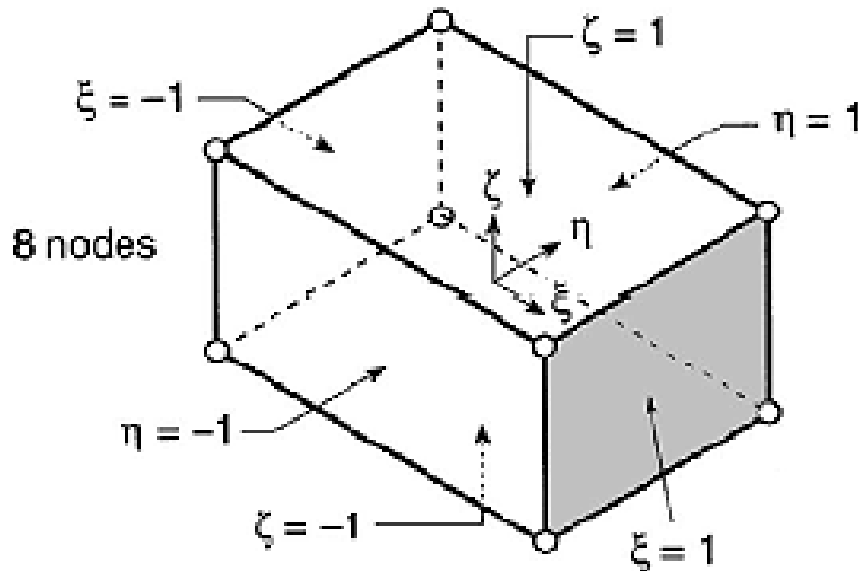
Figure 2.1: Eight-noded linear brick element of the serendipity family of elements. From Ref. [24]

2.2 Effective Materials Properties

After creating the FE model, be it with an unstructured mesh or be it on a grid, materials properties corresponding to the respective phase of the element are assigned to each element. Within one element the properties are uniform.

The overall effective properties of a composite material are determined by applying a certain perturbation to the model and then calculating the material's response to that perturbation numerically by a variational formulation FE method.

For calculating the effective electrical conductivity of a composite, for example, an external electrical field is applied. Then the Laplace equation

$$\mathrm{div}\sigma(\mathbf{r})\mathrm{grad}\phi = 0 \tag{2.1}$$

for the unknown nodal potentials is solved by minimizing the total electrical energy of the system in the presence of the field by a conjugate gradient method. [25] At the energy minimum the nodal potentials are uniquely defined and the local current within each element can be calculated. The effective conductivity of the composite is then extracted from the linear response relation between the overall current and the applied electric field. The complete electrical conductivity tensor can be retrieved by successively applying the field in the x-, y-, and z-direction, respectively [2].

With the same method other properties that are governed by the Laplace equation (eq. 2.1) can be calculated, e.g. the overall effective heat conductivity, the effective dielectric constant, or the effective gas permeability [2, 12].

The overall effective thermo-elastic properties (elastic constants and coefficient of thermal expansion) are calculated with a displacement-based linear elastostatic solver. Again a perturbation is applied, which, in this case, is a constant effective mechanical backstrain ϵ_{kl}. The solver finds a set of nodal displacement that minimizes the system's total strain energy in the presence of the backstrain. For the minimization a conjugate gradient method is used again. [25]

With the nodal displacements of the minimal strain energy conformation also the local strains in each element are known. From this the local stresses can be calculated by using the local elastic constants of the elements.

The overall effective elastic constants $\mathbf{C}_{ijkl}$ of the composite are calculated from the linear response relation

$$\sigma_{ij} = \mathbf{C}_{ijkl}\epsilon_{kl} \tag{2.2}$$

In order to determine the 21 independent components of the effective stiffness tensor $\mathbf{C}_{ijkl}$ six different strain states are applied and the elastic energy minimized for them (tensile strains in the three main axes directions and shear strains in the three main plains).

For calculating the overall effective thermal expansion coefficient a perturbation corresponding to a temperature change of 1 K is applied. At the same time an effective volume change is constrained such that the effective mechanical strain is zero ($\epsilon_{kl} = 0$). The strain energy is minimized as before and from the minimum strain energy state the effective thermal stress σ_{ij}^T is calculated.

By using the effective stiffness tensor $\mathbf{C}_{ijkl}$ calculated above or its inverse the effective compliance tensor $\mathbf{S}_{ijkl} = \mathbf{C}_{ijkl}^{-1}$ and the relation

$$\alpha_{ij} = \mathbf{C}_{ijkl}^{-1}\sigma_{kl}^T = \mathbf{S}_{ijkl}\sigma_{kl}^T \tag{2.3}$$

the six independent components of the overall effective thermal expansion coefficient α_{ij} can be determined. [26]

3 Short Fibre Composites

3.1 Introduction

Fibre reinforcement is a well-known method of improving the mechanical properties of polymeric materials. The traditional continuous fibre reinforcement requires elaborate, labour-intensive, and time-consuming winding or laminating techniques. Hence, the manufacturing process is expensive and only applicable for small part numbers. The use of short fibre reinforced polymers, however, allows to manufacture large numbers of parts with complex geometries. Existing processing equipment for thermoplastic materials can be used to injection mould, compression mould, or extrude such composites. Injection moulding is a fast and highly automatized way of producing parts with complex geometries. Fig. 3.1 shows the example of a clutch pedal produced by injection moulding of a short glass fibre reinforced nylon6.

It is therefore suitable for producing large numbers of parts in a cost-efficient way. As reinforcing fibres mainly glass fibres are used but the use of carbon fibres is also increasing. Typical injection moulded short glass fibres are $10\,\mu$m in diameter and $100 - 400\,\mu$m in length. Thus the fibre aspect ratio (ratio of length to diameter) is $10 - 40$. Usual fibre contents are $5 - 15$ vol.%.

The properties of short fibre reinforced composites can vary widely from isotropic (for a 3D random arrangement of fibres) to highly anisotropic (for fully aligned fibres). It is therefore essential to account for the fibre orientation in the design process of short fibre reinforced parts.

Commercial mould filling simulation softwares (e.g. Moldflow or Sigma-
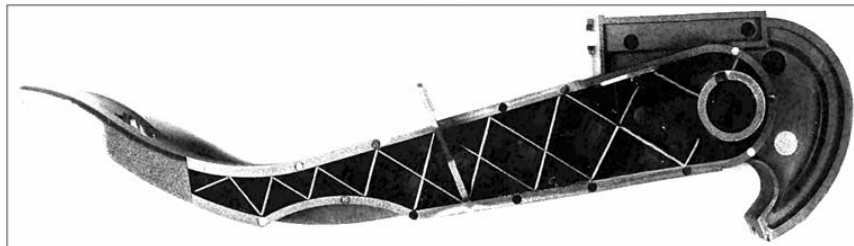
Figure 3.1: Injection moulded clutch pedal made of short fibre reinforced nylon6. [27]

soft/Magmasoft) are used to design the moulds and determine the processing parameters for injection moulding. They can simultaneously predict the local fibre orientation state in the finished part after cooling (Fig. 3.2). [27–30] The resulting predictions are in remarkable agreement with experimentally measured fibre orientation states. [27]

Based on the fibre orientation it is possible to calculate the local thermoelastic properties. This can then be used as input for the structural finite element analysis (using software such as Ansys or Abaqus) to determine the mechanical properties (stiffness, deformation, etc.) of the complete injection moulded part.

All presently available mould filling simulation softwares use a two-step approach for predicting the local thermoelastic properties. First, the properties of a uniaxially aligned composite are calculated based on one of the micromechanical models (e.g. Halpin-Tsai or Tandon-Weng). Second, the properties of the composite with fully aligned fibres are used to predict the properties of the composite with an arbitrary fibre orientation state by orientation averaging. [31]

The finite element method of Gusev [1, 2] allows to make direct numerical predictions of the thermoelastic properties of composites with a defined arbitrary fibre orientation state. It is therefore ideally suited to check the accuracy of the two-step procedure described above.

Overall this means that by designing the mould form and filling parameters one controls the local fibre orientation states. And this again is responsible for the macroscopic properties of the finished part. Because injection moulds are

Figure 3.2: Example output of mould filling simulation with predicted local fibre orientations. [30]

very expensive it is cost saving to apply a rational computer assisted design process rather than a experience-based trial and error approach.

In this chapter the application of the finite element method of Ch. 2 to short fibre reinforced composites is studied. First, arrangements of fully aligned fibres are used to investigate the influence of the fibre length distribution. Then, the effect of fibre misalignment is taken into consideration. Numerical predictions are compared with experimental results and with results calculated by some widely applied micromechanical models. Finally, a two step procedure is proposed that gives accurate predictions for arbitrarily oriented short fibres. The first step is to numerically predict the properties of composites with fully aligned fibres by using the finite element method. These results are then used in a second step to calculate the orientation average for composites with an arbitrary fibre orientation.
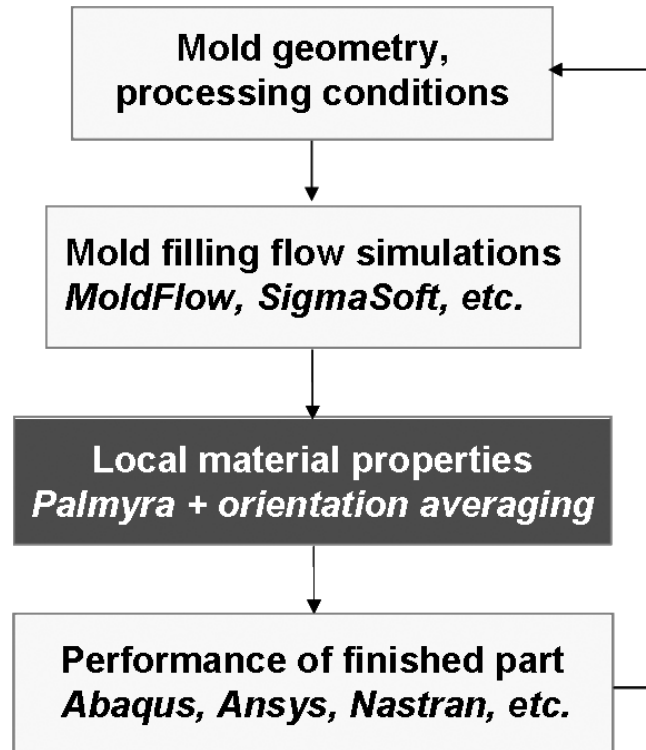
Figure 3.3: Computer assisted design process for short fibre reinforced polymer parts.

3.2 Validation

It has been shown that the spatial distribution of fibres in a unidirectionally aligned fibre composite has a significant influence on the elastic properties. Especially, the transverse packing of fibres needs to be considered in order to make accurate predictions of the transverse elastic constants. The numerical method of Ch. 2 was found to make the best predictions compared with experimental data. [11]

Here, the application of the FEM of Ch. 2 to short fibre reinforced composites is studied. Considering short fibre composites some additional parameters need to be considered, e.g. fibre length distribution (FLD) and fibre orientation (distribution).

3.2.1 Fibre Length distribution

Tucker and Liang reviewed the predictive capability of some commonly used micromechanical models. [32] The aim was to predict the properties of the composite unit, that is a representative volume element that can subsequently be averaged to reflect fibre length and orientation distributions of a real material. The fibre length aspect is usually addressed by replacing the FLD with some sort of mean length. A number of proposals for this "mean length" have been published for special fibre orientation states. Takao and Taya [33] and Halpin et al. [34] concluded that the number average length

$$L_N = \frac{\sum N_i \cdot L_i}{\sum N_i} \tag{3.1}$$

of a distribution was an appropriate value. Eduljee and McCullough [35] suggested a different value, namely

$$L_S = \frac{\sum N_i}{\sum \frac{N_i}{L_i}} \tag{3.2}$$

to take into account the skewed nature of real FLDs, in particular to give a heavier weighting to shorter fibres. The RMS (Root Mean Square) number average

$$L_{RMS} = \sqrt{\frac{\sum N_i \cdot L_i^2}{\sum N_i}} \tag{3.3}$$

has also been suggested as a possible descriptor of the FLD. The weight average

$$L_W = \frac{\sum W_i \cdot L_i}{\sum W_i} \tag{3.4}$$

was also included in the study for reasons of completeness. It would seem, therefore, that there is merit in being able to model an assembly of fibres with a 'real' FLD, in order to establish whether the distribution can be replaced by one of the above mean values in order to establish what McCullough [35] describes as 'the appropriate statistical parameters to represent the microstructural features of the composite'.

The aim of the current work, was therefore, to assess the numerical procedure of Ch. 2 in order to establish whether it has any merit over the current physical and phenomenological models. The advantages of the new approach are expected to be due to determining the properties of an assembly of fibres, giving the opportunity to incorporate fibre length and orientation distributions, the chance to have isotropic or anisotropic phases (most other models can only deal with isotropic phases); the possibility of combining different reinforcement shapes (cylinders, particles, plates etc) and even the possibility of studying layered structures.

The approach taken here was to start with simple microstructures and increase the complexity up to that seen in a real material. Unfortunately the simplest systems (i.e. aligned monodispersed length fibres) are the most difficult to manufacture. Simulations were carried out to look at the effect of fibre length distribution. Image analysis measurements of a typical FLD from an injection moulded plate were used to seed the Monte Carlo procedure, producing simulations with an equivalent FLD. Results from these runs were compared to runs carried out using assemblies of monodispersed length composites to assess whether the length distribution could be replaced by a single length. For the simulations presented in this paper, both phases were chosen to be isotropic, with short glass fibres in a typical isotropic thermoplastic.

Numerical

Direct finite-element calculations of three-dimensional multi-inclusion models were done under periodic boundary conditions in an orthorhombic periodic box. All computer models comprised fibres perfectly aligned along the x-axis of the periodic box and placed on random positions using a Monte-Carlo(MC) algorithm [1]: a typical example is shown in Fig. 3.4. For monodispersed fibres the aspect ratio of the box, a/b, was set to 7.5 where a is the box dimension in the x-direction of the coordinate system and b in the two lateral directions y and z (Fig. 3.4). The computer models comprising fibres with a distribution of lengths had to be generated in a more elongated periodic box of aspect ratio 25 due to the fact that fibres must not be longer than the box because this would imply self-overlaps under periodic boundary conditions. Previously, it was checked with monodispersed fibres that numerical predictions are not influenced by changing the box aspect ratio from 7.5 to 25.

In order to generate computer models that behave homogeneously and deliver accurate overall composite properties the minimum representative volume element (RVE) was investigated. [1, 36] Computer models with 5 different sizes of the periodic box all comprising a random dispersion of 1, 8, 27, 64 and 125 aligned fibres with aspect ratio 30 and volume fraction 0.15 were created. For each box size three MC-runs were performed and delivered three different fibre arrangements. The elastic properties of each set of three computer models with a particular size were calculated numerically and from the results the arithmetic mean and the 95% confidence interval were determined. Fig. 3.5 shows that for the Young's modulus E_{11} with 30 fibres one can already get predictions deviating only a few percent from the true value provided that one averages the results of three individual calculations (the 1 direction here is the direction of fibre alignment, the x-axis of Fig. 3.4: the 2 axis is perpendicular to this and corresponds to the y and z axes in Fig. 3.4). In the case of larger computer models comprising 125 fibres the individual predictions for the different MC-configurations show hardly any scatter. Consequently, it was decided to generate computer models comprising 100 fibres and to obtain the effective elastic properties for composites with a monodispersed fibre length from one single MC-configuration.

However, in the case of polydispersed fibres the distribution of fibre length was sampled in three MC-runs in order to approximate the measured distribution reasonably well. First, the measured distribution of fibre length was transformed into the cumulative probability density function. This function allowed to sample the distribution of lengths by generating 100 random numbers in the interval [0,1] and to determine the corresponding fibre lengths before the 100 fibres were put into the periodic box on random positions without overlaps (see Fig. 3.4).
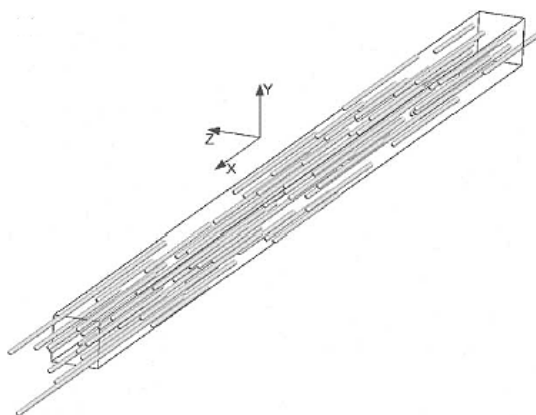
Figure 3.4: Orthorhombbic periodic box containing 100 perfectly aligned fibres with different fibre lengths received by sampling a measured distribution in a Monte Carlo run.
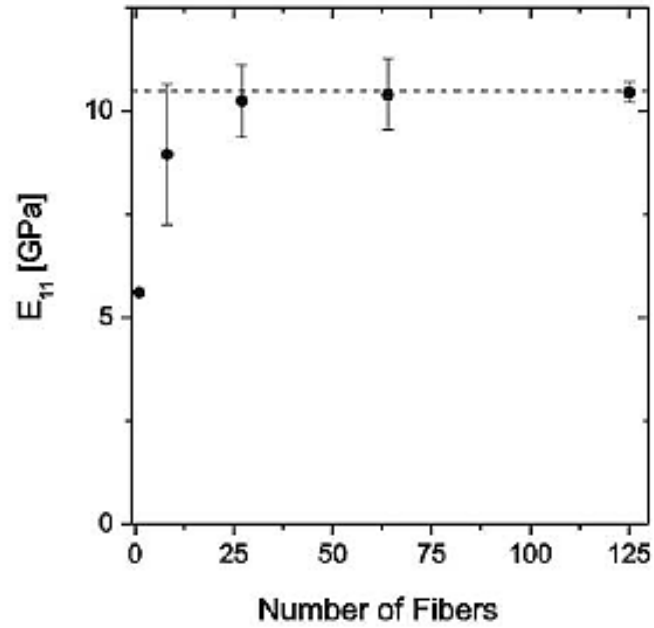
Figure 3.5: Predictions for the longitudinal Young's modulus E_{11} depending on the size of the computer models (number of fibres). The black circles indicate the arithmetic mean of three individual estimates and the error bars show the 95% confidence interval.

In each of the three MC-runs this procedure was repeated using a different seed for the random number generator and consequently MC-configurations with different FLDs resulted. Averaging the distributions of three individual MC-runs approximated the experimentally measured FLD reasonably well (see Fig. 3.6).

Results and Discussion

The distribution of fibre lengths that are normally present in a real material is an aspect of short fibre composites which can be difficult to address analytically. The most popular approach is to replace the FLD with a single length, normally the number average length. The numerical simulation offers the chance to establish if this approach is valid.

As a first step, additional simulations were run using monodispersed distributions up to an aspect ratio of 50. The results are shown in Fig. 3.7, with the diamonds representing individual runs at that aspect ratio, and the solid line the best fit through all the data. The random nature of the generated microstructures is reflected by the scatter of the points around the best fit line.

The next stage was to carry out numerical runs using a distribution of fibre lengths. In order to be representative, a real data set, measured using the image facilities developed at the University of Leeds, was used as the basis of the simulations. [37] The measured data for 27'500 fibres, collected by Bubb from an injection moulded short glass fibre filled plate, [38] is shown in Fig. 3.8. For
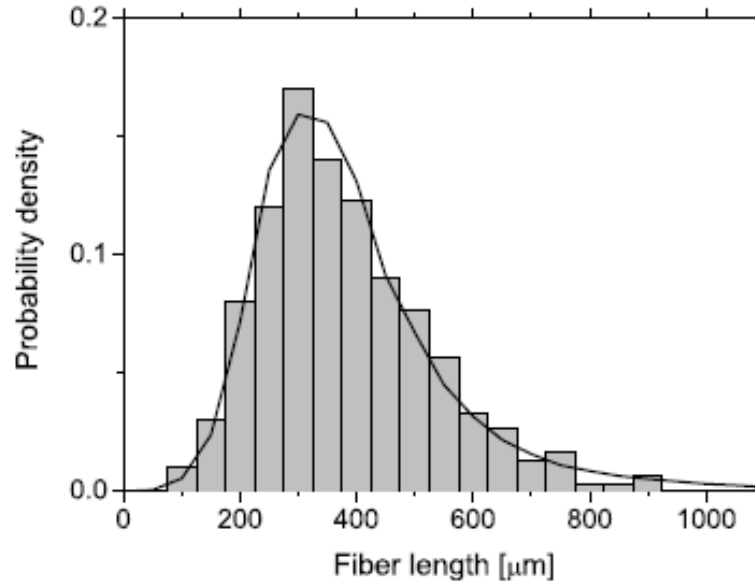
Figure 3.6: Probability density distribution of fibre lengths after 3 MC-runs shown as a bar plot. The black line indicates the measured length distribution.

this non-symmetrical distribution the number average length was determined as $388\,\mu$m and the weight average length as $454\,\mu$m. Using a fibre diameter of $10\,\mu$m gives aspect ratios of 38.8 and 45.4 for the length and weight averages respectively. As described earlier, the measured FLD was used to seed the Monte Carlo runs, and as shown in Fig. 3.6, the agreement between the generated length distribution and the measured one was excellent. The generated microstructures, with the polydispersed length distribution, were then used to determine the longitudinal modulus, E_{11}.

The question to be answered is what is the length of a monodispersed distribution, which would have the same longitudinal modulus as the 'real' distribution? Fig. 3.9 shows a comparison of the values from the monodispersed and polydispersed distributions. The horizontal lines show the band of predictions from three polydispersed MC runs, in this case 10.9 ± 0.1 GPa. The diamonds in Fig. 3.9 show the predictions from the monodispersed distributions at each particular aspect ratio. Where the best line fit through the diamonds crosses the horizontal lines, gives the aspect ratio which would fit the real distribution, which for this set of data was 36.6 ± 2.5. The first column of Table 3.1 shows a comparison of this aspect ratio with various measures of the distribution, namely the number and weight average aspect ratios, the RMS number average aspect ratio, and the skewed number average aspect ratio proposed by Eduljee and McCullough. [35] It is seen that the number average gives the closest agreement, although the value lies between the number average and skewed number average.
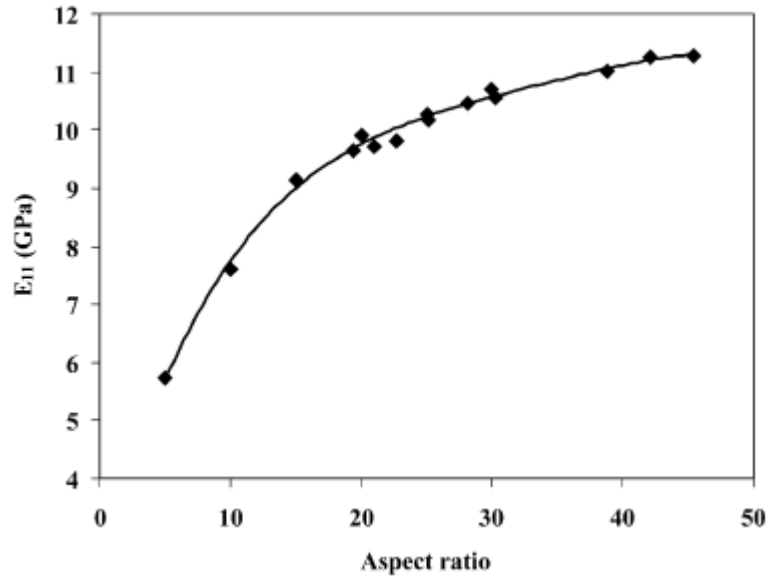
Figure 3.7: E_{11} vs. aspcect ratio for a volume fraction of 15%: simulations used a single aspect ratio. The solid line is a best fit through all data.
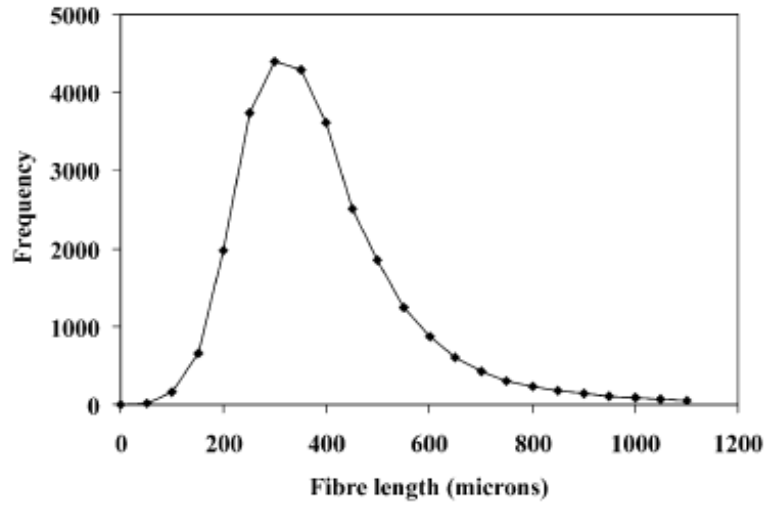
Figure 3.8: Experimentally measured fibre length distribution (FLD) from Bubb [38].
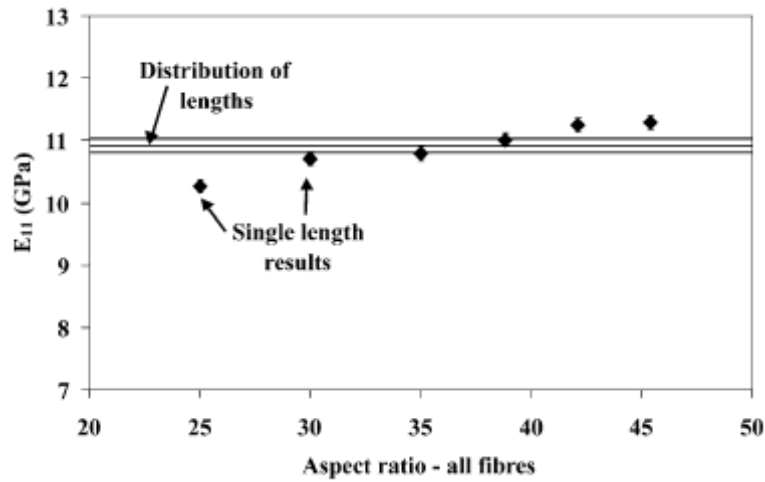
Figure 3.9: A comparision of predictions of E_{11} for a distribution of fibre lenghts and single length predictions – fibre diameter $= 10\mu$m.

To explore different regions of the modulus vs. aspect ratio curve shown in Fig. 3.7, other aspect ratio distributions were generated by using the length data in Fig. 3.8 but with different fibre diameters of 15, 20 and 25 μm. Fig. 3.10 shows the aspect ratio distributions for fibre diameters of 10 μm (as used so far) 15 and 20 μm: as the fibre diameter is increased the distribution is pushed to lower aspect ratios. As above, the single length needed to match the modulus of the 'real' distribution was determined for each distribution. The results, in comparison with the same measures as before with a fibre diameter of 10 μm, are shown in Table 3.1 and Fig. 3.11. While one single measure of the shape of the distribution does not fit exactly with the value derived from the numerical procedure, the number average aspect ratio appears to be the best choice to cover the whole range of likely aspect ratios. This result explains why this measure of the shape of the length distribution has proved so successful, although until this point there has been little justification for its use.

3.2.2 Effects of Fibre Misalignment

After having studied composites with fully aligned fibres and the effect of fibre length distribution, the second topic to be addressed is fibre misalignment. In a real short fibre composite the fibres are never perfectly aligned. It is therefore important to test whether the numerical approach can well handle the effect of misaligned fibres.
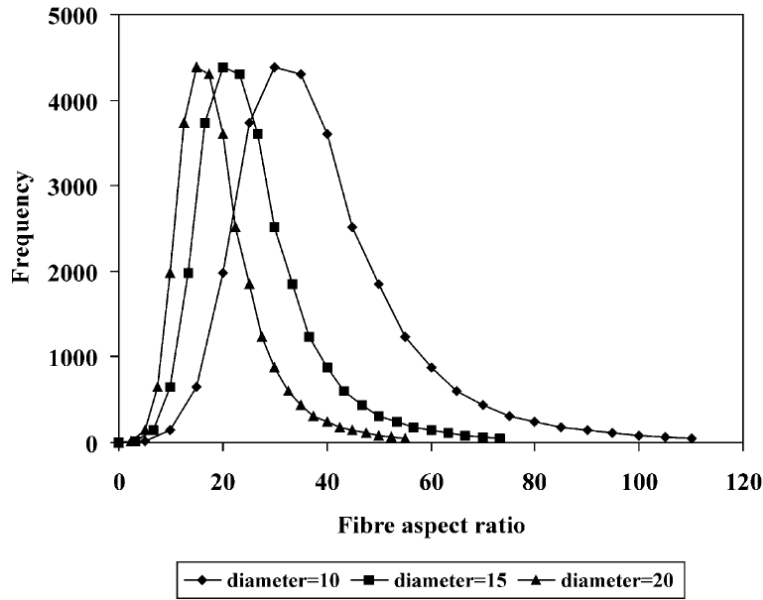
Figure 3.10: Fibre aspect ratio distributions for a diameter of 10, 15 and 20 μm.

Table 3.1: A comparison of the single aspect ratio which matches the modulus of the real distribution with various parameters to describe the real distribution, for different fibre diameters.

Fibre diameter [μm]	10	15	20	25
Single aspect ratio to match the distribution modulus	36.6 ± 2.5	24.3 ± 1.4	20.7 ± 0.5	15.8 ± 0.5
Number average aspect ratio	38.8	25.9	19.4	15.6
Weight average aspect ratio	45.4	30.2	22.7	18.1
RMS number average aspect ratio	41.9	28.0	21.0	16.8
Skewed number average aspect ratio after McCullough [35]	33.2	22.1	16.6	13.3
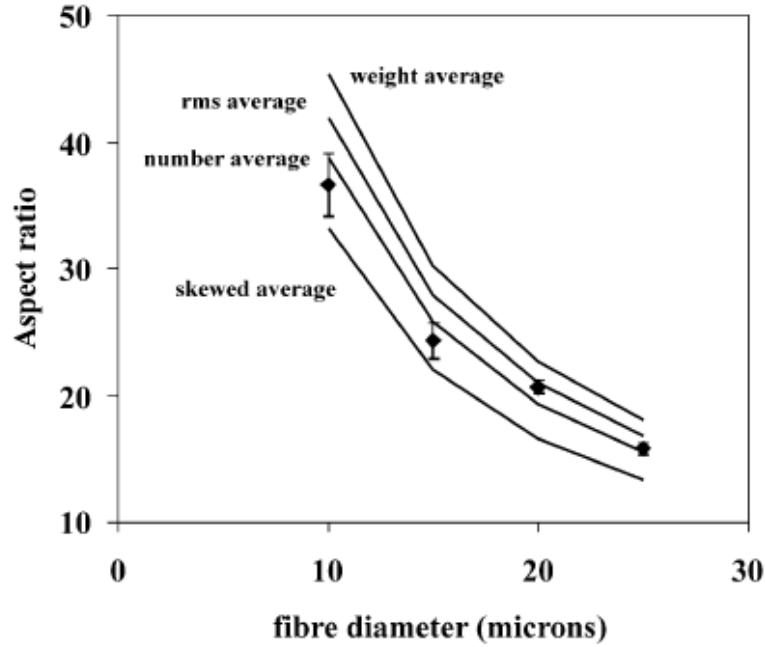
Figure 3.11: A comparison of the monodispersed aspect ratio which best fits the polydispersed distribution (diamonds) and the various distribution averages.

Table 3.2: Elastic and thermoelastic properties of polypropylene and glass fibres that were used to calculate the overall properties of short glass fibre reinforced composites both numerically and by the use of micromechanical models.

	Polypropylene	Glass fibres
E [GPa]	1.57	72.5
ν	0.335	0.2
α [10^{-6}K^{-1}]	108.3	4.9

Experimental

Dumbbells of 80 mm length with a gauge length of 25 mm and gauge diameter of 5 mm were injection moulded by conventional and shear controlled orientation injection moulding (SCORIM) using a mould gated at both ends. [39] The first set of samples was produced by conventional injection moulding where the polymer/glassfibre melt was injected into the mould through one gate of the mould before the sample was cooled down. For the second set of samples the shear controlled orientation moulding process (SCORIM) developed at the University of Brunel was used. Again the polymer/glassfibre melt was injected through one gate but during cooling of the sample, the polymer melt containing the glass fibres was forced back and forth through the mould cavity using both gates of the mould. Due to the additional shear forces experienced by the melt during the SCORIM process, the fibres are more highly aligned along the dumbbell axis than in conventional injection moulding.

The material used was a glass-fibre-polypropylene granulate from Hoechst, Grade G2U02, containing 20 wt.% of short fibres. The polypropylene was an easy flowing injection moulding grade with a melt flow index (MFI) of 55. Specifications of the elastic and thermoelastic properties of the polypropylene matrix and the glass fibres are listed in Table 3.2. The degree of fibre orientation in each of the types of injection moulded sample was measured on a two-dimensional longitudinal cut through the axis of the central gauge length section, using an image analysis system developed at the University of Leeds. [40] The orientation in both samples was found to be non-uniform with a well aligned shell region around a central, less well aligned, core. This pattern of fibre orientation was found to be symmetric about the centre line of the section and consistent along the gauge length.

Typical image frames ($\sim 400 \times 700\,\mu$m) taken from the shell region of each sample type are shown in Fig. 3.12: the injection, or 1 axis, is horizontal. It is clear that in the SCORIM sample (Fig. 3.12 B) the fibres are more highly aligned along the 1 axis compared to the conventionally moulded sample, which

itself has a high preferential alignment. To compare with mechanical measurements, the fibre orientation distributions for each gauge length cross section was required. To produce this distribution, the 2D image analysis data was divided into 10 strips across the sample diameter and then normalised in terms of the appropriate angular area. As the distributions were found to be transversely isotropic, for averaging purposes they can be described by only two orientation averages, $\langle cos^2\theta \rangle$ and $\langle cos^4\theta \rangle$. The measured values of these two averages were 0.872 and 0.769 for the conventional moulding and 0.967 and 0.936 for the SCORIM moulding, for the second and fourth orders, respectively.

In order to measure the fibre length distribution of the two samples the polypropylene matrix was first burnt off at a temperature of 450℃ in a furnace. The remaining glass fibres were spread onto a glass dish and their length distribution was determined by image analysis. The burn off technique was also used to confirm that the weight fraction of the fibres was 20%, giving a volume fraction of 8% from a knowledge of the constituent phase densities.

The Young's modulus E_{11}, of the glass fibre reinforced samples was measured in a tensile test at a constant strain rate of 10^{-3}s^{-1}. The sample strain was measured using a Messphysik video extensometer and 10 samples were measured for each sample type. To determine the properties of the matrix phase, compression moulded plates were made from pellets of the unreinforced polymer. The matrix Young's modulus was measured using the same technique as above, while the Poisson's ratio was determined using an ultrasonic immersion method.

Thermal expansion was measured for both composite samples and unreinforced polypropylene using a dilatometer by measuring the length change of the samples for a temperature change from +10 to +30℃ both in the longitudinal and the transverse direction of the dumbbells.
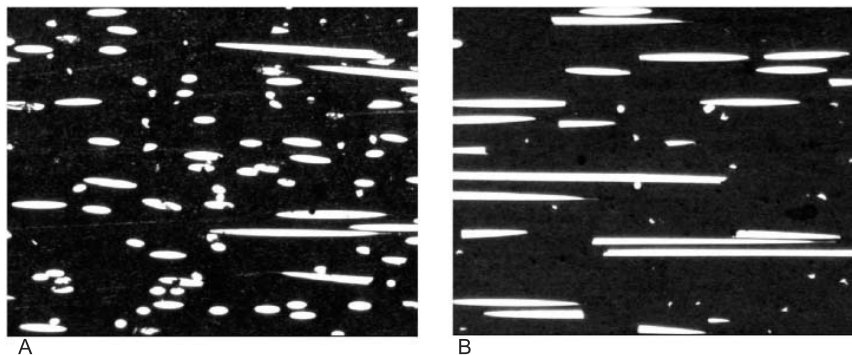
Figure 3.12: Typical image frames ($700 \times 530\,\mu$m) from the shell region of the samples' gauge section. A and B show longitudinal cuts through the gauge section of a conventionally (A) and a SCORIM (B) injection moulded dumbbell, respectively.

Numerical

The computer models comprised 150 misaligned fibres of equal aspect ratio randomly positioned in a cubic box at a volume fraction of 8%. For both the conventional and the SCORIM moulded sample the length distribution of the fibres was measured and the number average was assigned to all fibres in the respective computer model. In the previous section (Sec. 3.2.1) it was shown that the number average is the best choice to substitute a length distribution by a single fibre length. For the conventionally moulded sample the average length was $448\,\mu$m whereas for the SCORIM sample it was slightly smaller with $427\,\mu$m. The diameter of the glass fibres was measured as well and found to be $12\,\mu$m in both samples. The specification of the number of fibres, their length and diameter determines the total fibre volume in the computer model and as it is known that the fibre volume fraction is 8% the length of the periodic cubic box is fixed. The orientation of each fibre was determined individually by sampling the fibre orientation distribution (see Fig. 3.13) with a Monte-Carlo algorithm giving one of two angles necessary to define the orientation of a fibre. For this purpose, the measured frequency distribution of the angle θ was transformed into the cumulative probability density function so that to any number in the interval [0,1] a unique angle θ is asigned. During a Monte-Carlo run the cumulative probability density function was sampled with 150 random numbers in the interval [0,1] and each fibre was assigned a value for the angle θ. Assuming that the angle ϕ is homogeneously distributed in the intervall $[0°, 360°]$ which means that the gauge section of the dumbbell is transversely isotropic another 150 random numbers were necessary to randomly determine the second angle ϕ.

After having specified length, diameter and orientation of all 150 fibres they were successively positioned in the periodic box. Again by using random numbers the fibres were inserted at random positions into the periodic box and a subroutine checked for overlaps with already positioned fibres. If overlaps occured the position was rejected and the algorithm repeated the procedure until the fibre could be placed without overlaps and until all fibres were placed in the periodic box. Because the fibres were misoriented it was impossible to randomly place the fibres without overlaps even at the relatively small volume fraction of 8%. This problem was overcome by increasing the box size and inserting the fibres at a dilute volume fraction of 0.1 vol.%. The box was then compressed step-by-step during a variable-shape Monte-Carlo run to the desired volume fraction of 8% keeping the fibre orientations constant while repeatedly displacing each fibre in the box. In Fig. 3.14 examples of the computer models are shown together with cuts through the finite element meshes. In order to obtain information about the scatter of the numerical predictions three computer models were generated for both the conventional and the SCORIM composite by

sampling the measured θ-distribution with different seeds for the random number generator. By averaging the individual orientation distributions of the three computer models the measured distribution was approximated more accurately (see Fig. 3.13).

The 6 computer models (3 for the conventional and 3 for the SCORIM distribution) were meshed into unstructured, morphology-adaptive finite-element meshes with the consistent use of periodic boundary conditions. [1, 2, 41] The effective elastic properties are numerically calculated from the response to an applied perturbation in the form of a constant strain. The task to solve is to find a set of nodal degrees of freedom that minimize the strain energy. An iterative conjugate-gradient solver with a diagonal preconditioner was used for the finite element analysis. [1,25,41] The end criterion was the first residual norm to be reduced by a factor of 10^4 relative to its initial value. At the energy minimum the local strains are known and allow to assemble the effective stress. The effective elastic constants can then be calculated from the linear-elastic response equation. Six independent minimization runs with 6 different effective strains are necessary to determine all 21 independent components of the stiffness matrix.

To obtain the effective thermal expansion coefficient local non-mechanical strains corresponding to a temperature change of one degree are applied and the strain energy is minimized as already described in the previous paragraph. Calculating the effective thermal stress at the energy minimum and using the
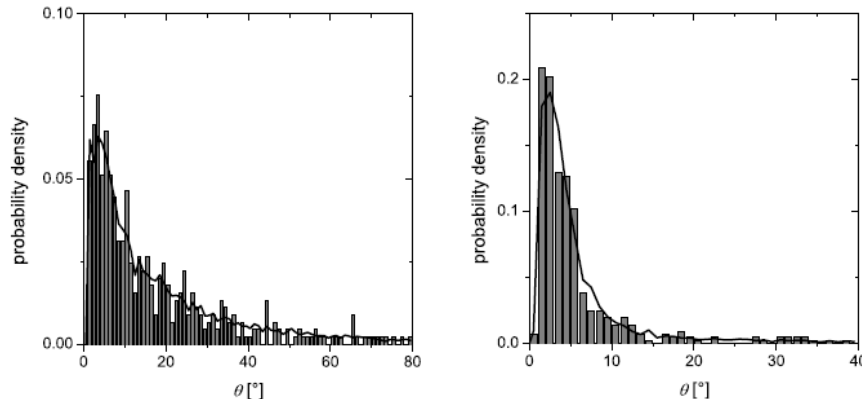
Figure 3.13: The average θ-distribution of the fibres in three computer models that were generated by sampling the measured θ-distribution (black line) during a Monte-Carlo run shown for the conventionally moulded composite (left) and for the SCORIM moulded composite (right). The angle θ characterizes the fibres' misalignments and the depicted measured distributions were obtained by averaging numerous measurements that were done across longitudinal sections of the dumbbells' gauge length.
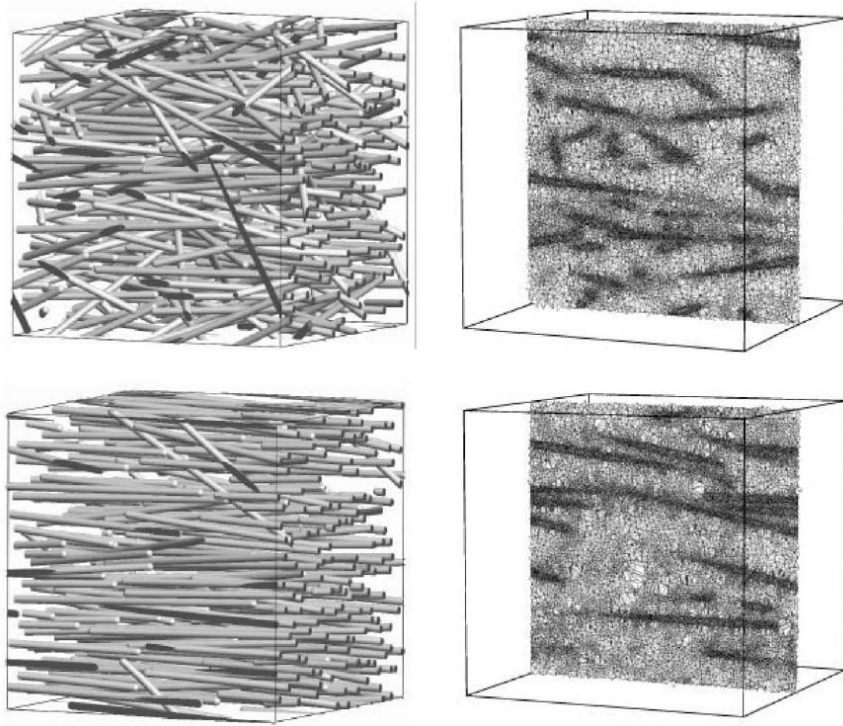
Figure 3.14: On the left side snapshots of the 3D multi-fibre computer models are shown for both the conventionally (top) and the SCORIM (bottom) composite. On the right side longitudinal cuts through the finite element mesh of both computer models are shown.

effective elastic constants one can determine the 6 independent components of the effective thermal expansion tensor. [2, 41]

The finite element meshes of all 6 computer models consisted of about 2.4×10^6 nodes and 15×10^6 tetrahedra. Calculations were done on a HP Visualize J6700 Workstation with two PA-RISC 8700 processors and took between 20 and 30 h for 7 minimizations (6 minimizations to determine the elastic properties and 1 minimization to determine the thermo expansion coefficients) on a single processor.

Results and Discussion

In this section both experimental and numerical results for glass fibre reinforced polypropylene are presented and discussed by including different micromechanical models for comparison. Both experimental and numerical results of the Young's modulus E_{11} in the longitudinal direction of the glass-fibre/polypropylene dumbbell are listed in Table 3.3. The numerically calculated Young's modulus E_{11} is nominally higher than the measured value for both the conventional and the SCORIM sample but the difference is less than 1% and is well inside the error range of the measurements. Both the experimental and the numerical values lie much closer to the upper bound predictions of the micromechanical models, confirming the well held belief that a state of constant strain is the most appropriate for well aligned glass fibre reinforced polymers. The Tandon and Weng model combined with the Ward approach for determining the aggregate properties gives an upper and a lower bound. The upper bound is closest to the measured values slightly underestimating them by 1.5% for both the conventionally and the SCORIM moulded samples, while the lower bound is significantly lower. The upper bound of the McCullough model which takes a combined approach for both the elastic and the thermoelastic properties gives quite accurate predictions, too. For the SCORIM sample, which has the highest degree of fibre alignement, the upper bound of the McCullough approach differs by 1.7% from the measured value for the Young's modulus E_{11} whereas for the conventional sample it is somewhat lower with a difference of 4.4%. It appears that this model looses accuracy the less well aligned the fibres are, although the differences are small. The predictions of the combined Cox-Wilczynski/aggregate approach shows larger deviations of around 8% from the experimental values. Therefore this approach is less appropriate to accurately predict the Young's modulus E_{11} of composites with misaligned short glass fibres.

Table 3.4 lists the results for the longitudinal thermal expansion coefficients α_1 of the two glass-fibre/polypropylene composites. While the difference between the measured values is somewhat larger than between the numerically calculated ones, both measurements and simulations show the same trend, that is the con-

24

Table 3.3: The Young's modulus E_{11} in the longitudinal direction of both conventionally and SCORIM injection moulded glassfibre/polypropylene dumbbell samples.

	Young's modulus E_{11} [GPa]	
	conventional	SCORIM
Measured	5.09 ± 0.25	5.99 ± 0.31
Numerical	5.14 ± 0.10	6.04 ± 0.02
Tandon-Weng/Aggregate		
Upper bound	5.01	5.90
Lower bound	3.78	5.48
McCullough		
Upper bound	4.87	5.89
Cox-Wilczynski/Aggregate		
Upper bound	4.70	5.44

ventional moulded sample has a larger thermal expansion coefficient α_1 than the SCORIM sample. Comparing our results for the longitudinal thermal expansion coefficient α_1 with micromechanical models first the Tandon and Weng/Takao and Taya approach is considered. This model calculates the thermal expansion coefficients of the perfectly aligned unit, so some form of orientation averaging is required to calculate the properties of the aggregate. From the literature it appears that there are two choices for determining the aggregate properties; either carry out a simple second order average of the longitudinal and transverse thermal expansion coefficients (i.e. $\alpha_1^{composite} = \alpha_1 \langle \cos^2 \theta \rangle + \alpha_2 \langle \sin^2 \theta \rangle$), which ignores any elastic constraints, or try to include the elastic constraints by using a modified laminate model (e.g. [34, 42]). The laminate approaches assume that the composite material behaves as a biased laminate fabricated from layers with the appropriate unit properties. The effects of misorientation are then handled by placing the biased plies at the average orientation angle. The results in Table 3.4 show, as might be expected, that ignoring the elastic constraints (second order average only) leads to an overprediction of the thermal expansion while the laminate approach tends to underpredict the thermal expansion by overemphasising the elastic constraints. When the fibres are highly aligned, i.e. in the SCORIM sample, the two approaches converge and the Tandon-Weng/Takao-Taya/laminate model gives quite an accurate prediction. The McCullough model, which predicts values for the aggregate directly, delivers values close to both measured and numerical values but like the Tandon-Weng/ Takao-Taya/laminate model it predicts a lower value of α_1 for the conventional than for the SCORIM sample which was not confirmed by either measurements or by numerical simulations. The laminate theory also predicts a decrease of

Table 3.4: Longitudinal and transverse thermal expansion coefficients of both conventionally and SCORIM injection moulded glassfibre/polypropylene dumbbell samples.

	Longitudinal thermal expansion α_1 $[10^{-6}\mathrm{K}^{-1}]$	
	conventional	SCORIM
Measured	32.9 ± 1.5	27.7 ± 1.7
Numerical	30.6 ± 1.0	29.3 ± 0.1
Tandon-Weng/Takao-Taya/aggergate	42.3	32.0
Tandon-Weng/Takao-Taya/laminate	26.3	29.4
McCullough	29.2	31.4
	Transverse thermal expansion α_2 $[10^{-6}\mathrm{K}^{-1}]$	
	conventional	SCORIM
Measured	121 ± 2	121 ± 1
Numerical	115 ± 1	119 ± 0.1
Tandon-Weng/Takao-Taya/aggergate	115	120
Tandon-Weng/Takao-Taya/laminate	109	119
McCullough	118	121

the thermoexpansion coefficient α_1 as the degree of fibre misalignment increases. This effect is explained by the rapid increase of the in-plane shear modulus (G_{12}) with increasing degree of fibre misalignment [42]. Depending on the level of fibre anisotropy and volume fraction, a minimum for the thermal expansion coefficient α_1 might occur at a particular value of average fibre misalignment. Both the measured and the numerically calculated thermal expansion coefficient α_1 show the opposite behaviour, that is the conventionally moulded thermal expansion is higher than the SCORIM sample, which is perhaps an indication that the laminate and McCullough models overpredict the effects of elastic constraint.

For both sample types the same transverse thermal expansion coefficient $\alpha_2 = 121 \cdot 10^6\mathrm{K}^{-1}$ was measured. Numerical calculations delivered a lower transverse thermal expansion coefficient α_2 for the conventional compared to the SCORIM sample, which is in harmony with all the micromechanical models. All micromechanical models in particular the Takao-Taya/aggregate model, agree well with both the measured and the numerical values.

To summarise the results for both elastic and thermoelastic properties, it was found that agreement between measurements and numerical simulations is excellent, when the numerical simulations are based on the correct microstructure, thus validating the numerical approach and demonstrating that it accurately

predicts all elastic constants not only for idealized morphologies of aligned fibres but also for morphologies containing imperfections like fibre misalignments. Comparison with micromechanical models showed that the Tandon-Weng model together with the upper bound from the aggregate approach is very accurate in predicting the Young's modulus E_{11}, confirming the current published literature. For the transverse thermoexpansion coefficient α_2, the measured as well as the numerically calculated values agreed well with several micromechanical models, whereas for the longitudinal thermoexpansion coefficient α_1 none of the micromechanical models showed the correct relationship between the two orientation states, as was correctly predicted by the numercial simulation.

3.3 Stiffness and Thermal Expansion of Short Fibre Composites with Fully Aligned Fibres

Predicting the overall, effective properties of short fibre composites with fully aligned fibres from the properties of the individual phases and the composite's morphology has attracted a great deal of attention during the last decades, and a variety of micromechanics-based and empirical models have been proposed. [32, 43–50] It has however been difficult to objectively assess the predictive capability of the models, as it is rather hard in practice to fabricate well-controlled samples of composites with fully aligned short fibres. Accordingly, it has also been difficult to validate the adequacy of the underlying assumptions made upon formulation of micromechanics-based models, as well as to decide on the significance of parameters obtained by fitting a plausible empirical form against a particular set of experimental data. In this work, the focus is on the overall elastic constants and the use of the finite element method of Ch. 2 [1, 2] to assess the adequacy of two of the most widely used models, namely that of the micromechanics-based model of Tandon and Weng [44–47, 49] and the semi-empirical model of Halpin-Tsai [48, 50][i]. In Sec. 3.2.2 a comparison with measurements on well-characterized laboratory samples, showed that the finite element method gave excellent predictions for injection moulded short fibre composites. [6, 11] Therefore, the approach taken here is to use accurate in principle numerical predictions in place of measured values.

---

[i]The Halpin-Tsai equations were initially proposed for continuous fibre composites and then generalized for those with aligned short fibres. [48] While the final implementation is empirical in nature, the functional forms are conformable with the self-consistent ideas of Hill. [50]

3.3.1 Numerical

Periodic computer models comprised of a polymer matrix reinforced by 100 fully-aligned randomly-positioned non-overlapping identical fibres were studied (Fig. 3.15).

Using both glass and carbon fibres, calculations with three different polymer matrices typical of industrial short fibre composites were done (Table 3.5). Perfect adhesion was imposed at the fibre-matrix interfaces. A total of nine different combinations of fibre aspect ratio, $a = 10$, 20, and 30, and fibre volume fraction, $f = 10\%$, 20% and 30%, were studied. This parameter range is representative of most industrial injection moulded short fibre reinforced composites.

Computer models were meshed into periodic unstructured morphology-adaptive tetrahedra based quality meshes (Fig. 3.16). [2,41] The external strain was applied by changing the size and shape of the simulation box. A preconditioned conjugate-gradient solver was employed for minimizing the total strain energy as a function of the nodal displacements. [1, 2] The overall elastic constants C_{ik} were obtained on the basis of a linear response relation between the average volume stress and the strain applied. [ii]

3.3.2 Results and Discussion

Fig. 3.17 presents results on the predictive capability of the Tandon-Weng model for the overall longitudinal elastic constant, C_{11}, of short glass fibre composites with a semi-crystalline polymer matrix. One can see that the Tandon- Weng

---

[ii]Minimization runs were conducted on the mainframe *stardust.ethz.ch* cluster of PA8600 (550 MHz) processors at ETH Zürich. Typically, it took several single processor CPU hours to calculate the C_{ik} of a particular computer model.
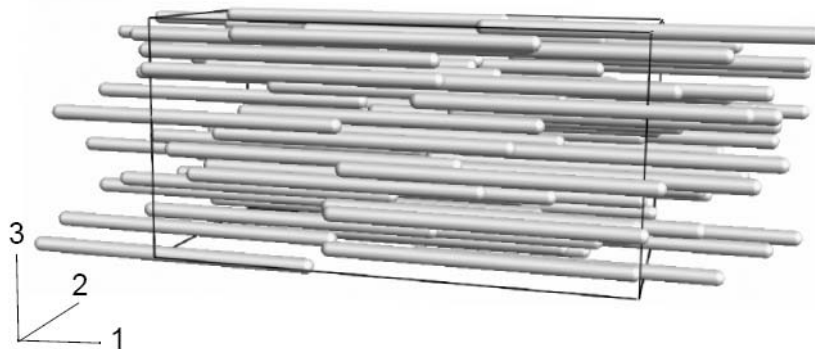
Figure 3.15: Periodic computer model comprised of 100 fully aligned randomly placed non-overlapping identical fibres of aspect ratio $a = 20$. The volume fraction is $f = 20\%$. Orthorhombic periodic boundary conditions are imposed.

Table 3.5: Matrix and fibre elastic properties. E denotes the Young's modulus and ν the Poisson's ratio. The elastic parameters of matrix M3 are typical of a glassy polymer, M1 of a solid semi-crystalline polymer at room temperature, and M01 is representative of a semi-crystalline polymer at elevated temperature. For glass fibres the elastic parameters of E-glass were taken while for carbon fibres those of highly anisotropic fibre-symmetry Courtaulds H370 fibres were used. The index numbering system for carbon fibres follows Fig. 3.15. For example, G_{12} denotes the shear modulus in the 12-plane.

	E [GPa]	ν
M3	3	0.35
M1	1	0.40
M01	0.1	0.45
Glass fibres	70	0.20
Carbon fibres	$E_{11} = 370$	$\nu_{21} = 0.35$
	$E_{22} = 12$	$\nu_{23} = 0.48$
	$G_{12} = 17.5$	
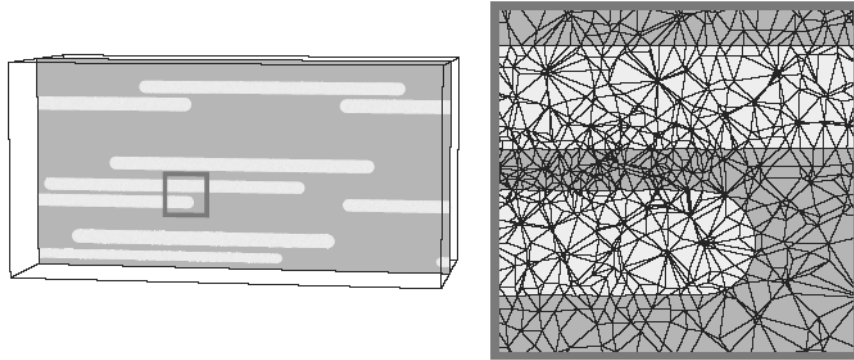
Figure 3.16: 2D cut through the periodic computer model shown in Fig. 3.15 (left). One can notice that the fibre sections sketched as spreading outside the simulation box in Fig. 3.15 are now entering the simulation box from the opposite side. Both visualization modes are equally consistent under periodic boundary conditions, as in the first case one performs visualization based on the fibre center-of-mass positions while in the second case on the tetrahedra center-of-gravity coordinates. 2D cut through the periodic tetrahedra-based mesh employed for predicting the overall elastic constants C_{ik} numerically (right). The same fragment as shown in the left image. The meshes typically consisted of a million nodes and several million tetrahedra.

model is very accurate for the cases of high fibre aspect ratios and low fibre loadings. This observation is consistent with the model's underlying assumptions, as the model was derived under a dilute condition and it was shown that it delivered the proper asymptotic predictions for the limiting case of infinitely long fibres. [43,46] The model's predictions become, however, progressively less reliable for composites comprised of shorter fibres dispersed at higher loadings.

Fig. 3.18 shows further results on the predictive capability of the Tandon-Weng model, for a variety of glass fibre reinforced composites. It is seen that the model gives quite accurate predictions for the C_{12} and C_{23} elastic constants, satisfactory predictions for the transverse C_{22} elastic constant, but delivers less reliable predictions for the longitudinal C_{11} and shear C_{44} elastic constants, especially with increasing difference between the fibre and matrix stiffness.

Table 3.6 provides an overview of the predictive capability of the Tandon-Weng (the Qiu-Weng version for anisotropic carbon fibres) and Halpin-Tsai models. The standard matrix norm error is calculated to compare the predictions.[iii] One can see that for glass fibre composites with a glassy polymer

---

[iii] The standard matrix norm is defined as $\|C\| = \sqrt{\sum C_{ik} \cdot C_{ik}}$ with the summation carried out over indices i and k running from 1 to 6. As the standard matrix norm tends to smooth all extreme deviations in the individual C_{ik} components, a low error is a necessary rather
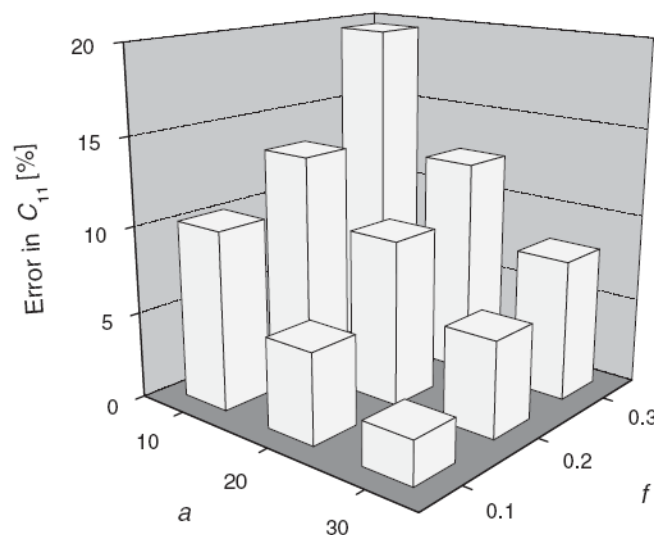
Figure 3.17: Comparison between numerical and Tandon-Weng predictions for the overall longitudinal elastic constant C_{11} of glass fibre composites with matrix M1. In the figure, a denotes the fibre aspect ratio and f the fibre volume fraction. The relative error is defined as $(C_{11}^{num} - C_{11}^{TW})/C_{11}^{num}$. The elastic parameters of matrix M1 and the range of a and f studied are typical of most widely used in industry short glass fibre composites with commodity polymer matrices (polypropylene, polyethylene, etc.).
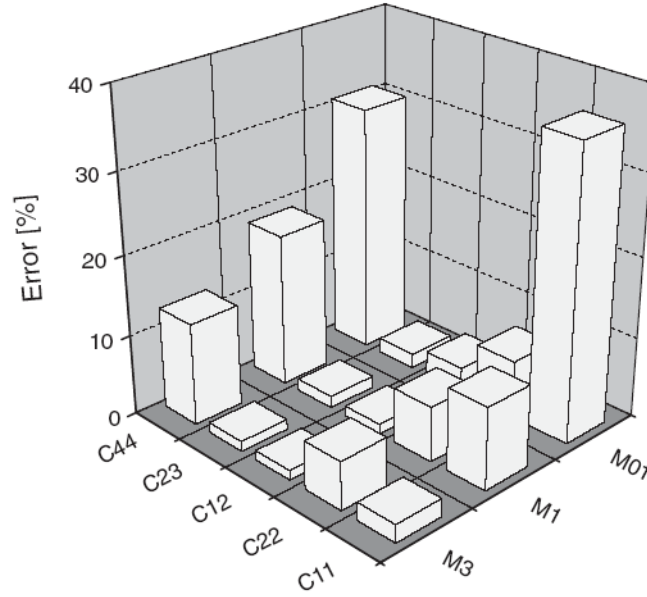
Figure 3.18: Comparison between numerical and Tandon-Weng predictions for the overall elastic constants of glass fibre composites. Each bar is an average over nine individual error estimates obtained with a particular matrix reinforced by fibres with aspect ratios $a = 10$, 20, and 30 dispersed at volume fractions $f = 10\%$, 20% and 30%. For example, the bar with labels M1 and C_{11} is an average over the nine error estimates shown in Fig. 3.17.

Table 3.6: Accuracy assessment for the Tandon-Weng and Halpin-Tsai predictions. The standard matrix norm errors, $\|\Delta C\|/\|C\|$, between numerical and model predictions are analyzed. All error estimates are given in percent relative to the numerical results. Each individual error estimate is an average of those obtained with nine combinations of fibre aspect ratios a and volume fractions f studied in this chapter (Fig. 3.17). In the parentheses, the maximal error among these nine individual standard matrix norm error estimates is also shown. For the adjustable parameters of the Halpin-Tsai equations, literature recommended values were used. [5, 32] The Halpin-Tsai predictions are obviously unsatisfactory, mostly due to poor predictions for the transverse Poisson's ratio ν_{23}. [11]

| | Tandon-Weng | Qiu-Weng | Halpin-Tsai | |
	glass	carbon	glass	carbon
M3	4 (7)	13 (21)	40 (103)	28 (35)
M1	11 (17)	26 (33)	45 (127)	45 (57)
M01	32 (46)	40 (61)	50 (89)	60 (76)

matrix (M3) the Tandon-Weng model delivers reliable results, with an accuracy appropriate for engineering design purposes. However, the model predictions become less accurate for the most widely industrially used glass fibre composites with semi-crystalline matrices (M1 and M01). For carbon fibre composites, the Qiu-Weng predictions are considerably less accurate than the corresponding Tandon-Weng ones for glass fibre composites. One can also see that the predictions of the semi-empirical Halpin-Tsai model are systematically less accurate than those of the Tandon-Weng model.

Regarding the relation to 'real' materials, as neither of the two models considered nor the numerical finite element method include the interfacial layers, one can express concern for the adequacy of both of the routes for the stiffness predictions. To this important point, the results of the validation program in Sec. 3.2 and in [11] have indicated that for all 'real' continuous fibre and short fibre composites studied at the University of Leeds the finite element method gave excellent stiffness predictions, without any explicit account for the presence of interface layers. A further issue to be addressed is whether there is any molecular orientation in the matrix phase, as a consequence of the processing route particularly when injection moulding is used. Detailed experimental studies of injection moulded glass-fibre polypropylene-matrix samples, conducted in Leeds by using Wide Angle X-Ray Diffraction (WAXS), [51] showed that while molecular orientation was seen for some unfilled polypropylene samples, this was never prevalent in glass filled samples, under the same industrially employed processing conditions. The validation study in Sec. 3.2 showed excellent agreement between experimental measurements and numerical predictions assuming an isotropic matrix. [6] The effect of the fibre length distribution was also considered , [5] and it was demonstrated that one can obtain accurate stiffness and thermal expansion predictions by replacing the 'real', measured fibre length distribution with a monodispersed, number average fibre length L_N.

3.4 Fibre Orientation State

In short fibre composites the material properties such as stiffness and thermal expansion depend strongly on the local fibre orientation state. The full information about the orientation of all the fibres in the composite is contained in the orientation distribution function (3.4.1). An alternative and much more concise description can be given with orientation tensors (3.4.2). Orientation tensors can be used to calculate the orientation averaged properties from the properties of fully aligned composites (3.4.3).

---

than a sufficient condition for the all round adequacy.

3.4.1 Orientation distribution function

The orientation of a single fibre can be described by the two angles θ and ϕ as defined in Fig. 3.19. The angles θ and ϕ can be measured experimentally by analyzing the elliptical form of cut fibres in polished cross-sections of a composite material. [4, 27, 37, 52, 53]
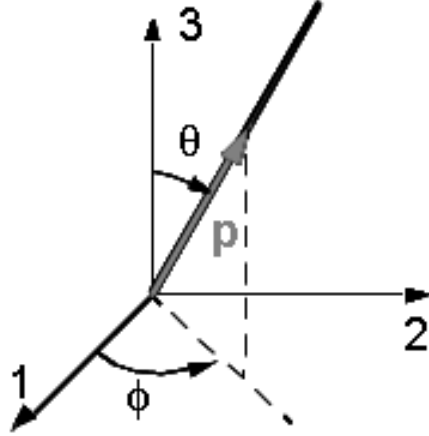
Figure 3.19: The orientation of a single fibre is defined by the two angles θ and ϕ. Alternatively, the unit vector $\mathbf{p}$ with components p_1, p_2 and p_3 can be used.

The orientation state of an ensemble of fibres at a certain point in space can then be described by a probability distribution function, $\psi(\theta, \phi)$, which is defined in such a way that the probability of finding a fibre with orientation angles between θ_1 and $(\theta_1 + \mathrm{d}\theta)$, and ϕ_1 and $(\phi_1 + \mathrm{d}\phi)$ is given by [54]

$$P(\theta_1 \leq \theta \leq \theta_1 + \mathrm{d}\theta, \phi_1 \leq \phi \leq \phi_1 + \mathrm{d}\phi) = \psi(\theta_1, \phi_1) \sin\theta_1 \mathrm{d}\theta \mathrm{d}\phi \qquad (3.5)$$

Instead of using the two angles θ and ϕ an equivalent description of the orientation of a single fibre is a unit vector $\mathbf{p}$ which is parallel to the fibre axis. The distribution function can therefore also be written as $\psi(\mathbf{p})$, where the components of $\mathbf{p}$ are related to the angles θ and ϕ as follows,

$$p_1 = \sin\theta\cos\phi \qquad (3.6)$$
$$p_2 = \sin\theta\sin\phi \qquad (3.7)$$
$$p_3 = \cos\theta \qquad (3.8)$$

Since $\mathbf{p}$ is a unit vector (i.e. its length is one) the three components of $\mathbf{p}$ are inter-related by $p_i p_i = 1$.[iv] The set of all possible directions of $\mathbf{p}$ corresponds

---

[iv]The Einstein summation convention is used throughout this section, i.e. summation over repeated indices is implied

to the unit sphere. The integral over the surface of the unit sphere (or over all possible directions of $\mathbf{p}$) is written as

$$\oint d\mathbf{p} = \int_{\phi=0}^{2\pi} \int_{\theta=0}^{\pi} \sin\theta d\theta d\phi \tag{3.9}$$

The probability distribution function must satisfy two physical conditions. First, the fibres do not possess an identified direction, i.e. a fibre with orientation angles (θ, ϕ) is not distinguishable from one with $(\pi - \theta, \phi + \pi)$, and therefore

$$\psi(\mathbf{p}) = \psi(-\mathbf{p}) \tag{3.10}$$

Second, the probability distribution function ψ must be normalized. That is

$$\oint \psi(\mathbf{p}) d\mathbf{p} = 1 \tag{3.11}$$

The orientation distribution function, ψ is a complete description of the orientation state of a collection of fibres. However, it has the disadvantage that it is quite cumbersome to handle, especially if one wants to implement it in a numerical method. It would therefore be preferential to use a more concise description of the orientation state.

3.4.2 Orientation Tensors

Such a concise description does indeed exist in the form of orientation tensors. [52, 54] An infinite set of orientation tensors exists. Here, the discussion is restricted to the second and fourth order orientation tensors. It should be noted that the odd-order orientation tensors are zero because the distribution function is even (eq. 3.10). The second order orientation tensor is determined by forming dyadic products with all possible orientation unit vectors $\mathbf{p}$ and integrating the product of the resulting tensors with the distribution function $\psi(\mathbf{p})$ over all possible directions of $\mathbf{p}$. [54] The second and fourth order orientation tensors are:

$$a_{ij} = \langle p_i p_j \rangle = \oint p_i p_j \psi(\mathbf{p}) d\mathbf{p} \tag{3.12}$$

$$a_{ijkl} = \langle p_i p_j p_k p_l \rangle = \oint p_i p_j p_k p_l \psi(\mathbf{p}) d\mathbf{p} \tag{3.13}$$

The indices i, j, k, l run from 1 to 3. From the definition (eq. 3.12, eq. 3.13) it is immediately clear that the orientation tensors are symmetric, for example

$$a_{ij} = a_{ji} \tag{3.14}$$

and from the fact that $\mathbf{p}$ is a unit vector, it follows that

$$a_{ii} = 1 \tag{3.15}$$

Moreover, higher order tensors contain complete information about lower orders, for example

$$a_{ijkk} = a_{ij} \tag{3.16}$$

The second and fourth order orientation tensors consist of 6 and 15 independent components, respectively. If the principle axis of the tensor coincide with the axis of the coordinate system, all off-diagonal elements of the tensor become zero and therefore the number of non-zero elements reduces to 3 and 6, respectively. The number of independent components is reduced to 2 for the second order tensor because of eq. 3.15.

3.4.3 The Orientation Averaging Scheme

Orientation tensors play an important role in orientation averaging. Consider any tensor property $\mathbf{T}(\mathbf{p})$ of a unidirectional microstructure aligned in the direction of $\mathbf{p}$. $\mathbf{T}$ must be transversely isotropic with $\mathbf{p}$ as its axis of symmetry. $\langle \mathbf{T} \rangle$ is the orientation average of $\mathbf{T}$ and is defined as

$$\langle \mathbf{T} \rangle = \oint \mathbf{T}(\mathbf{p})\psi(\mathbf{p})\mathrm{d}\mathbf{p} \tag{3.17}$$

Now, as an example, consider a second order tensor, $T_{ij}(\mathbf{p})$. In order to be transversely isotropic this tensor must be of the form

$$T_{ij}(\mathbf{p}) = A_1 p_i p_j + A_2 \delta_{ij} \tag{3.18}$$

where the A_i are scalar constants and δ_{ij} denotes the Kronecker tensor. The orientation average of $T_{ij}(\mathbf{p})$ is

$$\langle T \rangle_{ij} = A_1 \langle p_i p_j \rangle + A_2 \langle \delta_{ij} \rangle \tag{3.19}$$
$$= A_1 a_{ij} + A_2 \delta_{ij} \tag{3.20}$$

This demonstrates that the orientation average of a material property that is described by a second order tensor, e.g. the dielectric constant, is completely defined by the second order orientation tensor, and by the underlying unidirectional property tensor. [54]

A similar relation exists for fourth order tensors. Consider a tensor with the symmetry of the elasticity tensor (e.g. elastic stiffness, elastic compliance, or viscosity), i.e.

$$T_{ijkl} = T_{jikl} = T_{ijlk} = T_{klij} \tag{3.21}$$

To be transversely isotropic with symmetry axis $\mathbf{p}$, the tensor must have the form

$$
\begin{aligned}
T_{ijkl}(\mathbf{p}) = {} & B_1(p_i p_j p_k p_l) \\
& + B_2(p_i p_j \delta_{kl} + p_k p_l \delta_{ij}) \\
& + B_3(p_i p_k \delta_{jl} + p_i p_l \delta_{jk} + p_j p_l \delta_{ik} + p_j p_k \delta_{il}) \\
& + B_4(\delta_{ij}\delta_{kl}) + B_5(\delta_{ik}\delta_{jl} + \delta_{il}\delta_{jk})
\end{aligned}
\tag{3.22}
$$

The B_i are five scalar constants that are related to the five independent components of a transversely isotropic tensor. The orientation average of $T_{ijkl}(\mathbf{p})$ is then [54]

$$
\begin{aligned}
\langle T \rangle_{ijkl} = {} & B_1(a_{ijkl}) \\
& + B_2(a_{ij}\delta_{kl} + a_{kl}\delta_{ij}) \\
& + B_3(a_{ik}\delta_{jl} + a_{il}\delta_{jk} + a_{jl}\delta_{ik} + a_{jk}\delta_{il}) \\
& + B_4(\delta_{ij}\delta_{kl}) + B_5(\delta_{ik}\delta_{jl} + \delta_{il}\delta_{jk})
\end{aligned}
\tag{3.23}
$$

For the case of the elastic stiffness tensor C_{ijkl} the five constants $B_1, ..., B_5$ are related to the components of the C_{ijkl} of a composite with fully aligned fibres. In the contracted notation they are [31]

$$
\begin{aligned}
B_1 &= C_{11} + C_{22} - 2C_{12} - 4C_{66} \\
B_2 &= C_{12} - C_{23} \\
B_3 &= C_{66} + 1/2(C_{23} - C_{22}) \\
B_4 &= C_{23} \\
B_5 &= 1/2(C_{22} - C_{23})
\end{aligned}
\tag{3.24}
$$

Although the thermal expansion is characterized by a second order tensor, α_{ij}, it is directly connected to the elastic properties of a material. Thus the orientation averaging of the thermal expansion tensor requires the fourth order orientation tensor. The orientation averaged thermal expansion is given by

$$
\begin{aligned}
\langle \alpha_{ij} \rangle &= \langle C_{ijkl}\alpha_{kl} \rangle \langle C_{ijkl} \rangle^{-1} \\
&= \langle C_{ijkl}\alpha_{kl} \rangle \langle S_{ijkl} \rangle \\
&= (D_1 a_{ij} + D_2 \delta_{ij}) \langle S_{ijkl} \rangle
\end{aligned}
\tag{3.25}
$$

where D_1 and D_2 are two invariants that depend on the elastic and thermal expansion tensors of the unidirectional composite [31][v]

$$
\begin{aligned}
D_1 &= A_1(B_1 + B_2 + 4B_3 + 2B_5) + A_2(B_1 + 3B_2 + 4B_3) \\
D_2 &= A_1(B_2 + B_4) + A_2(B_2 + 3B_4 + 2B_5)
\end{aligned}
\tag{3.26}
$$

---

[v]One should double the B_5 term in all expressions for the thermal expansion coefficients.

where $B_1, ..., B_5$ are defined in eq. 3.24 and

$$A_1 = \alpha_1 - \alpha_2$$
$$A_2 = \alpha_2$$

$$(3.27)$$

3.5 Prediction of Stiffness and Thermal Expansion by the Orientation Averageing Scheme

It is fairly common in practice that during injection moulding, the mould filling process results in non-uniform fibre orientation distributions in the final injection moulded short fibre reinforced composite part. [52] Consequently, one needs to be able to deal with spatially non-uniform elastic constants in order to describe the structural performance of the part. This is, in principle, no problem for the finite element methods of structural analysis [24,55], provided that all the elastic constants for all the mesh elements across the part are known. Advani and Tucker [54] proposed an extension of the laminate analogy of Halpin-Pagano [56], such that the elastic constants of a short fibre composite with any given fibre orientation distribution can be obtained by averaging the elastic constants of a composite with fully aligned fibres, weighted by the fibre orientation distribution. It would be very attractive to employ this orientation averaging scheme to form predictions for the design of short fibre reinforced composite parts, should this scheme be accurate enough. Here, our finite element method [1,2] is applied to directly predict the stiffness and thermal expansion of several hundred multi-fibre computer models with a variety of different predefined fibre orientation states. The direct predictions are compared with those obtained by using the orientation averaging scheme and demonstrate that the orientation averaging scheme delivers reliable, engineering accuracy predictions.

Orientation averaging of the elastic properties described in eq. 3.23] involves fast arithmetic operations and allows for a quick evaluation of $\langle C_{ijkl} \rangle$ for all the mesh elements during the finite element assembly stage. [24,54]

3.5.1 Numerical

Periodic computer models comprising 150 non-overlapping fibres with predefined second order orientation tensors a_{ij} were studied (Fig. 3.20). In each model the fibre orientation state was adjusted to a specific second order orientation tensor a_{ij} of diagonal form following a regular grid with a spacing of $\Delta a = 0.1$. Since $a_1 + a_2 + a_3 = 1$ and all $a_i \geq 0$, only 13 grid points are in fact symmetry independent. To generate a model with a given tensor a_{ij}, a MC-run was conducted with a set of 150 isolated fibres, by changing the Euler angles of the fibres and accepting new configurations whenever they progressed the

system towards the desired orientation state. Then, the fibres were placed with the so-assigned Euler angles inside a large periodic box, and during a variable box-size MC-run the fibres were displaced and the box size steadily decreased towards the desired fibre volume fraction. At this stage, fibre orientations were kept constant and all configurations with fibre overlaps were rejected.

Computer models were then meshed into periodic tetrahedra-based morphology-adaptive quality meshes (Fig. 3.21). [2,41] Assuming typical elastic properties for the fibres and the matrix, (Table 3.5), the elastic constants of a
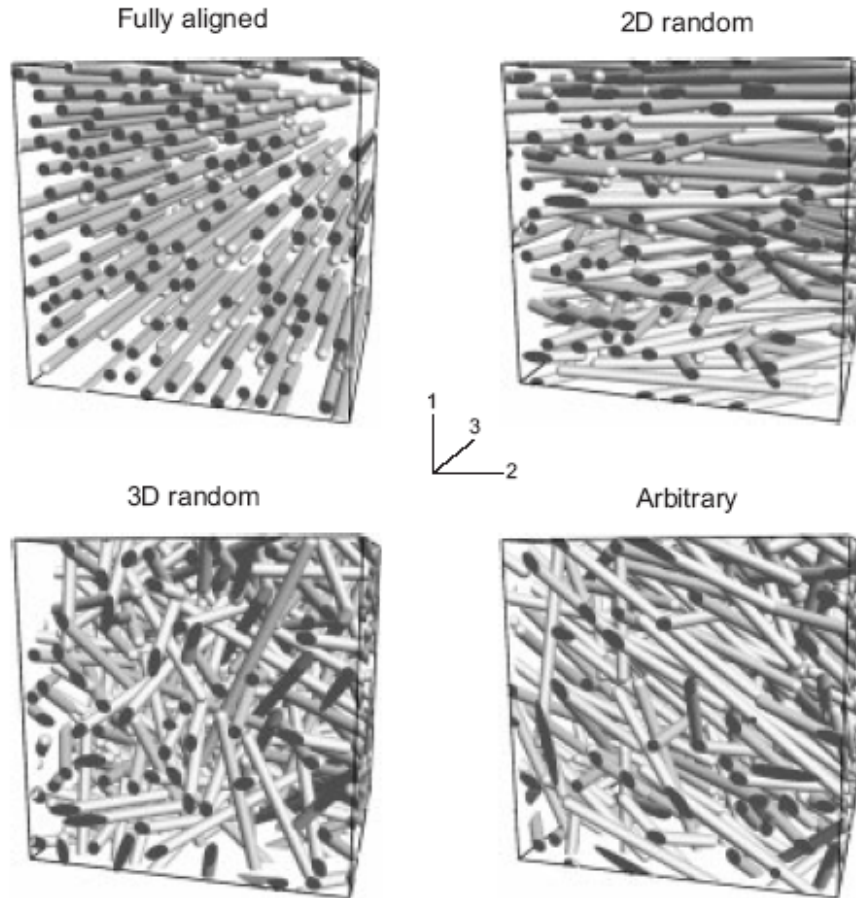
Figure 3.20: Four different orientation states of short fibre composites. Periodic computer models with 150 non-overlapping identical fibres of aspect ratio $a = 20$ are shown. The fibre volume fraction is $f = 15\%$. In the coordinate frame shown, the models have diagonal second order orientation tensors a_{ij} defined by three eigenvalues $\{a_1, a_2, a_3\}$. The model with fully aligned fibres has eigenvalues $\{0, 0, 1\}$, the 2D-random model $\{0, 0.5, 0.5\}$, the 3D-random model $\{0.33, 0.33, 0.33\}$, and the arbitrary model $\{0.6, 0.3, 0.1\}$.

large number of computer models were predicted. [1, 2, 5]
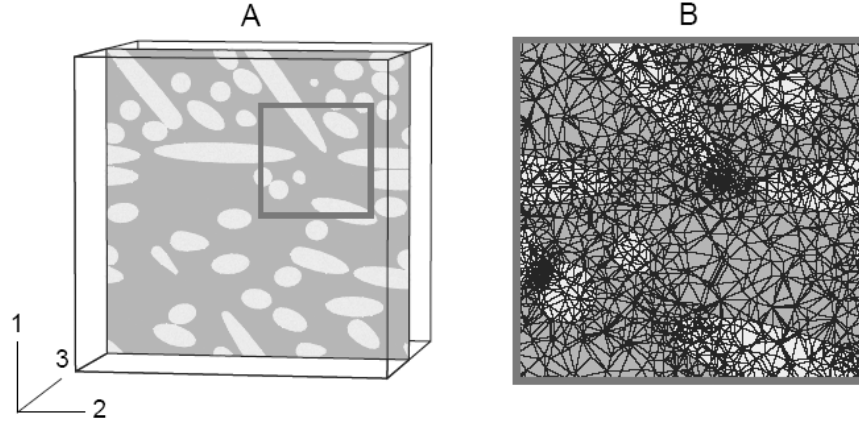
Figure 3.21: **A**: 2D cut through a computer model with a fibre orientation state described by the second order orientation tensor a_{ij} with eigenvalues $\{0.6, 0.3, 0.1\}$ (cf. Fig. 3.20). In the cutting plane, circular fibres appear as ellipses, with the two semi-axes defined by the fibres' orientation relative to the cutting plane. This sort of information is typically used for experimental characterization of fibre orientation states, based on digitized image frames obtained from polished sections of laboratory short fibre composite samples. [37] **B**: Magnified fragment of the 2D cut through the three dimensional morphology-adaptive tetrahedra-based mesh used for predicting the properties of this computer model numerically. The fragment is marked accordingly in part A. Periodic meshes typically consisted of a few million nodes and several million tetrahedra.

3.5.2 Results and Discussion

Direct numerical predictions were compared with the obtained by using the orientation averaging scheme of eq. 3.23. The needed invariants $B_1, ..., B_5$ of eq. 3.23 were calculated from the $\langle C_{ijkl} \rangle$ of the computer models with fully aligned fibres using eq. 3.24.

Fig. 3.22 presents results for glass fibre composites with a typical commodity polymer matrix (M1). One can see that the orientation averaging predictions agree remarkably well with direct numerical results, with a largest error of about 3% seen for a 2D-random planar orientation state. Table 3.7 provides a summary of the error assessment, over all the orientation states studied. One can see that the orientation averaging is highly suitable for predicting the $\langle C_{ijkl} \rangle$ of short glass fibre composites. Although short glass fibre reinforced composites are the most widely used in industry today, short carbon fibre reinforcement is also used. Similar orientation averaging predictions have been produced for carbon
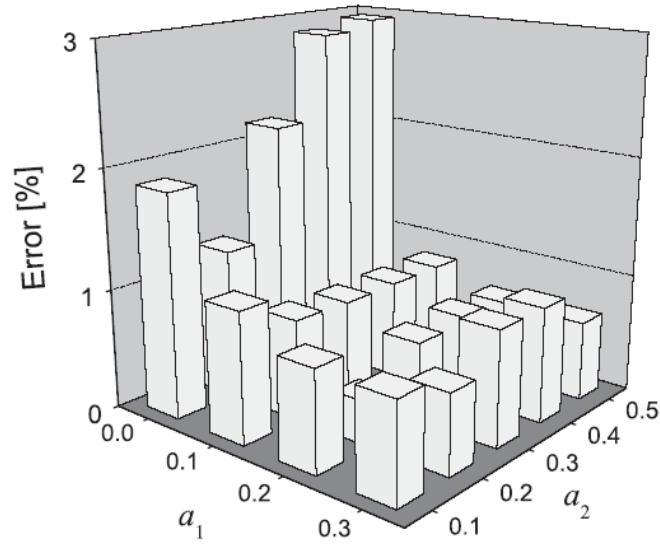
Figure 3.22: Relative standard matrix norm error between direct and orientation averaging predictions. Results for a composite with glass fibres of aspect ratio $a = 20$ dispersed in matrix M1 at a volume fraction of $f = 15\%$ are shown. The error assessment is carried out based on computer models with predefined second order orientation tensors. Diagonal form tensors are considered and a regular grid with a spacing of $\Delta a = 0.1$ is used. Only 13 grid points are in fact symmetry independent. All of them are shown in the figure, together with 7 additional symmetry equivalent points included for visual expediency.

Table 3.7: Accuracy assessment for the orientation averaging predictions. The standard matrix norm errors, $\|\Delta C\|/\|C\|$ and $\|\Delta\alpha\|/\|\alpha\|$, between direct and orientation averaging predictions for the elastic constants and thermal expansion coefficients are shown. Here results for composites with fibres of aspect ratio $a = 20$ dispersed at a volume fraction of $f = 15\%$ are listed. Each error estimate shown in this table is an average over the estimates obtained with computer models of all the predefined second order orientation tensors studied, see Figure 20. All error estimates are given in percent relative to the direct numerical predictions. The accuracy assessment for composites with $a = 30$ and $f = 10\%$ and $a = 10$ and $f = 30\%$ has shown results which are very similar to those presented in this table.

	Glass fibres			Carbon fibres		
Matrix	M3	M1	M01	M3	M1	M01
$\|\Delta C\|/\|C\|$	1.1	1.9	3.3	6.1	8.4	5.6
$\|\Delta\alpha\|/\|\alpha\|$	3.4	2.5	1.2	5.4	7.6	8.7

fibre composites. The results are also shown in Table 3.7, and although less accurate than the glass fibre predictions, they still suggest that the orientation averaging scheme is satisfactory for most practical purposes.

As an alternative, one can predict the elastic constants by the inversion of the elastic compliances $\langle S_{ijkl}\rangle$ obtained by averaging the S_{ijkl} of a composite with fully aligned fibres. The same eq. 3.23 can readily be used for this purpose, with the scalar constants $B_1, ..., B_5$ calculated from the S_{ijkl} components. [43] This calculation was checked and it was found that this alternative averaging scheme resulted in very poor predictions, typically with 20-60% standard matrix norm errors, depending on the particular orientation state and fibre fraction.

For glass fibres, one commonly assumes isotropic elastic behavior. As a result, any glass fibre composite with a uniform matrix can be viewed as a two phase composite and one can therefore use the explicit formula of Levin

$$\alpha_i = (\alpha_k^{(1)} - \alpha_k^{(2)})(S_{kl}^{(1)} - S_{kl}^{(2)})^{-1}(S_{li} - S_{li}^{(2)}) + \alpha_i^{(2)} \tag{3.28}$$

to predict the overall thermal expansion coefficients α_{ij}. [43,57] The superscripts (1) and (2) stand for the fibre and matrix phase, respectively. The situation is, however, different for carbon fibre composites, as carbon fibres are anisotropic and differently oriented fibres have generally different laboratory-frame elastic constants. As thermal expansion of three and more phase composites is no longer uniquely determined by the overall elastic constants, [43, 57] the accuracy of orientation averaging predictions was assessed. [31] For this purpose, directly predicted tensors α_{ij} were compared with those obtained by using the orientation averaging scheme for the thermal expansion described by eq. 3.4.3.

Table 3.7 provides a summary of the relative standard matrix norm error for all fibre and matrix types. For completeness, predictions for glass fibre composites are also given. Overall, the results for the thermal expansion are in concert with those seen for the elastic constants: the orientation averaging gives excellent predictions for glass fibre composites and relatively less accurate but still satisfactory results for carbon fibre composites.

3.6 Conclusions

In this chapter the application of different micromechanical models and of the finite element method of Ch. 2 to predict the thermoelastic properties of short fibre reinforced composites was studied. Numerical predictions for computer models with parallel fibres with a fibre length distribution were compared to single aspect ratio predictions. It was found that best predictions are achieved by replacing the fibre length distribution with the number average length.

Injection moulded samples usually show some degree of fibre misalignment. The measured orientation distribution was sampled by a Monte Carlo procedure to create computer models that match the real distribution. Numerically predicted properties of these composites were in excellent agreement with experimental data. Of the micromechanical models investigated the best result could be achieved by using the model of Tandon and Weng in conjunction with the laminate theory.

A set of microstructures of aligned short fibres was generated at three different volume fractions and three different fibre aspect ratios. The thermoelastic properties for three typical polymeric matrices with glass and carbon fibres respectively, were calculated numerically as well as with the models of Tandon-Weng and Halpin-Tsai. Tandon-Weng resulted in the best estimates but in some cases the error was still very large, especially for matrices with a lower stiffness and a higher Poisson's ratio, such as semi crystalline thermoplasts at elevated temperature. So one should not rely on micromechanical models to predict the properties of fully aligned composites. This is especially important if these predictions are used as basis for an orientation averaging.

The thermoelastic properties of composites with arbitrarily defined fibre orientations have been directly calculated by the finite element procedure. Alternatively, these properties were predicted by orientation averaging of the results with fully aligned composites. It was seen that the orientation averaging gives results with an accuracy that is sufficient for most practical applications provided the properties of the fully aligned composite are accurately predicted. As mentioned above, this is best done by direct numerical calculations.

Summarizing, the accuracy of the finite element method was validated against experimental results. It was demonstrated that the properties of short fibre

composites with arbitrary fibre orientation can be calculated by orientation averaging of numerical predictions for fully aligned composites, which consists of fast arithmetic operations. It can therefore implemented in the process displayed in Fig. 3.3 to allow for accurate and efficient design of short fibre reinforced composite parts.

4 Comparison of Grid-based Finite Element Method with Unstructured Mesh Finite Element Method

4.1 Introduction

The finite element method described in Ch. 2 [1,2] uses a Monte Carlo method to create models of (random) microstructures of multiphase composite materials. Morphology adaptive tetrahedra-based periodic meshes are built on the microstructure. [10] The solution is found numerically with an iterative preconditioned conjugate gradient solver. [25] The versatility of this method has been shown on a number of different examples. [5–9,11–14,17,18,58,59] Its accuracy has been validated against a wide range of experimental data. [6,11,58]

Recently, a modified version of his method has been developed (see Ch. 2). [3, 22] Instead of using unstructured morphology adaptive meshes it uses a regular grid of cubic elements. [24] Intuitively, one would expect that the accuracy of the results depends on the grid resolution. It needs to be fine enough to resolve the essential features of the microstructure. So one should generally expect to use a larger number of elements as compared to morphology adaptive meshes because the fine grid resolution needs to be applied over the whole microstructure. However, the grid based method has the advantage that it is possible to directly use microstructural data that is acquired in a grid format, such as e.g. microtomography data (see Ch. 5, Ch. 7 & Ch. 8). Moreover it is possible to use mixed formulation finite element solvers which are necessary when incompressible materials (rubber) are studied. [60]

In this chapter, the goal is to establish the accuracy of the predictions made by the grid-based method by comparing whether they are in accordance with the results from the unstructured mesh method, whose accuracy has been demonstrated before. [6,11,58]

To this end, random microstructures consisting of spheres, platelets, and spherocylinders, respectively were built at different volume fractions. Their thermoelastic properties were calculated with both the unstructured mesh and the grid

based version of the finite element method, and the results were compared.

4.2 Numerical

Random microstructures consisting of 64 identical non-overlapping spheres, platelets, and spherocylinders, respectively, were generated with a Monte Carlo procedure in a cubic unit cell. [23] For spherical inclusions two different microstructures for each of the three volume fractions $f = 10$, 20 and 30 vol.% were generated while for spherocylinders and platelets one microstructure per volume fraction was studied. The aspect ratio of the platelets was $a = 5$ and the one of the spherocylinders was also $a = 5$.

The models were meshed with morphology-adaptive quality meshes and their stiffness tensor and thermal expansion tensor was calculated. [23] Calculations were considered as converged when the initial gradient had been reduced by a factor of 10^{-4}. For the matrix the properties of a typical semi-crystalline polymer were assumed and the inclusions were assumed to be typical for E-glass(Table 4.1). A total number of nine different microstructure was studied.

Table 4.1: Elastic properties of matrix and inclusions used for the comparison between unstructured mesh based and grid based calculations. The matrix is a typical semi-crystalline polymer at room temperature, the inclusions are E-glass.

	Matrix	Glass inclusions
E [GPa]	3	70
ν	0.35	0.2
α [10^{-6}K^{-1}]	$1 \cdot 10^{-4}$	$1 \cdot 10^{-5}$

The same nine microstructures as above were then remeshed with cubic grids of different resolutions. Grids of 50^3, 100^3, and 200^3 voxels were created. [26]

The same material properties as above were used (Table 4.1). Again the solutions were considered as converged when the initial gradient had been reduced by a factor of 10^{-4}.

In addition some short fibre composites comparable to the ones of Ch. 3 were studied. Microstructures of 100 spherocylinders with an aspect ratio of $a = 20$ at a volume fraction of $f = 10\%$ were generated with the following predefined second order orientation tensors (for details see Sec. 3.4 and Sec. 3.5.1):

$$a_{ij} = \begin{pmatrix} 1 & 0 & 0 \\ 0 & 0 & 0 \\ 0 & 0 & 0 \end{pmatrix} \tag{4.1}$$

$$a_{ij} = \begin{pmatrix} 1/3 & 0 & 0 \\ 0 & 1/3 & 0 \\ 0 & 0 & 1/3 \end{pmatrix} \quad (4.2)$$

and

$$a_{ij} = \begin{pmatrix} 1/2 & 0 & 0 \\ 0 & 1/2 & 0 \\ 0 & 0 & 0 \end{pmatrix} \quad (4.3)$$

These microstructures were also meshed with both unstructured meshes and grids with a resolution of $100^3 = 1.0 \cdot 10^6$. Glass fibres as well as high modulus carbon fibres were studied. Phase properties according to Table 4.2 were used.

Table 4.2: Matrix and fibre elastic properties. E denotes the Young's modulus and ν the Poisson's ratio. The elastic parameters of matrix M1 are typical of a solid semi-crystalline polymer at room temperature. For glass fibres the elastic parameters of E-glass were taken while for carbon fibres those of highly anisotropic fibre-symmetry Courtaulds H370 fibres were used. The index numbering system for carbon fibres follows Fig. 3.15. For example, G_{12} denotes the shear modulus in the 12-plane.

|	E [GPa]	ν
M1	1	0.40
Glass fibres	70	0.20
Carbon fibres	$E_{11} = 370$	$\nu_{21} = 0.35$
	$E_{22} = 12$	$\nu_{23} = 0.48$
	$G_{12} = 17.5$	

4.3 Results and Discussion

Unstructured meshes with spherical inclusions had about $1.5 \cdot 10^4$ to $5 \cdot 10^4$ nodes (about $9 \cdot 10^4$ to $3 \cdot 10^5$ elements). To realize good quality meshes with the anisometric inclusion types (platelets and spherocylinders) a higher number of nodes was necessary, i.e. about $1 \cdot 10^5$ to $3 \cdot 10^5$ nodes corresponding to about $7 \cdot 10^5$ to $2 \cdot 10^6$ elements.

With the cubic grids the number of nodes is equal to the number of elements. It was for a resolution of 50^3, 100^3, and 200^3 $1.25 \cdot 10^5$, $1 \cdot 10^6$, and $8 \cdot 10^6$ nodes (or elements), respectively. It can be observed that for the anisometric inclusions at the volume fractions studied here the number of elements for a good quality unstructured mesh is of the same order as the one of a grid with a resolution of 100^3 to 200^3.
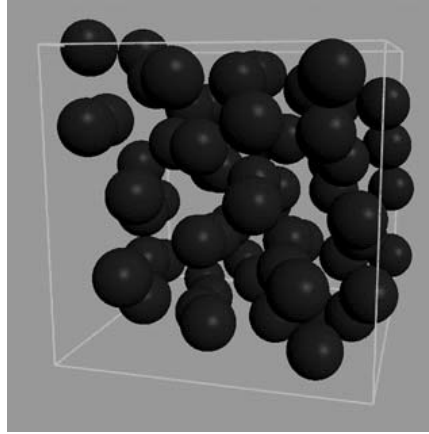
Figure 4.1: Example of a microstructure containing 64 identical non-overlapping spheres. The inclusion volume fraction is $f = 0.2$.
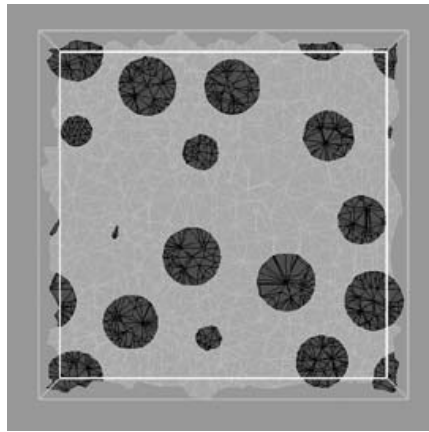
Figure 4.2: 2D cut through the morphology adaptive unstructured finite element mesh (same microstructure as in Fig. 4.1). The mesh is built of tetrahedra.
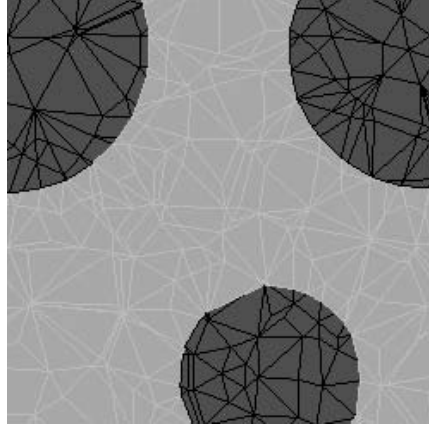
Figure 4.3: Detail of the mesh in Fig. 4.2.
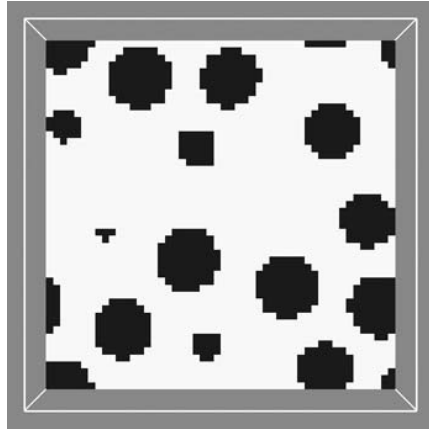
Figure 4.4: 2D cut through the grid based representation of the micostructure in Fig. 4.1. The grid resolution here is $50 \times 50 \times 50$.
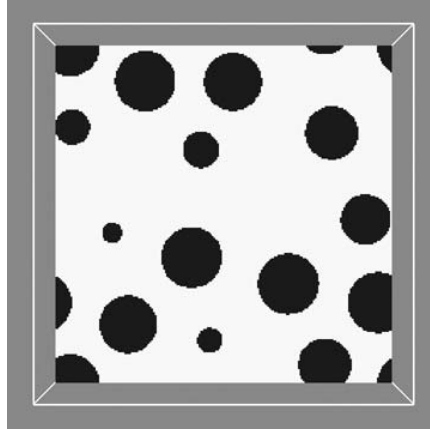
Figure 4.5: By going to a grid resolution of $200 \times 200 \times 200$ the reproduction of features is much better as compared to Fig. 4.4.

Figure 4.6: Microstructure with an isotropic fibre orientation state. The second order orientation tensor corresponds to eq. 4.2. 100 fibres with an aspect ratio of $a = 20$ at a volume fraction of $f = 0.1$.

Figure 4.7: Cut through the morphology adaptive unstructured mesh for the microstructure in Fig. 4.6.
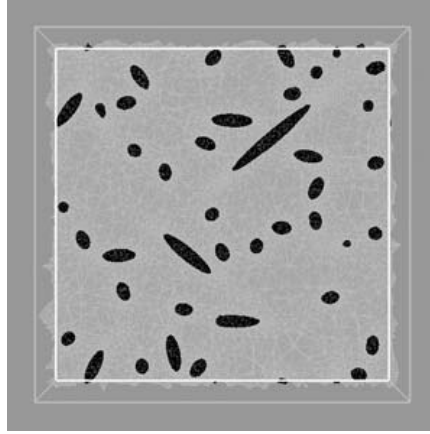

Figure 4.8: Detail of the mesh in Fig. 4.7.
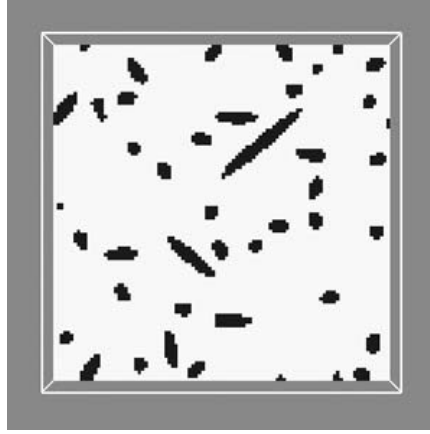
Figure 4.9: Cut through the grid representation of the microstructure in Fig. 4.6. Grid resolution $100 \times 100 \times 100$.

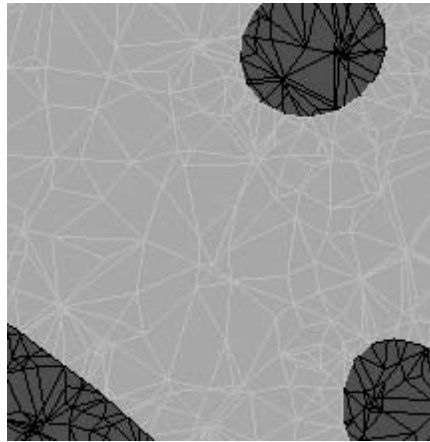**Figure 4.10:** A finer grid resolution ($200 \times 200 \times 200$) again gives a better representation, especially of curved features.

Table 4.3: Comparison between stiffness tensors, C_{ik}, predicted by grid-based method and unstructured mesh method. 64 identical glass spheres randomly dispersed in a semi-crystalline polymer matrix. The inclusion volume fraction is $f = 10$, 20 and 30%, respectively. Grid resolutions studied are 50^3, 100^3, and 200^3. Error estimates are indicated as percent deviation relative to the prediction with unstructured meshes ($\|\Delta C\|/\|C\|$ [%]). Results for two different microstructures per volume fraction are shown.

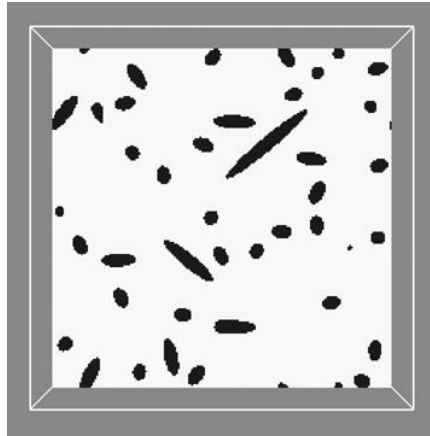|	Grid resolution		
f	50^3	100^3	200^3
10	1.0 / 1.5	2.0 / 2.5	2.6 / 3.1
20	1.6 / 1.9	2.3 / 3.4	3.3 / 4.4
30	3.3 / 2.4	2.0 / 2.7	3.4 / 4.1

Table 4.4: Comparison between thermal expansion tensors, α_{ij}. Error estimates are indicated as percent deviation relative to the prediction with unstructured meshes ($\|\Delta\alpha\|/\|\alpha\|$ [%]). Corresponding results for C_{ik} are the numbers after the slash in Table 4.3.

	Grid resolution		
f	50^3	100^3	200^3
10	0.1	0.8	1.2
20	0.9	0.6	1.3
30	2.4	0.3	0.9

The results were assessed by comparing the stiffness tensors, C_{ik}, and for the spherical inclusions also the tensor of thermal expansion, α_{ij}. The standard matrix norm errors, $\|\Delta C\|/\|C\|$ and $\|\Delta\alpha\|/\|C\alpha\|$, between the grid-based predictions and the unstructured mesh prediction have been calculated. The error estimates are given in percent relative to the unstructured mesh prediction, which is considered to give accurate results [5,6].

The results show that already at a relatively coarse grid resolution of 50^3 approximate predictions are possible within about 5% standard matrix norm error at the volume fractions studied (Table 4.3, Table 4.5, and Table 4.6). Larger errors are only observed with platelets and spherocylinders at a inclusion volume fraction of $f = 0.3$ (error about 10%) As one would intuitively expect the accuracy is improved with increasing the grid resolution to 100^3 or 200^3 in the microstructures consisting of spherocylinders or platelets (Table 4.5, Table 4.6). Surprisingly however, this trend is not observed with spherical inclusions

Table 4.5: Comparison between stiffness tensors, C_{ik}, predicted by grid-based method and unstructured mesh method. 64 identical glass spherocylinders randomly dispersed in a semi-crystalline polymer matrix. The inclusion volume fraction is $f = 10$, 20 and 30%, respectively. Grid resolutions studied are 50^3, 100^3, and 200^3. Error estimates are indicated as percent deviation relative to the prediction with unstructured meshes ($\|\Delta C\|/\|C\|$ [%]).

	Grid resolution		
f	50^3	100^3	200^3
10	2.6	0.9	0.3
20	5.1	1.8	0.6
30	9.3	3.3	1.1

Table 4.6: Comparison between stiffness tensors, C_{ik}, predicted by grid-based method and unstructured mesh method. 64 identical glass platelets randomly dispersed in a semi-crystalline polymer matrix. The inclusion volume fraction is $f = 10$, 20 and 30%, respectively. Grid resolutions studied are 50^3, 100^3, and 200^3. Error estimates are indicated as percent deviation relative to the prediction with unstructured meshes ($\|\Delta C\|/\|C\|$ [%]).

	Grid resolution		
f	50^3	100^3	200^3
10	2.9	1.2	0.4
20	5.7	2.2	0.7
30	10.3	3.8	1.2

(Table 4.3).

The errors increase with increasing volume fractions of spherocylinders and platelets (Table 4.5, Table 4.6). Again this is not observed with spherical inclusions (Table 4.3). The increasing error is probably due to the fact that interparticle distances are decreased with increasing volume fraction. Therefore the probability grows that inclusion particles are joined together because the matrix between the particles cannot be resolved by the grid. Morphology adaptive meshes are an advantage in such cases since the mesh is refined specifically in such regions of the microstructure.

For spherocylinders and paltelets at a grid resolution of 200^3 the standard matrix norm error is about 1% or less even at a volume fraction of 30%, which can be considered a very good accuracy.

The results for spherical inclusions do not show such trends as the ones for spherocylinders and platelets. The errors vary erratically beteween about 1 and 4%. It seems that this is the accuracy level that can be achieved whereas the variations are random and depend on the specific microstructure and meshing. It seems that the accuracy here is not necessarily improved by refining the grid resolution.

For the microstructures consisting of spherical inclusions the thermal expansion tensors have been predicted in addition to the stiffness tensor. The error of the grid based prediction as compared to the unstructured mesh prediction is shown in (Table 4.4). The error is smaller than for the stiffness tensor prediction – typically below 1%. There are no clear trends with volume fraction or grid resolution. This behaviour is similar to the one of the stiffness tensor predictions for composites with spherical inclusions. This is probably due to the fact that the stiffness tensor goes in the calculation of the thermal expansion tensor.

Table 4.7: Comparison between stiffness tensors, C_{ik}, and thermal expansion tensor, α_{ik}, predicted by grid-based method and unstructured mesh method. Microstructures comprise 100 identical glass fibres ($a = 20$, $f = 0.1$) in a semi-crystalline polymer matrix. The grid resolution is $100 \times 100 \times 100$. Error estimates are indicated as percent deviation relative to the prediction with unstructured meshes ($\|\Delta C\|/\|C\|$ [%] and $\|\Delta \alpha\|/\|\alpha\|$ [%], respectively).

orientation tensor			error	
a_{11}	a_{22}	a_{33}	$\|\Delta C\|/\|C\|$ [%]	$\|\Delta \alpha\|/\|\alpha\|$ [%]
1	0	0	0.9	0.7
1/3	1/3	1/3	0.8	0.7
1/2	1/2	1/2	1.0	2.2

Table 4.8: Comparison between stiffness tensors, C_{ik}, and thermal expansion tensor, α_{ik}, predicted by grid-based method and unstructured mesh method. Microstructures comprise 100 identical carbon fibres ($a = 20$, $f = 0.1$) in a semi-crystalline polymer matrix. The grid resolution is $100 \times 100 \times 100$. Error estimates are indicated as percent deviation relative to the prediction with unstructured meshes ($\|\Delta C\|/\|C\|$ [%] and $\|\Delta \alpha\|/\|\alpha\|$ [%], respectively).

orientation tensor				
a_{11}	a_{22}	a_{33}	$\|\Delta C\|/\|C\|$ [%]	$\|\Delta \alpha\|/\|\alpha\|$ [%]
1	0	0	3.1	0.6
1/3	1/3	1/3	0.4	0.3
1/2	1/2	1/2	0.9	1.4

The calculations with short fibres of an aspect ratio of $a = 20$ show that the standard matrix norm error for both the stiffness tensor and the thermal expansion tensor does not exceed 3%. In fact, in most cases it is around 1%.

When discussing the differences between the two types of predictions one should note that the inclusion volume fraction is systematically underestimated by the unstructured mesh. This is the case because the nodes are placed on the surface of the inclusion and connected by planar surfaces. For all convex inclusion shapes necessarily the effective volume fraction is slightly below the nominal volume fraction. In turn, considering inclusions that are stiffer than the matrix this will result in some underestimation of the effective stiffness of the composite.

With the grids, this effect does not occur since the mismatch between the element and the real shape of the inclusion object can either deliver a positive or a negative contribution to the inclusion volume fraction. In the end the effective volume fraction observed was in all cases very close to the nominal one. Thus confirming the above statement.

It should therefore be expected that the stiffness predictions with the grids are closer to the correct value. However, the following fact should also be considered: morphology adaptive meshes can follow curved surfaces more smoothly than the grid which necessarily always results in stepped inclusion object surfaces. The stepped nature of interfaces may also influence the predicted properties. It is, however, not obvious what kind of effect this will have on the predicted properties of the composite.

4.4 Conclusions

It has been demonstrated that the accuracy of the grid-based method is comparable to the one of the unstructured mesh method. Generally speaking higher volume fractions will lead to larger errors because of the reduced interparticle distances which can become difficult to resolve by the grid. With spherocylinders and platelets a clear trend towards higher accuracy with increasing grid resolution is observed. With the unstructured meshes the inclusion volume fraction and therefore also the effective stiffness of the composites is systematically slightly underestimated. All in all, the predictions of the grid-based method are within about 4% or less of the predictions of the unstructured mesh method for the microstructures studied. It is therefore justified and appealing to use the grid-based method instead of the unstructured mesh method where appropriate.

5 Microtomography

Computer tomography (CT) is a powerful method which allows to determine the three dimensional (3-D) structure of objects. In principle, the method relies on measuring X-ray transmission data of the measured objects under many different angles which allows to reconstruct a cross-sectional image of the object based on mathematical reconstruction methods. 3-D microstructural information can be retrieved by applying a virtual slicing procedure to the object and putting together the independent reconstructed slices.

The mathematical foundations of CT were laid already in the early twentieth century by Radon [61]. But it required the advent of fast computers in the 1970s to apply the technique in practice when the first X-ray tomographic scanner was invented [62].

CT is popularly known mainly from medical applications where it is a very efficient tool for producing 3-D images of the human body. The spatial resolution of medical CT is rather limited due to the dose limitations of the living tissues being scanned. For non-living samples, however, these limitations do not apply and it is possible to use special equipment allowing for better spatial resolution. This is exploited in the so-called microtomography (μCT) (also known as X-ray Tomographic Microscopy (XTM)) [63]. It is a very powerful method for acquiring 3D information of structures or materials. Its field of application covers biomedical science, materials science, geophysics, archeology, industrial applications, and others [21, 64–71].

There follow some remarks about the interaction of X-rays with matter (Sec. 5.1) which are necessary to understand the principle of tomography as explained in Sec. 5.2. The advantages of synchrotron based CT are discussed in Sec. 5.3 before the instrumental setup used to measure the data for the present thesis are shortly described (Sec. 5.4).

5.1 Interaction of X-rays with Matter

X-ray photons can interact with matter in a number of different ways:

- photoelectric absorption

- coherent or Rayleigh scattering

- incoherent or Compton scattering

- electron-positron pair production.

The latter can be neglected here because it appears only above 1 MeV whereas typical X-ray energies in μCT are in the range 5-100 keV.

The total interaction of X-rays with matter is described by the linear attenuation coefficient μ. It depends on i) the photon energy E, ii) the density ρ, and iii) the atomic number Z of the investigated material.

Adding the different contributions of X-rays interacting with matter, i.e. the atomic photoelectric cross-section σ_{pe}, the coherent (Rayleigh) scattering cross-section σ_{coh}, and the incoherent (Compton) scattering cross-section σ_{incoh}, the total attenuation coefficient μ can be written in the form:

$$\mu = \frac{N_A}{A}\rho(\sigma_{pe} + \sigma_{coh} + \sigma_{incoh}) \tag{5.1}$$

where N_A is Avogadro's constant, A is the atomic weight, and ρ is the density. In the photoelectric domain the dependance of the attenuation coefficient is often described by [72]

$$\mu = K\rho\frac{Z^4}{E^3} \tag{5.2}$$

where K is a constant.

Let us consider an X-ray beam of fixed energy E passing through a homogeneous medium with a total attenuation coefficient μ and let $N(x, E)$ be the number of photons (Fig. 5.1). The number of photons interacting with the medium on a distance dx is proportional to the number of incident photons $N(x, E)$. The relation is described by the so-called Beer-Lambert law:

$$\mathrm{d}N = -\mu(E)N(x, E)\mathrm{d}x \Rightarrow N(x, E) = N_0 e^{-\mu(E)x} \tag{5.3}$$

For a heterogeneous medium where μ is a function of the position inside the medium, $\mu(x, E)$, we get

$$N(x, E) = N_0 \exp\left(-\int_0^x \mu(x', E)\mathrm{d}x'\right) \tag{5.4}$$

for the number of transmitted photons.

5.2 Principle of Tomography

Once we understand how X-rays interact with matter the question arises how we can reconstruct a cross-sectional image of a sample from transmission measurements. To answer this question we introduce two coordinate systems, i.e.
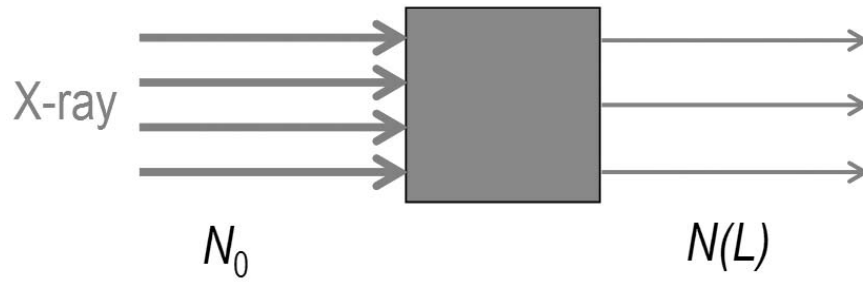
Figure 5.1: Attenuation of an X-ray beam crossing a medium with attenuation coefficient μ.
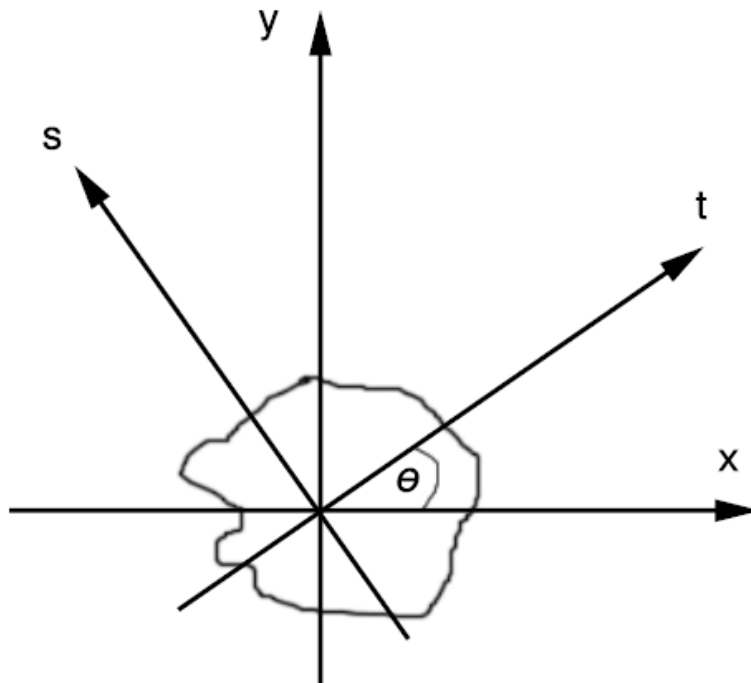
Figure 5.2: Coordinate systems used in the discussion of the principle of tomography.

a fixed laboratory system (x, y) and a second system (s, t) that moves with the sample while it is rotated (Fig. 5.2).

Let $\mu(x, y)$ be the local total attenuation coefficient of the sample which need not be homogeneous. The number of photons passing through the sample at a given angle θ at a fixed position t is then given by

$$N_\theta(t) = N_0 \exp \left(- \int_{L_{\theta,t}} \mu(x, y) \mathrm{d}s \right) \tag{5.5}$$

where $L_{\theta,t}$ is a straight line at a fixed angle θ and a fixed position t. From this one can define a projection $P_\theta(t)$ as

$$P_\theta(t) := \ln \left(\frac{N_0}{N(t)} \right) = \int_{L_{\theta,t}} \mu(x, y) \mathrm{d}s \tag{5.6}$$

The basic idea of computer tomography is to invert eq. 5.6 for many parallel projections taken over a range of different projection angles θ in order to get the two-dimensional distribution of the attenuation coefficient $\mu(x, y)$ (Fig. 5.3).

The relation between the two coordinate systems in Fig. 5.2 is given by a simple rotation about the angle θ.

$$\begin{pmatrix} t \\ s \end{pmatrix} = \begin{pmatrix} \cos \theta & \sin \theta \\ -\sin \theta & \cos \theta \end{pmatrix} \begin{pmatrix} x \\ y \end{pmatrix} \tag{5.7}$$

In the (t, s)-coordinate system, the projection $P_\theta(t)$ of an arbitrary object function $f(x, y)$ is:

$$P_\theta(t) = \int_{-\infty}^{\infty} f(t, s) \mathrm{d}s \tag{5.8}$$

Then its Fourier transform is:

$$S_\theta(\omega) = \int_{-\infty}^{\infty} P_\theta(t) e^{-2\pi i \omega t} \mathrm{d}t \tag{5.9}$$

Substituting eq. 5.8 into eq. 5.9 we get:

$$S_\theta(\omega) = \int_{-\infty}^{\infty} \int_{-\infty}^{\infty} f(t, s) e^{-2\pi i \omega t} \mathrm{d}s \mathrm{d}t \tag{5.10}$$

Using the coordinate transformation eq. 5.7, this can be transformed into the (x, y)-system:

$$S_\theta(\omega) = \int_{-\infty}^{\infty} \int_{-\infty}^{\infty} f(x, y) e^{-2\pi i \omega (x \cos \theta + y \sin \theta)} \mathrm{d}x \mathrm{d}y \tag{5.11}$$
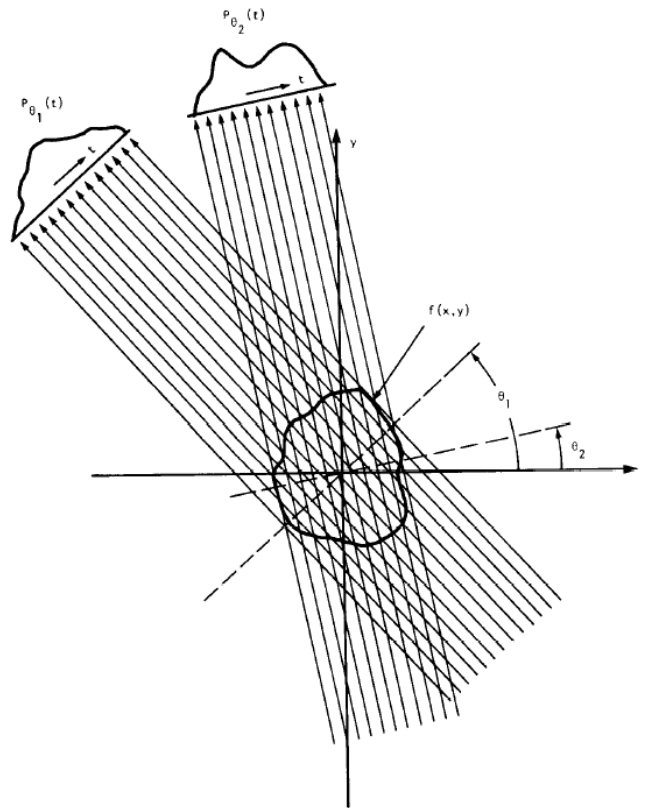
Figure 5.3: Parallel projections are taken by measuring a set of parallel rays for a number of different angles (From Ref. [73])

The right hand side of eq. 5.11 can be interpreted as the two-dimensional Fourier transform of $f(x, y)$ at a spatial frequency of $(u = \omega \cos\theta, v = \omega \sin\theta)$ or

$$S_\theta(\omega) = F(\omega, \theta) = F(x \cos\theta, y \sin\theta) \tag{5.12}$$

This equation (eq. 5.12) is the essence of straight ray CT and it proves the so-called *Fourier slice theorem* [73]:

> The Fourier transform of a parallel projection of an image $f(x, y)$ taken at angle θ gives a slice of the two-dimensional transform $F(u, v)$ subtending an angle θ with the u-axis. In other words, the Fourier transform of $P_\theta(t)$ gives the values of $F(u, v)$ along line BB in Fig. 5.4.

From eq. 5.12 and Fig. 5.4 we can see that by taking projections of an object function $f(x, y)$ at angles $\theta_1, \theta_2, \ldots \theta_n$ and Fourier transforming each of this, we can determine the values of $F(u, v)$ on radial lines. Knowing $F(u, v)$, the object function $f(x, y)$, or $\mu(x, y)$ in our specific case, can be recovered by calculating the inverse Fourier transform:

$$f(x, y) = \int_{-\infty}^{\infty} \int_{-\infty}^{\infty} F(u, v) e^{2\pi i(ux+vy)} \mathrm{d}u \mathrm{d}v \tag{5.13}$$

However, since in practice we can only measure a finite number n of projections, we will only get information on n radial lines in the frequency domain.
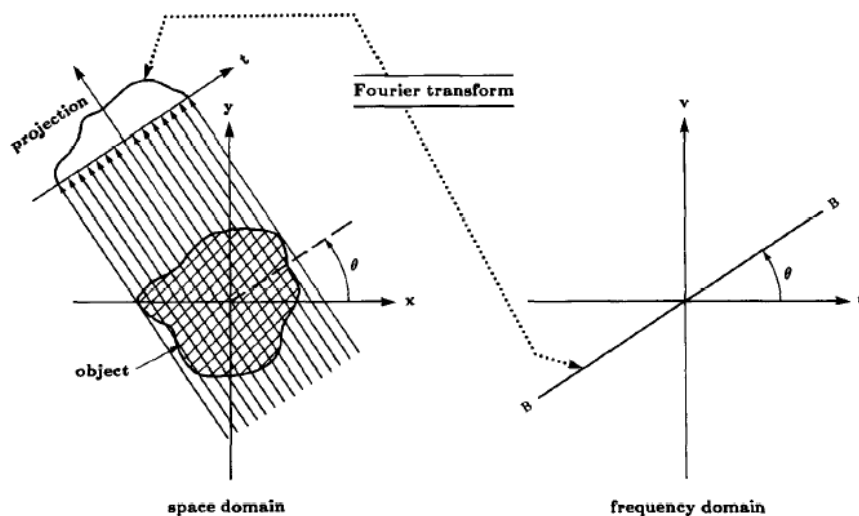
Figure 5.4: The Fourier slice theorem relates the Fourier transforms of a projection to the Fourier transform of the object along a radial line. From Ref. [73]

Interpolation procedures have to be applied to obtain the points on an Euclidean grid because the data obtained lie on a polar grid.

Filtered Backprojection

If we go to polar coordinates by substituting $u = \omega \cos \theta$ and $v = \omega \sin \theta$ in eq. 5.13, we get

$$f(x, y) = \int_{-\infty}^{\infty} \int_{-\infty}^{\infty} F(\omega, \theta) e^{2\pi i \omega (x \cos \theta + y \sin \theta)} \omega \mathrm{d}\omega \mathrm{d}\theta \qquad (5.14)$$

and, since $F(\omega, \theta + \pi) = F(-\omega, \theta)$, we can write

$$f(x, y) = \int_{0}^{\pi} \int_{-\infty}^{\infty} F(\omega, \theta) e^{2\pi i \omega (x \cos \theta + y \sin \theta)} |\omega| \mathrm{d}\omega \mathrm{d}\theta \qquad (5.15)$$

Applying the Fourier slice theorem on this, i.e. substituting $F(\omega, \theta)$ by $S_\theta(\omega)$, we get

$$\begin{aligned} f(x, y) &= \int_{0}^{\pi} \int_{-\infty}^{\infty} S_\theta(\omega) e^{2\pi i \omega (x \cos \theta + y \sin \theta)} |\omega| \mathrm{d}\omega \mathrm{d}\theta \\ &= \int_{0}^{\pi} \int_{-\infty}^{\infty} P_\theta(t) h(x \cos \theta + y \sin \theta - t) \mathrm{d}t \mathrm{d}\theta \qquad (5.16) \end{aligned}$$

where the reconstruction filter $h(t)$ has been defined by

$$\begin{aligned} h(t) &\equiv \int_{-\omega_{max}}^{\omega_{max}} |\omega| e^{-2\pi i \omega t} \mathrm{d}\omega \\ &= \frac{1}{\pi} \omega_{max}^2 \frac{\sin t\omega_{max}}{t\omega_{max}} - \frac{1}{2\pi} \omega_{max}^2 \left(\frac{\sin t\omega_{max}}{t\omega_{max}} \right)^2 \qquad (5.17) \end{aligned}$$

with $2\omega_{max}$ being the bandwith of the image. And finally we can write eq. 5.16 in the form of

$$f(x, y) = \int_{0}^{\pi} Q_\theta(t) \mathrm{d}\theta \qquad (5.18)$$

$$Q_\theta(t) = \int_{-\infty}^{\infty} P_\theta(t') h(t - t') \mathrm{d}t' \qquad (5.19)$$

The application of the reconstruction method described here is limited to a parallel beam geometry, as it exists at a synchrotron, for example. Modern laboratory instruments use a fan-beam or cone-beam geometry, which requires more sophisticated reconstruction methods (e.g. [74]).

5.3 X-ray Sources

The spatial resolution in X-ray tomography experiments is mainly governed by the X-ray photon flux. [21] This flux varies over several orders depending on the instrumentation used. The quality of an X-ray source is determined by a number of properties, i.e. source size, divergence, monochromaticity and flux. A single number which allows to compare different X-ray sources is the *brilliance* η. It is defined as [75]

$$\eta(x, y, \theta, \psi, \omega, t) \text{ expressed in } \frac{\text{photons/s}}{\text{mrad}^2 \cdot \text{mm}^2 \cdot (0.1\%\text{BW})} \qquad (5.20)$$

In medical X-ray tomographs (CT) the allowable radiation dose is limited and therefore the spatial resolution is 300-500 μm. Laboratory microtomographs (μCT) that are used for the investigation of non-living samples can use much higher X-ray intensities, mainly limited by the photon flux available from the X-ray tube. On such instruments a resolution of 10 - 20 μm can be achieved. The X-ray photon flux produced by a third generation synchrotron source such as the Swiss Light Source (SLS) at the Paul Scherrer Institute (PSI), Villigen, Switzerland is even orders of magnitude higher than the one available from X-ray tubes. The spatial resolution can thus be improved to about 1 μm with a standard detector or even to the submicrometer range with the use of some newly developed special detectors [75–77].

In the laboratory X-rays are commonly generated in an X-ray tube where electrons that are emitted from a cathode are accelerated in a high voltage field towards a water-cooled metal anode (e.g. copper). The X-rays are emitted in a continuous spectrum of Bremsstrahlung plus additional radiation peaks at characteristic energies.

For tomography experiments usually microfocus X-ray tubes are used. Because of the low brilliance it is anavoidable to use a polychromatic spectrum to get enough intensity for measurements. This can lead to artifacts due to the so-called beam hardening effect. A further disadvantage is that a high photon intensity is only delivered at some discrete energies, thus preventing an optimal tuning of the energy.

Synchrotron radiation is emitted when highly relativistic electrons in a storage ring are accelerated in a magnetic field, which can be achieved by bending magnets, wigglers, or undulators. The resulting radiation has a very high intensity, which is about 10 orders of magnitude higher than that of the Cu Kα line of a rotating copper anode. Furthermore the X-ray beam has a very small divergence and can be considered to be nearly parallel. It is hence possible to use parallel beam reconstruction methods as described in 5.2. Thanks to the very high intensity of the synchrotron X-ray beam it is possible to use a monochromator and still achieving a high photon flux. Because of the X-ray spectrum

being continuous, it is possible to tune the energy to the optimum for the specific measurement. Since achievable photon energies are usually not so high usually only relatively small samples can be investigated with such instruments [75, 78].

5.4 Instrumentation

Microtomography measurements for this thesis were performed on two different instruments. For C/Al-composites measurements were made on a synchrotron based instrument at the Swiss Light Source (SLS) at the Paul Scherrer Institut (PSI), Villigen, Switzerland. The LDPE/Pglass-hybrids were measured on a laboratory instrument at EMPA, Dübendorf, Switzerland. All measurements and raw data processing were done by Peter Wyss of EMPA.

The microtomography instrument at the SLS is located on the Materials science beamline (MS or 4S). This is a multipurpose beamline hosting also a powder diffraction and an in-situ surface diffraction instrument. The microtomography instrument is equipped with a double crystal monochromator with a energy resolution of 0.014%. At 10 keV, a typical energy for microtomography measurements the flux of photons is about 10^{14} photons/s on a spot size of 1 mm^2.

The transmitted photons are converted to visible light by a scintillator and then projected on a CCD camera by a visible light optical setup.

The C/Al samples were measured SLS using a monochromatic beam energy of 10 keV. This corresponds to a wavelength of the X-rays of about 1.2 Å. The field of view (FOV) was 1.4 mm, and 1001 projections over an angle of 180 degrees were measured. The individual 2-D tomograms were reconstructed by a filtered back-projection procedure. The resulting effective size of the digital volume element (voxel) was $0.7 \times 0.7 \times 0.7 ~\mu$m^3 [22].

Polymer/Pglass hybrid samples were measured at EMPA in Dübendorf on a laboratory tomograph. The X-ray source was a micro focus tube Feinfoucus FXE 200.5 with a spot size of about 10μm and an accelaration energy of 90 keV. A Hamamatsu C7942CA-02 detector with a brass filter and a pixel size of 100μm was used and a 2×2 binning of the data was applied. 600 projections with a frame size of 1024×1024 and 8 Bit (256 grey levels) image depth were recorded. The set-up resulted in a effective voxel size of 2.5μm.

The same samples were also measured on microtomograph of the type V-Tomex (Phoenix X-ray, Wunstorf, Germany). With an acceleration energy of 180 keV the spot size was 7μm. A Perkin-Elmer detector without binning was used. 600 projections with a frame size of 500×500 pixels were recorded. The image depth was 16 Bit (65535 grey levels). The resulting voxel size was 5.9μm.
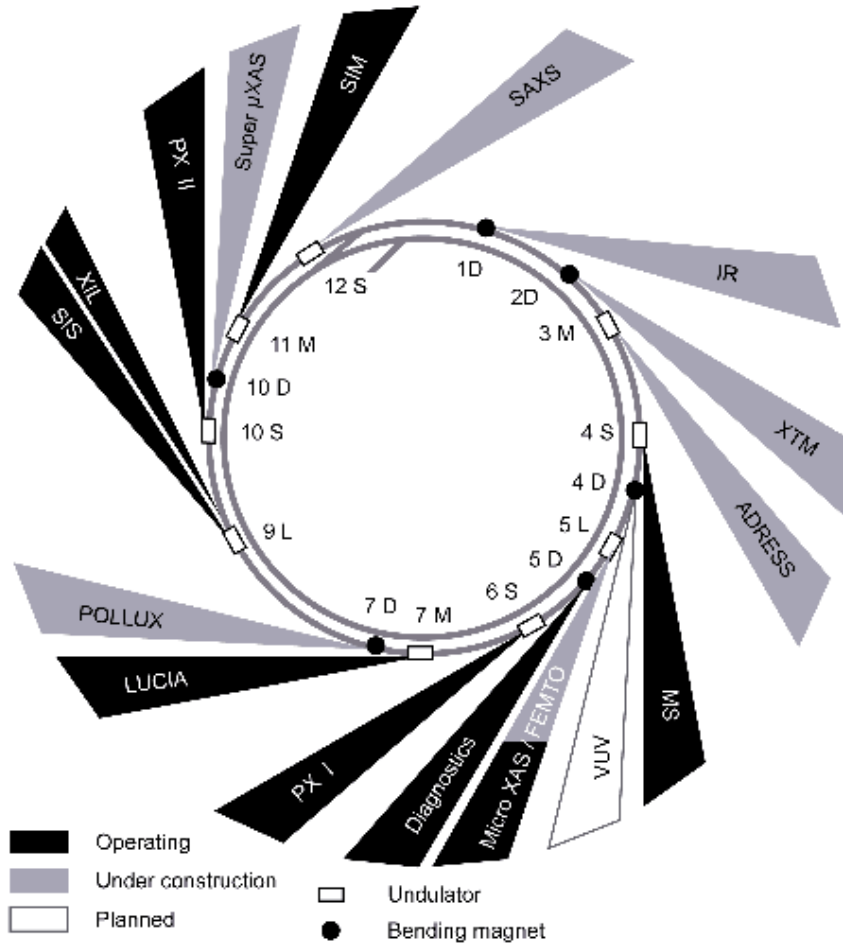
Figure 5.5: Beamlines at the SLS. Tomography measurements were made at beamline MS. From Ref. [79]
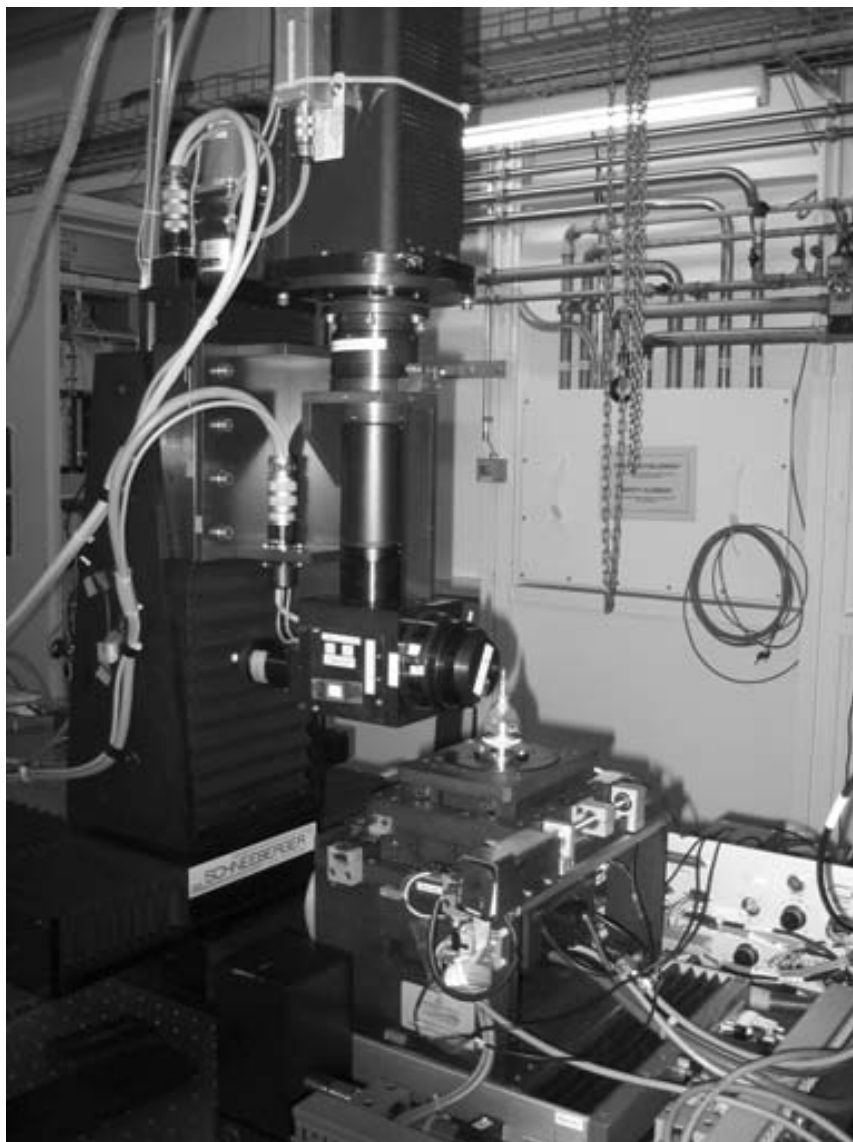
Figure 5.6: The experimental setup at the SLS. The synchrotron beam comes from the right (Photo: Th. Etter).

# 6 Effective Materials Properties Based on Tomography Data

This chapter describes the path that was followed and the procedures that have been applied on the way from the reconstructed tomographic images to effective materials properties.

6.1 Image Segmentation

Image segmentation stands for a transformation of a gray scale image with a (quasi-) continuous spectrum of grey values to an image with distinct regions that belong to one of a usually small number of different phases. In practice, this means that one applies certain threshold values that separate the grey values that are assigned to the same phase.

With the data used here this procedure was not straight-forward, neither for the LDPE/Pglass-hybrids nor for the C/Al-composites. The segmentation of the images was complicated by the fact that there was no clear distinction between the grey values belonging to the different phases (except for pores). This is illustrated by the histogram of the grey values (Fig. 6.1). An automatic segmentation procedure could therefore not be applied.

The human eye, however, shows a remarkable ability to distinguish between
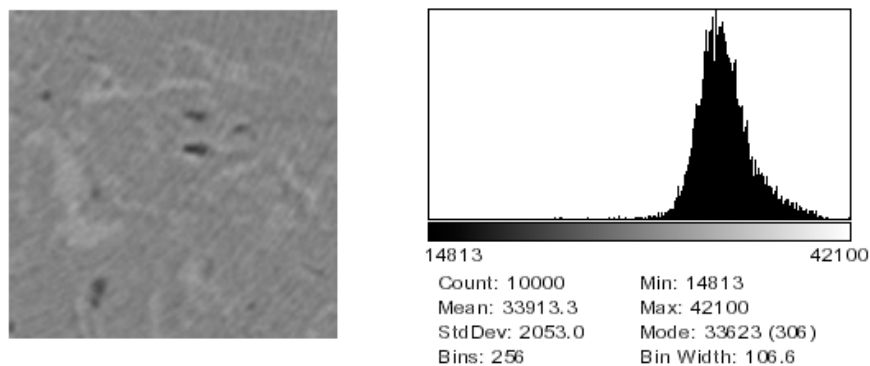
Figure 6.1: Example of a tomogram and corresponding histogram of grey levels.

the different phases. A first estimate for the threshold value that has to be applied for the segmentation was therefore made by visual judgement applying the thresholding option of ImageJ [80].

The phase volume fractions were already known before the image analysis. For the LDPE/Pglass-hybrids the nominal composition from the synthesis of the material was 50 / 50 vol.-%. The open porosity of the graphite preforms was measured by mercury infiltration as 14.5 vol.-%, which means that the sum of aluminium and pore volume fractions has to sum up to this value. The resulting phase volume fractions were checked against these known volume fractions of the phases and the threshold value was varied to match the phase volume fractions in the model to the known values.

6.2 Image Processing

From the complete stack of TIFF images first the region of interest for the specific model was cut out. For example for a 100 x 100 x 100 voxel model the 100 image layers that are of interest were loaded in ImageJ. From these an area of 100 x 100 pixels was cut out. The "*Crop*" function of *ImageJ* allows to process the whole stack of e.g. 100 images simultaneously.

The files were than saved in a 16 bit integer format ("*Save stack as Text image...*""). This means that the image may contain 2^{16} different grey levels which are represented by an integer number between 0 and $2^{16} - 1 = 65536$. The thresholding of these integer images was implemented in a C-program. This program also merged the layers into a single file that served as microstructural input for the FE solver.

For the example of the LDPE/Pglass hybrids the dependance of the phase volume fractions in the model on the threshold value used for the image segmentation is presented here (Fig. 6.2). A volume of $275 \times 200 \times 400$ voxels has been cut out from the complete tomography dataset. This was the largest cuboid volume that could be extracted from the dataset which lies completely inside the sample. 25 slices from the beginning and 25 slices from the end of the stack have been excluded from the analysis because there were artifacts caused by the cone-beam measurement geometry.

From the visual analysis of the images it has been determined that the threshold value should be around 25000. Additionally, the information that the Pglass volume fraction is $f_{Pglass} = 0.50$ was used to exactly specify the segmentation threshold. For a series of different threshold values the images have been segmented and the resulting volume fractions of the two phases calculated. Fig. 6.2 shows the strong dependance of the phase volume fractions (f_{Pglass} and f_{LDPE}) on the threshold value.

6.3 Phase Properties

The FE calculations need the mechanical and / or physical properties of the individual phases as input to determine the effective properties of the composite. The phase properties were either measured or taken from the literature, or in the case where this was not possible they were determined numerically (for details see Ch. 7 and Ch. 8).

6.4 Solver

An in-house solver implementing the method described in chapter 2 was used to calculate the effective properties of the composites. Calculations were performed on a HP Superdome computer maintained by the central computing facilities of ETH (Informatikdienste). In the beginning the Superdome was equipped with PA 8600 processores with a clock rate of 550 MHz. Later it has been upgraded to Itanium-2 processors (clock rate 1.5 GHz). Typical CPU times for calculating the properties of one computer model ranged from a few minutes up to about one week depending on the size of the model, processor speed, and property to be calculated (For physical properties like the electrical conductivity only one
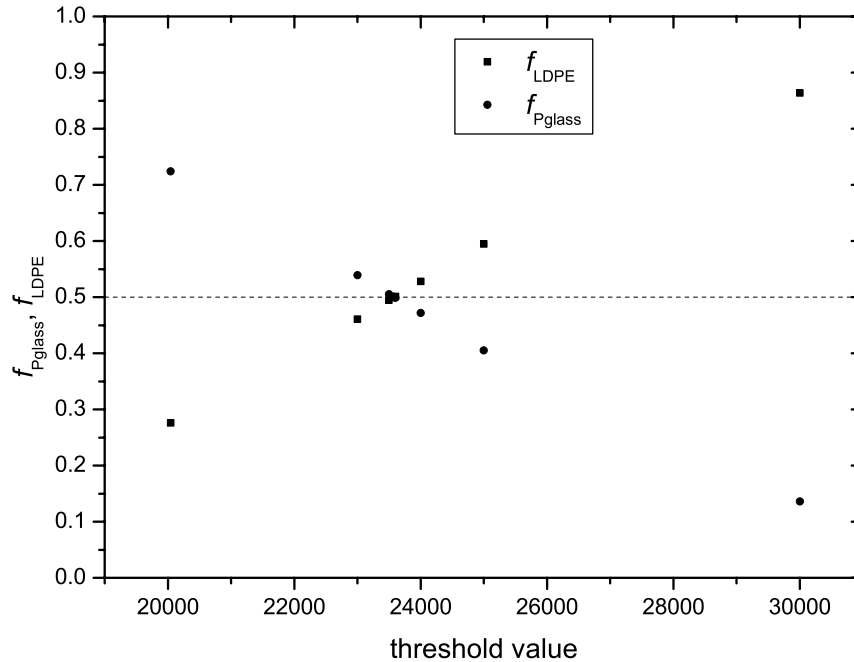
Figure 6.2: Dependance of phase volume fractions (f_{Pglass} and f_{LDPE}) in the model on the threshold value used for image segmentation.

minimization is needed while for the elastic properties six minimizations are needed plus one for the thermal expansion coefficien. Therefore increasing the CPU time approximately by a factor of seven.)

7 LDPE/Pglass-Hybrids

Some specific compositions of phosphate glasses (Pglass) possess the remarkable property of a very low glass transition temperature (T_g) , i.e. not much above 100 ℃. Their glass transition temperature is hence in the same range as the melting point of some polymers e.g. low density polyethylene (LDPE). Nevertheless in the glassy state they show reasonably high stiffness in comparison to most common polymers.

A composite of such a Pglass with a polymer such as LDPE will potentially result in a material showing very interesting elastic properties as compared to most pure polymers.

Due to the T_g of the Pglass being of the same order as the melting temperature (T_m) of LDPE it is possible to melt process composites of the two from a common melt of Pglass and LDPE. This would allow for relatively easy and cost efficient production of large numbers of parts.

Such a process would be economically interesting since well established polymer processing equipment could be used. Examples of possible processing methods are extrusion or injection moulding.

This numerical study was done to first investigate the continuity of the two phases (Sec. 7.2.3). Subsequently the mechanical properties of the hybrid were predicted by finite elements (Sec. 7.3). This results were largely different from experimental data. Therefore local stresses in the hybrid were analyzed in order to understand the observed discrepancy (Sec. 7.4).

7.1 Material Processing

LDPE/Pglass hybrids have been synthesized by Kevin Urman and Prof. Joshua Otaigbe at the University of Southern Mississippi, USA. They have provided the samples for mechanical and tomography measurements. For this reason the synthesis of these hybrids is presented here only shortly.

The Pglass was prepared from stochiometrically calculated amounts of ammonium dihydrogen phosphate ($NH_4H_2PO_4$), tin oxide (SnO), and tin fluoride (SnF_2) to produce a molar composition of $0.50\,SnF_2 + 0.20\,SnO + 0.30\,P_2O_5$ [81,82]. The resulting glass has a density of $\rho = 3.75\,g/cm^3$ and a remarkably low glass transition temperature of $T_g = 116 - 126\,℃$.

As polymer component a molding grade low density polyethylene (LDPE) of Huntsman Corp. (PE 1023) with a density of $\rho = 0.92\,\text{g/cm}^3$ and a melting point of $T_m = 125\,°C$ was used. The two components, Pglass and LDPE, were melt blended in a Brabender torque mixer with twin roller-type rotors. The mixer was preheated to 140 °Cand a fixed shear rate of 30 rpm was set. The polymer was first added and kept in the mixer for about 5 minutes until a homogeneous melt was achieved. Then the glass was added and the mixture was melt mixed for about 20 minutes. For this project a hybrid with a glass content of 50 vol.-%, corresponding to 80 w.-%, was prepared [83, 84].

Samples for the dynamic mechanical tests were compression moulded and DMTA samples were cut from the compression molded sheets. For tomography measurements strands of the hybrid were extruded.

7.2 Morphology of Hybrids

7.2.1 SEM Results

Otaigbe et al. published a scanning electron microscopy image of a cross section through a 50/50vol.-% LDPE/Pglass hybrid that shows an interesting microstructure (Fig. 7.1). They suggest that the presented microstructure is formed by a co-continuous network of LDPE and Pglass [83].

Since interpenetrating networks (IPN) may have unconventional properties a novel material which potentially has such a microstructure is interesting to investigate. However, it is difficult, if not impossible, to decide whether a given microstructure is really co-continuous solely based on SEM images because this information is generically 2-D. It is very cumbersome and not really reliable to conclude from 2-D images to the three-dimensional microstructure of a material. The LDPE/Pglass hybrids were therefore studied with the help of X-ray microtomography.

New samples have been prepared for this purpose by Urman. A SEM micrograph of one of these samples (Fig. 7.2) is not of such a good image quality which makes a comparison with the aforementioned image (Fig. 7.1) difficult. However, one could get the impression that here we see globular inclusions in a matrix, which would contradict the existence of a co-continuous microstructure.

7.2.2 X-ray Tomography

As can be seen from the SEM images, the microstructural features in the 50/50 LDPE/Pglass hybrids have a minimal size of about $10\,\mu\text{m}$ or larger. It is therefore sufficient to use a laboratory microtomograph in order to resolve the microstructure of this material. This has the advantage that access to such a

system is much easier than to a synchrotron-based instrument.

Because of the high tin content of the Pglass a reasonable contrast between the polymer and the Pglass phase could be expected.

Microtomography measurements on the hybrids were made by Peter Wyss of the Centre for Non-Destructive Testing of EMPA in Dübendorf, Switzerland. Fig. 7.3 presents a typical tomogram slice from on of the measured sample. A magnified region (100×100 pixels) of this slice is shown in Fig. 7.4.

Reconstructed tomograms were processed as described in Ch. 6 From the stack of reconstructed slices a three-dimensional representation of the microstructure was created (Fig. 7.5). It represents a reconstructed volume of $400 \times 275 \times 200$ voxels, where one voxel is $5 \times 5 \times 5 \, \mu\mathrm{m}^3$.

7.2.3 Continuity of the Phases

Obviously, it is impossible to determine whether the individual phases are continuous from a 3-D representation such as Fig. 7.5. Because the volume fraction of both phases is 50% each, the network constituting either one phase is rather dense. We can, however, use our numerical tools to decide whether either phase is continuous or not. With the finite element method described in Ch. 2 we determine separately for the two phases whether whether they are continuous,
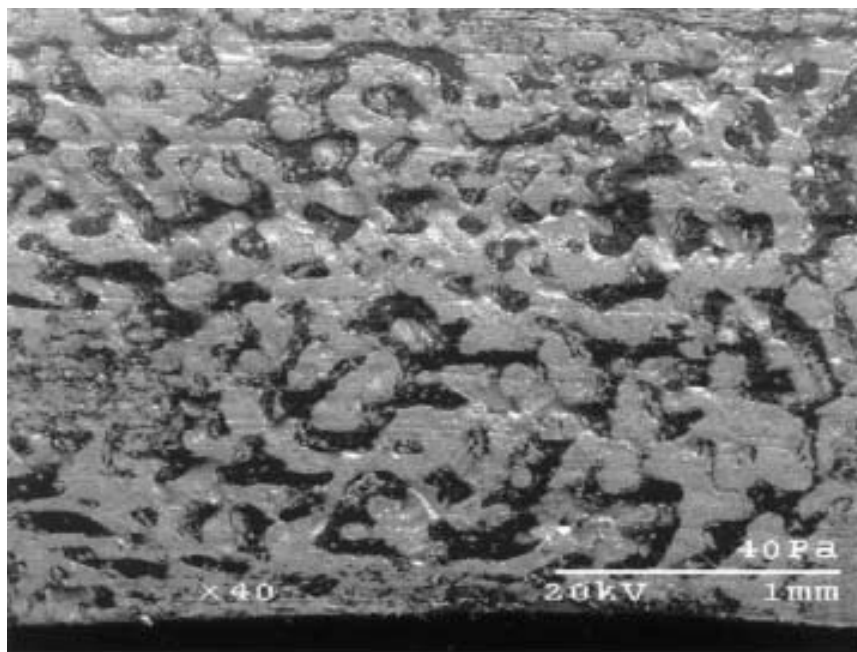
Figure 7.1: SEM micrograph of 50/50 vol.% LDPE/Pglass hybrid. Indicating a possibly co-continuous microstructure. From Ref. [83]
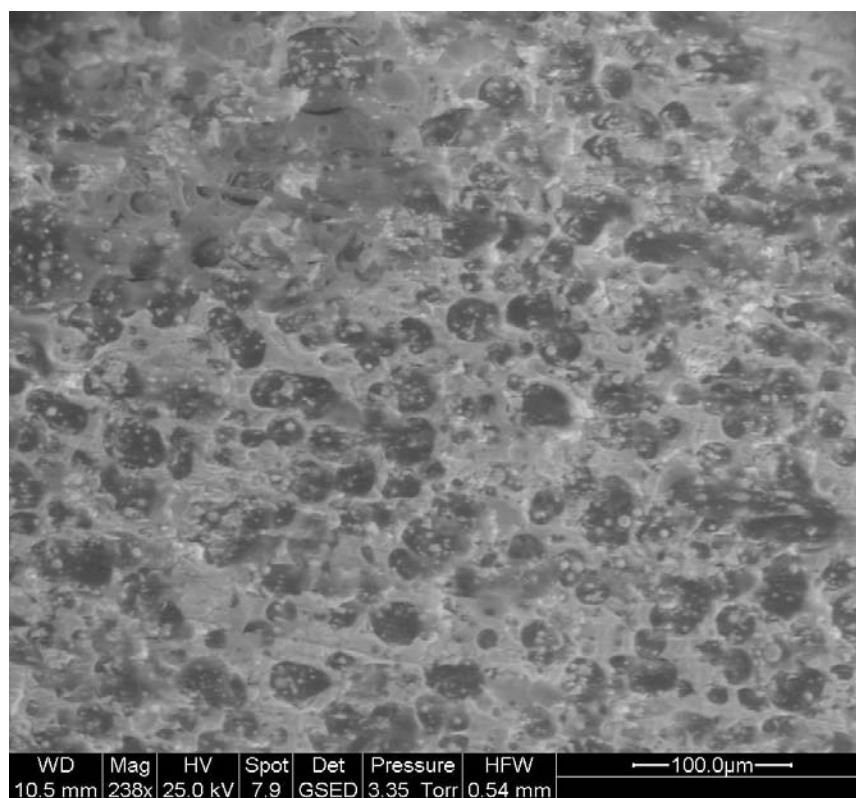
Figure 7.2: SEM micrograph of 50/50 vol.% LDPE/Pglass hybrid. New sample prepared for microtomography measurements (SEM image by Kevin Urman, USM).
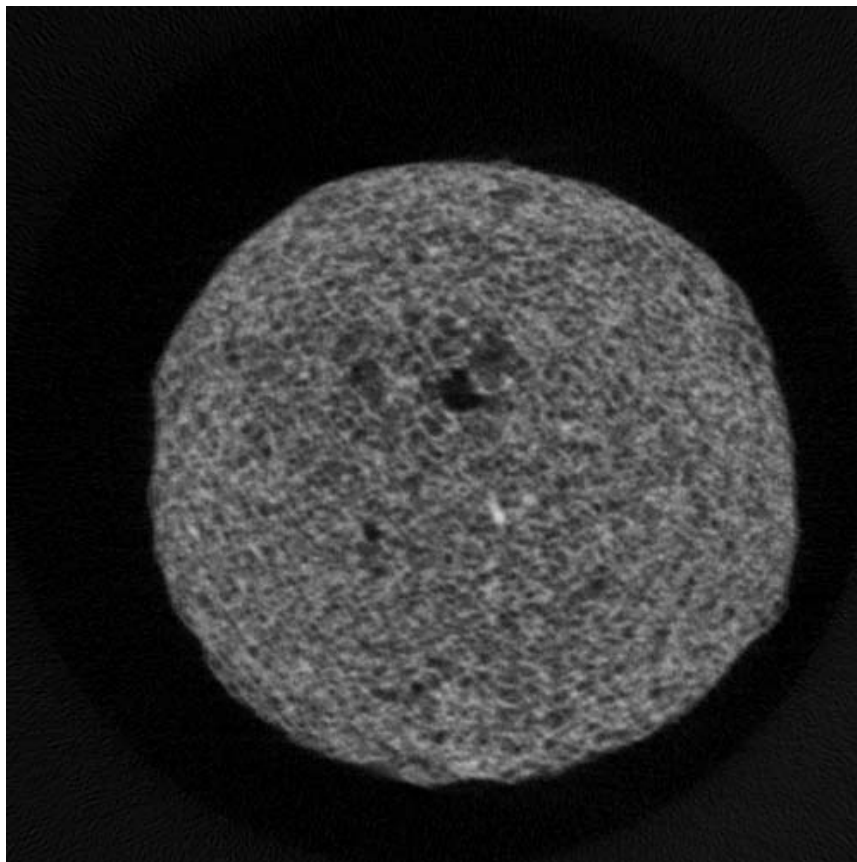
Figure 7.3: Representative tomogram of 50/50 vol.% LDPE/Pglass hybrid sample. Image size is 500×500 pixels.
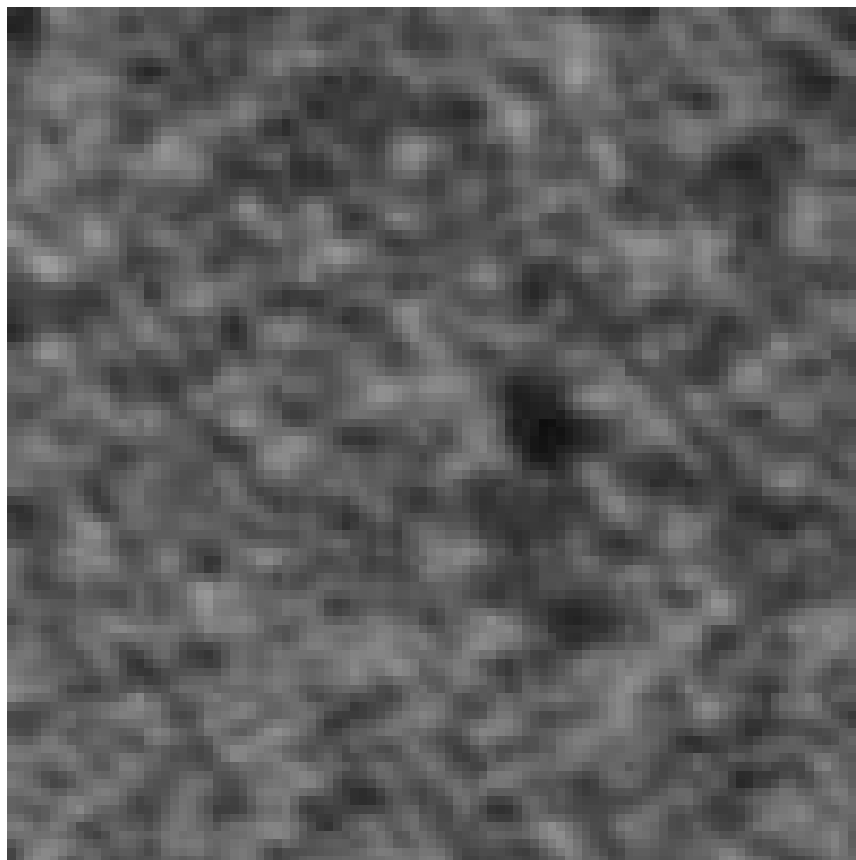
Figure 7.4: Magnified region of Fig. 7.3 (50/50 vol.% LDPE/Pglass hybrid sample). Image size is 100×100 pixels.
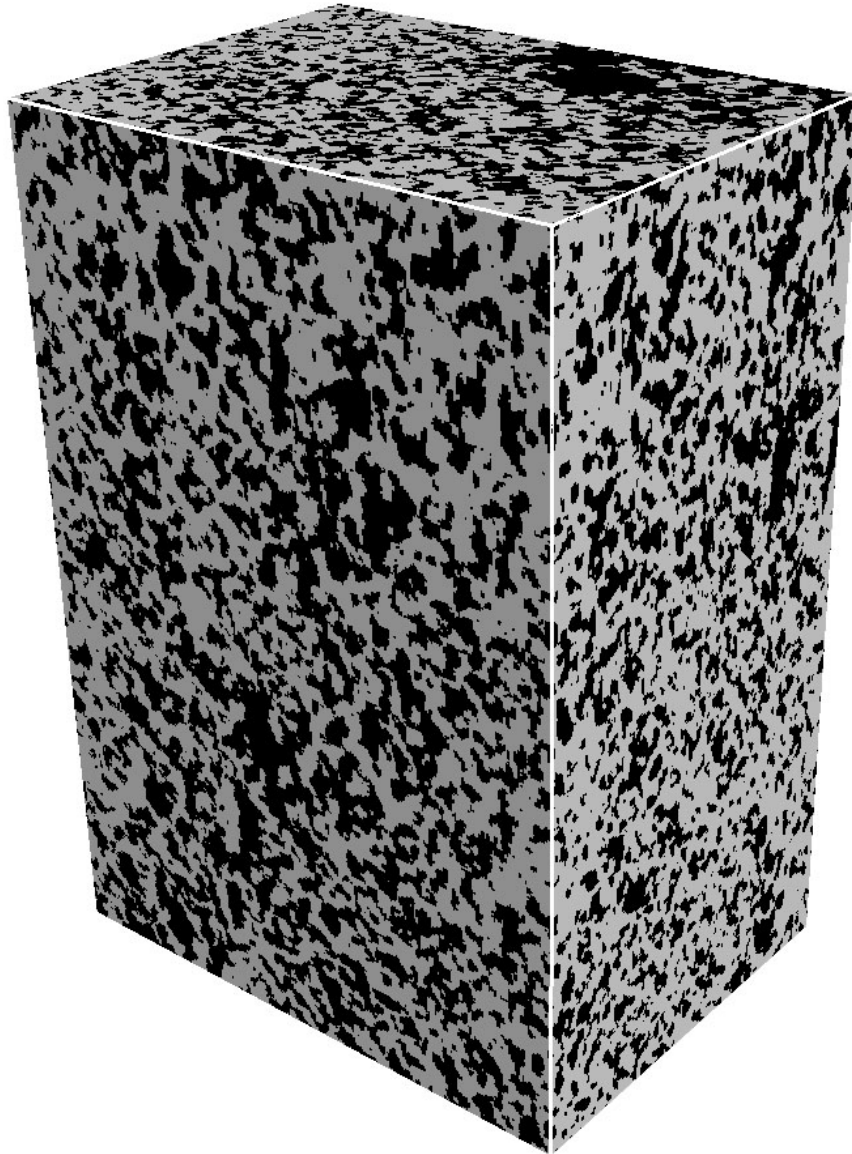
Figure 7.5: Three-dimensional representation of the microstructure as measured by X-ray microtomography. The volume is 400 x 275 x 200 voxels, where one voxel is 5 x 5 x 5 μm^3.

Table 7.1: Dependance of the effective conductivity of the hybrid (σ_{eff}^{LDPE} and σ_{eff}^{Pglass}) on the conductivity of the conducting phase σ. σ_{eff} values are normalized by σ in order to facilitate comparison.

| σ	1	10	100
$\sigma_{eff}^{LDPE}/\sigma$	0.3198	0.3182	0.3134
$\sigma_{eff}^{Pglass}/\sigma$	0.2195	0.2184	0.2149

or not.

The conductivity is a property that is sensitive to the continuity of a phase. Providing that phase B is non-conducting, phase A can only conduct an electric current through the sample if there are continuous conducting paths of phase A that connect the opposite sides of the sample.

In this study we test the continuity of the two phases by two separate calculations: in the first one the LDPE phase is assigned an arbitrary conductivity of unity ($\sigma_{LDPE} = 1$) while the Pglass is assigned zero conductivity ($\sigma_{Pglass} = 0$). Therefore the effective conductivity of the hybrid depends only on the LDPE and an non zero conductivity can only be realized in the case where the LDPE phase is continuous. In a subsequent calculation the Pglass is taken to be the conducting phase ($\sigma_{Pglass} = 1$, $\sigma_{LDPE} = 0$). With these parameters the continuity of the Pglass phase is tested.

Numerical Results

It was tested whether the arbitrary choice of a conductivity value for the conducting phase would influence the result in an unacceptable way. To this end the effective conductivity was predicted with different values for the conductivity of the conducting phase for a test volume of 100 x 100 x 100 voxels. As the results in Table 7.1 show the differences in the result are negligible when determining phase continuity.

The procedure described above is performed on 16 arbitrarily chosen subvolumes of a size of $100 \times 100 \times 100$ voxels. It can be expected that the effective conductivity depends on the volume fraction of the conducting phase in the specific subvolume. The phase contents in the 16 individual subvolumes are presented in Fig. 7.6. The average volume content of LDPE in the 16 subvolumes is $f_{LDPE} = 0.507 \pm 0.071$ and all 16 individual values lie within an interval of two standard deviations. The numerically predicted conductivity values are $\sigma_{eff}^{LDPE} = 0.277 \pm 0.080$ (LDPE conducting phase), and $\sigma_{eff}^{Pglass} = 0.283 \pm 0.076$ (Pglass conducting phase), respectively (Fig. 7.7, Fig. 7.8).

It can be seen from these results that either of the two phases shows continuous conductivity for itself. From this we conclude that both phases are
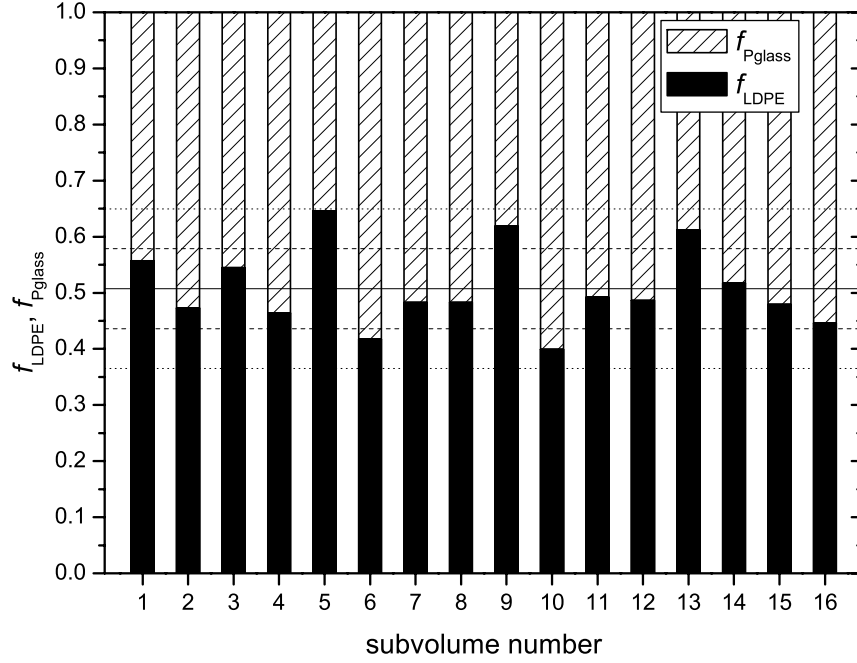
Figure 7.6: Volume contents of the two phases (f_{Pglass} and f_{LDPE}) in the 16 sub-volumes of $100 \times 100 \times 100$ voxels. The solid line represents the average LDPE volume content $f_{LDPE} = 0.507$, while the dashed and dotted lines show a deviation of one and two standard deviations.
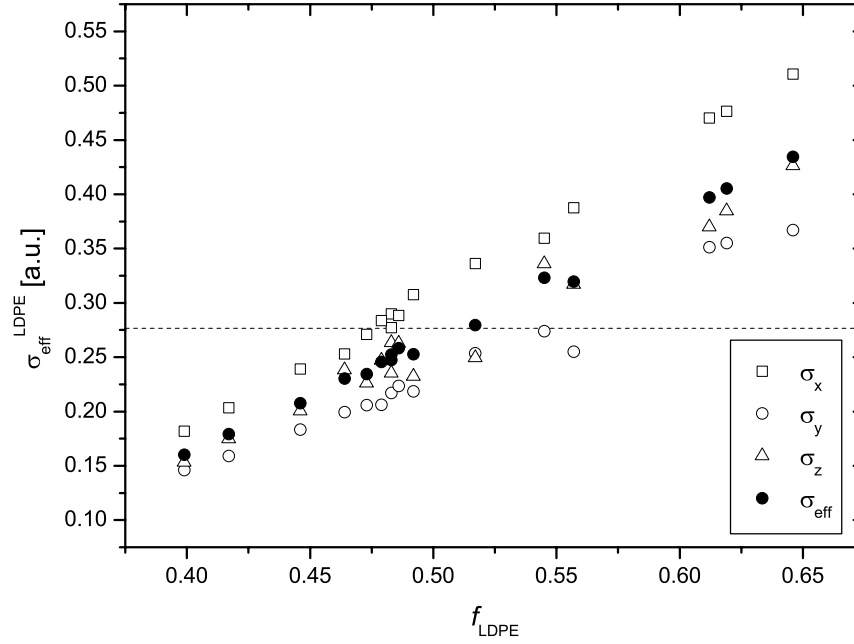
Figure 7.7: Numerically predictions for the effective conductivity of subvolumes of $100 \times 100 \times 100$ voxels with LDPE as conducting phase. σ_x, σ_y, and σ_z are the predicted conductivity values in the respective directions, wheras σ_{eff} is the average of σ_x, σ_y, and σ_z. Conductivity values are plotted in dependance of the volume fraction of the LDPE phase.
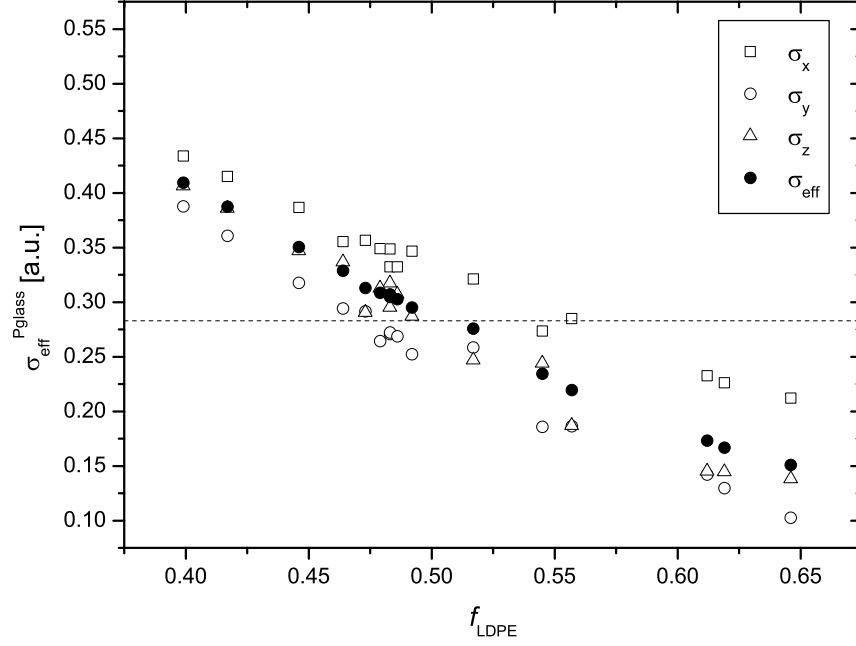
Figure 7.8: Numerically predictions for the effective conductivity of subvolumes of $100 \times 100 \times 100$ voxels with Pglass as conducting phase. σ_x, σ_y, and σ_z are the predicted conductivity values in the respective directions, wheras σ_{eff} is the average of σ_x, σ_y, and σ_z. Conductivity values are plotted in dependance of the volume fraction of the LDPE phase.

continuous, and thus a co-continuous microstructure is present as it was suggested by Otaigbe [83].

7.3 Mechanical Properties

Whereas the electrical conductivity calculations have been made in order to determine the continuity of the phases, the mechanical properties of LDPE/Pglass hybrids are of real interest in practice. It is *a priori* unclear what mechanical properties will result from the co-continuous microstructure of the hybrids. When manipulating the samples it is noticed that they are very brittle.

7.3.1 DMTA Measurements

To get a quantitative picture oft the elastic properties of the hybrids their modulus has been measured by dynamic mechanical thermal analysis (DMTA). This method seemed to be most appropriate because of the brittleness of the material and the small sample sizes available.

A Polymer Laboratories Mk II Dynamic Mechanical Thermal Analyser (DMTA) was used. The measurements were made in the single cantilever bending mode, i.e. one end of the sample was fixed and the dynamic load was applied to the other end of the sample. Temperature scans from 25°C to 100°C at a heating rate of 1°C/min were made at frequencies of 1 Hz, and 10 Hz, respectively.

LDPE/Pglass hybrid material was compression moulded to a thickness of 1 mm and cut into 7 mm wide samples. The free sample length in the measurement setup was 8 mm. As a control, LDPE samples were also measured in the same setup. They were compression molded to plates of a thickness of 0.9 mm and cut into samples 10 mm wide.

For LDPE a storage modulus $E' = 0.3$ - 0.4 GPa at room temperature was measured (Fig. 7.9). This is in reasonable accordence with values of 0.1 - 0.3 GPa given in the the literature for the tensile modulus of LDPE [85]. For the LDPE/Pglass hybrid samples E' was in the range of 1.1 - 1.3 GPa at room temperature (Fig. 7.10). The phase shift at room temperature is small ($\tan \delta \approx 0.2$) therefore the complex modulus E^* is in this case comparable to the storage modulus (since $E^* = E'\sqrt{1 + (\tan \delta)^2}$).

Stiffnesses between 1 GPa and 2 GPa can easily be achieved with common commercial polymers, e.g. HDPE has a stiffness of 0.4 - 1.4 GPa, PP has 1.1 - 2.1 GPa, or PA66 has 1.2 - 3.8 GPa [85]. With such polymers this stiffness level can be achieved at a density of about 1 g/cm^3 whereas the LDPE/Pglass hybrids have a density of more than 2 g/cm^3. Technologically the measured stiffness of the hybrid is not very appealing since they can be easily achieved
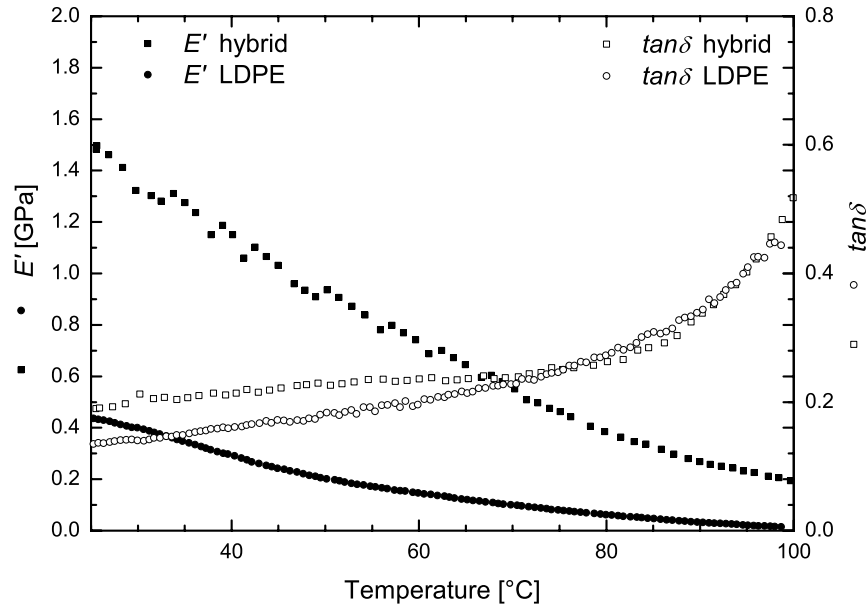
Figure 7.9: Result of DMTA measurements. Comparsison between pure LDPE and LDPE/Pglass hybrid at a frequency of 10 Hz. Storage modulus E' and loss factor $\tan\delta$ are shown.
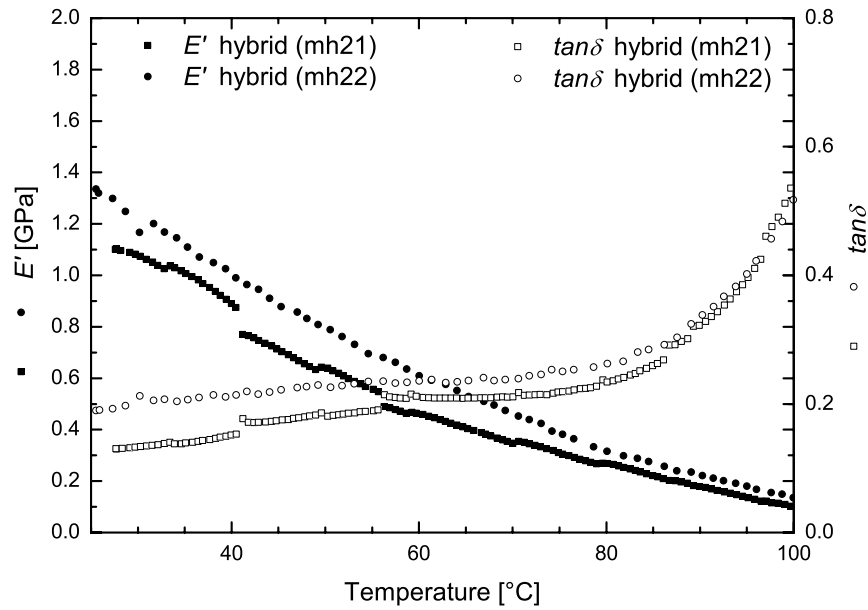
Figure 7.10: Result of DMTA measurements. Two LDPE/Pglass hybrid samples (mh021 and mh022) at a frequency of 1 Hz. Storage modulus E' and loss factor $\tan\delta$ are shown.

with common polymers. Considering specific stiffness the hybrids are in an even less favorable position because at a density of more 2 g/cm^3 they have the same stiffness as what is achievable with pure polymers at 1 g/cm^3. The brittleness of the hybrids is a further drawback which should be taken into account.

These results show that at the present stage the stiffness of the hybrids is technologically not very appealing. Nevertheless, the LDPE/Pglass hybrids are interesting from a scientific point of view and have therefore been studied further. Namely, it was interesting to determine the technological potential of the interpenetrating microstructures and to identify the reason why it is not realized in practice.

7.3.2 Micromechanical Models

Micromechanical models allow to make straight-forward predictions of the effective properties of a composite material. Their advantage is that they use analytical expression, which makes the evaluation relatively easy and fast. But on the other hand predictions are only bounds or estimates for very simple geometries such as fully aligned fibres.

Nevertheless some results are presented here in order to see the range in which the numerically predicted properties are expected. Reuss and Voigt bounds are not very restrictive but very simple to calculate since they are based on the assumption of equal stress or equal strain, respectively, in the two phases of the composite. The upper (Voigt) bound is given as

$$E_{Voigt} = \sum f_i E_i \qquad (7.1)$$

where f_i is the volume fraction of phase i, and E_i is Young's modulus of phase i. In this specific case with the phase properties given in Table 7.2 the Voigt bound is $E_{Voigt} = 15.1$ GPa. Meanwhile the lower (Reuss) bound is defined as

$$E_{Reuss} = \frac{1}{\sum f_i/E_i} \qquad (7.2)$$

and in our case is $E_{Reuss} = 0.4$ GPa. In the present situation the Reuss bound is very close to the stiffness of the LDPE and the interval between Voigt and Reuss bounds is very wide because of the large difference in the stiffnesses of the two phases.

The Hashin-Shtrikman bounds on the effective elastic moduli make more rigorous predictions. They are based on a variational principle and it can be shown that they are the most rigorous bounds that can be specified when only the volume fractions of the phases are known and no further information about the microstructure of the composite is available [43, 86, 87].

For the bulk modulus k and the shear modulus μ of a two phase composite with phase properties k_1, k_2, μ_1, and μ_2 the lower and upper Hashin-Shtrikman bounds on the effective moduli are

$$\frac{f_1}{1 + (1 - f_1)\frac{k_1 - k_2}{k_2 + k_l}} \leq \frac{k - k_2}{k_1 - k_2} \leq \frac{f_1}{1 + (1 - f_1)\frac{k_1 - k_2}{k_2 + k_u}} \tag{7.3}$$

and

$$\frac{f_1}{1 + (1 - f_1)\frac{\mu_1 - \mu_2}{\mu_2 + \mu_l}} \leq \frac{\mu - \mu_2}{\mu_1 - \mu_2} \leq \frac{f_1}{1 + (1 - f_1)\frac{\mu_1 - \mu_2}{\mu_2 + \mu_u}} \tag{7.4}$$

where for $(\mu_1 - \mu_2)(k_1 - k_2) \geq 0$

$$k_l = \frac{4}{3}\mu_2 \tag{7.5}$$

$$k_u = \frac{4}{3}\mu_1 \tag{7.6}$$

$$\mu_l = \frac{3}{2}\left(\frac{1}{\mu_2} + \frac{10}{9k_2 + 8\mu_2}\right)^{-1} \tag{7.7}$$

$$\mu_u = \frac{3}{2}\left(\frac{1}{\mu_1} + \frac{10}{9k_1 + 8\mu_1}\right)^{-1} \tag{7.8}$$

and for $(\mu_1 - \mu_2)(k_1 - k_2) \leq 0$

$$k_l = \frac{4}{3}\mu_1 \tag{7.9}$$

$$k_u = \frac{4}{3}\mu_2 \tag{7.10}$$

$$\mu_l = \frac{3}{2}\left(\frac{1}{\mu_2} + \frac{10}{9k_1 + 8\mu_2}\right)^{-1} \tag{7.11}$$

$$\mu_u = \frac{3}{2}\left(\frac{1}{\mu_1} + \frac{10}{9k_2 + 8\mu_1}\right)^{-1} \tag{7.12}$$

From these results the effective tensile modulus E and the effective Poisson's ratio is available through the relations

$$E = \frac{9k\mu}{3k + \mu} \tag{7.13}$$

and

$$\nu = \frac{3k - 2\mu}{6k + 2\mu} \tag{7.14}$$

For the specific case with the phase properties of Table 7.2 the Hashin-Shtrikman bounds on the effective Young's modulus are $E_{lower} = 0.676\,\text{GPa}$,

and $E_{upper} = 10.845\,\text{GPa}$. The usefulness of these bounds is limited in cases like this where the ratio between the moduli of the two phases is quite large. Because here the bounds lie far apart.

The micromechanical model developed by Tandon and Weng [46] based on Eshelby's solution for an ellipsoidal inclusion in an infinite matrix [44] and on Mori-Tanaka's average stress [45] is a widely used model. It predicts the five independent elastic constants of a transversely isotropic composite with fully aligned "fibres" with an aspect ratio between zero and infinity (i.e. platelets, spheres, and fibres of various aspect ratio are covered by this) by the following analytical expressions:

$$\frac{E_{11}}{E_m} = \left(1 + f_f\frac{A_1 + 2\nu_m A_2}{A_6}\right)^{-1} \tag{7.15}$$

$$\frac{E_{22}}{E_m} = \left(1 + f_f\frac{-2\nu_m A_3 + (1-\nu_m)A_4 + (1+\nu_m)A_5 A_6}{2A_6}\right)^{-1} \tag{7.16}$$

$$\frac{G_{12}}{G_m} = 1 + f_f\left(\frac{\mu_m}{\mu_f - \mu_m} + 2f_m S_{1212}\right)^{-1} \tag{7.17}$$

$$\frac{G_{23}}{G_m} = 1 + f_f\left(\frac{\mu_m}{\mu_f - \mu_m} + 2f_m S_{2323}\right)^{-1} \tag{7.18}$$

$$\nu_{21} = \frac{\nu_m A_6 - f_f(A_3 - \nu_m A_4)}{A_6 + f_f(A_1 + 2\nu_m A_2)} \tag{7.19}$$

$$\frac{K_{23}}{K_m} = \frac{(1+\nu_m)(1-2\nu_m)}{1 - \nu_m(1+2\nu_{21}) + f_f\frac{2(\nu_{21}-\nu_m)A_3 + (1-\nu_m(1+2\nu_{21}))A_4}{A_6}} \tag{7.20}$$

where λ_m, μ_m, λ_f, and μ_f are the Lamé constants of the matrix and the fibres, respectively. f_f is the volume fraction of the inclusion phase (fibres) and $f_m = 1 - f_f$ is the volume fraction of the matrix. Eq. 7.19 was derived by Tucker [32] and is not the original equation derived by Tandon and Weng. The original equation can only be solved iteratively because it is coupled with eq. 7.20. The parameters $A_1, \ldots, A_6$, $B_1, \ldots, B_5$, and $D_1, \ldots, D_3$ are defined as follows:

$$A_1 = D_1(B_4 + B_5) - 2B_2 \tag{7.21}$$

$$A_2 = (1 + D_1)B_2 - (B_4 + B_5) \tag{7.22}$$

$$A_3 = B_1 - D_1 B_3 \tag{7.23}$$

$$A_4 = (1 + D_1)B_1 - 2B_3 \tag{7.24}$$

$$A_5 = \frac{1 - D_1}{B_4 - B_5} \tag{7.25}$$

$$A_6 = 2B_2 B_3 - B_1(B_4 + B_5) \tag{7.26}$$

Table 7.2: Properties of the LDPE and the Pglass used for the calculations. Young's modulus E, Poisson ratio ν, linear thermal expansion coefficient α, and density ρ. Average values taken from the literature.

	LDPE	Pglass
E [GPa]	0.2	30.0
ν	0.49	0.27
α [10^{-6}/K]	150.0	12.0
ρ [g/cm^3]	0.92	3.64

$$B_1 = f_f D_1 + D_2 + f_m(D_1 S_{1111} + 2S_{2211}) \tag{7.27}$$

$$B_2 = f_f + D_3 + f_m(D_1 S_{1122} + S_{2222} + S_{2233}) \tag{7.28}$$

$$B_3 = f_f + D_3 + f_m(S_{1111} + (1 + D_1)S_{2211}) \tag{7.29}$$

$$B_4 = f_f D_1 + D_2 + f_m(S_{1122} + D_1 S_{2222} + S_{2233}) \tag{7.30}$$

$$B_5 = f_f + D_3 + f_m(S_{1122} + S_{2222} + D_1 S_{2233}) \tag{7.31}$$

$$D_1 = 1 + 2\frac{\mu_f - \mu_m}{\lambda_f - \lambda_m} \tag{7.32}$$

$$D_2 = \frac{\lambda_m + 2\mu_m}{\lambda_f - \lambda_m} \tag{7.33}$$

$$D_3 = \frac{\lambda_m}{\lambda_f - \lambda_m} \tag{7.34}$$

S_{ijkl} are the components of Eshelby's tensor which depend on the Poisson's ratio of the matrix ν_m and the inclusion aspect ratio a. Expressions for the components of the Eshelby tensor can be found in the paper of Tandon and Weng. [46]

The model of Tandon and Weng predicts $E = 3.4\,\text{GPa}$ for our composition. However, it should be noted that this is not really a comparable situation since it is a prediction for parallel fibres whereas here in the investigated material the reinforcing phase forms a three-dimensional network.

7.3.3 Numerical Results

The finite element method of Ch. 2 was used to numerically predict the effective elastic constants of the hybrids. Numerical estimates were calculated for two

Table 7.3: Numerically predicted stiffness values of two hybrid samples ($200 \times 200 \times 275$ voxels). All values in GPa.

Sample ID	E_{11}	E_{22}	E_{33}	E_{eff}
hyb275_01	8.193034	6.471022	6.863883	7.175980
hyb275_02	8.512704	6.711815	6.901985	7.375501

Table 7.4: Numerically predicted thermal expansion coefficients of two hybrid samples ($200 \times 200 \times 275$ voxels). All values in $10^{-5} \cdot \mathrm{K}^{-1}$.

Sample ID	α_{11}	α_{22}	α_{33}	α_{eff}
hyb275_01	4.392	6.824	6.108	5.775
hyb275_02	4.201	6.629	6.272	5.701

different volumes with a size of $200 \times 200 \times 275$ voxels each. Again phase properties as given in Table 7.2 were used. The energy minimization was stopped when the gradient had reached $3 \cdot 10^{-3}$ of its initial value. The effective Young's modulus for deformation in x-, y-, and z-direction, respectively, were extracted from the effective stiffness tensor and the average value of the three was calculated Table 7.3. The effective thermal expansion coefficient for a temperature change of $\Delta T = +1\mathrm{K}$ was also calculated. Results are shown in Table 7.4.

The stiffness in the 11-direction is 20-30% higher than in the two perpendicular 22- and 33-directions. The 11-direction is the extrusion direction of the sample. The higher stiffness in this direction is caused by some degree of preferential orientation of the high stiffness Pglass phase in this direction induced by the extrusion process. The lower thermal expansion coefficient in 11-direction directly follows from the higher stiffness in this direction.

7.3.4 Difference to Measured Stiffness

An overview of measured, calculated, and numerically predicted stiffness values is given in Table 7.5. The numerically predicted stiffness seems to be reasonable in comparison with upper bound values (Sec. 7.3.2). It is about 33 % smaller than the upper Hashin-Shrtrikman bound. But this is still a value which can be explained by the particularities of the microstructure.

The measured stiffness (1.2 GPa), however, is less than 20 % of the numerically predicted stiffness (7.3 GPa). This very striking difference is far beyond the experimental error or the error of the numerical method. We therefore were looking for a different reason for this obvious discrepancy.

Table 7.5: Overview on measured, calculated, numerically predicted Young's modulus of a 50/50 LDPE/Pglass hybrid sample. Measured and numerically predicted results are given as average over two samples.

method	E_{eff} [GPa]
measured	1.2
Voigt upper bound	15.1
Hashin-Shrtrikman upper bound	10.8
Tandon-Weng	3.4
numerical prediction	7.3

7.4 Local Thermal Stresses

In order to explain the large difference between the numerical prediction and the measured stiffness of the hybrid we propose the following explanation: the thermal expansion coefficient of the two phases differ by more than one order of magnitude ($150 \cdot 10^{-6}$ K^{-1} vs. $12 \cdot 10^{-6}$ K^{-1}). During the cooling from the manufacturing temperature to room temperature this mismatch will inevitably lead two internal stresses in the two phases. We assume that the relevant temperature interval for the build-up of thermal stresses starts at the glass transition temperature of the Pglass, which is around 120℃ (approximately the melting temperature of LDPE, too), and continues down to room temperature. Therefore the relevant temperature interval it is about 100 K. By analyzing the local thermal stresses obtained from the finite element calculation it can be decided whether they are large enough to cause local damage in the structure. In particular, it is interesting whether the higher stiffness Pglass phase will be damaged because this may lead to the observed low stiffness.

7.4.1 Method

During the calculation of the effective thermal expansion coefficients a virtual temperature change of $\Delta T = +1$ K is applied to the model. At the end of the minimization process the local hydrostatic pressure and the local von Mises stress caused by the temperature change in each individual element is calculated and written to the output file. When the samples are manufactured and subsequently cooled to room temperature, which is about 100 K below the glass transition temperature of Pglass. Therefore it has been assumed that the temperature difference, which causes thermal stresses, is $\Delta T = -100$ K. The elastic constants and the thermal expansion coefficient are assumed to be constant over this temperature interval. Therefore the stress values predicted for a

$\Delta T = +1\,\mathrm{K}$ were multiplied by a factor of $A = -100$ to calculate the stresses for a $\Delta T = -100\,\mathrm{K}$.

The local stresses are calculated for two different volumes of 11 million elements each ($275 \times 200 \times 200$ voxels). The local stresses have been evaluated separately for the LDPE and for the Pglass respectively.

7.4.2 Numerical Results

Histograms show the distribution of local von Mises stress and local hydrostatic pressure occuring in the elements of one phase after the cooling process. It should be noted that the ordinate of the histograms is plotted in logarithmic scale because the distribution is dominated by the average stress and pressure values. The number of elements that are subject to such average pressure of stress are of the order of 10^6 out of about $5.5 \cdot 10^6$ elements. However, there remain a significant number of elements (on the order of 10^1 to 10^2) that are subject to much higher loads.

Considering the LDPE first (Fig. 7.11 and Fig. 7.12), we observe that the majority of elements are under a von Mises stress of less than 4 MPa and only very few undergo a von Mises stress of up to 8.5 MPa. Looking at the hydrostatic pressure it is clear that the majority of the elements are under a negative hydrostatic pressure which effectively is a tension. All tension is smaller than 30 MPa. A minority of elements is under compression up to about 30 MPa. But since compression is much less prone to cause failure of the material, this can be neglected. Assuming that the amorphous domains of the LDPE are still able to deform plastically to some degree damage is not expected to occur in the LDPE phase.

Because of the relatively higher stiffness of the Pglass, which is 150 times larger than the one of LDPE, stresses in this phase are much higher (Fig. 7.13 and Fig. 7.14). Von Mises stresses in the vast majority of elements are below 100 MPa but stresses of up to 230 MPa are found in significant numbers of elements. The hydrostatic pressure is mainly positive meaning that most of the elements are under compression and thus not susceptible to failure. But considerable numbers of elements are still under tension of up to 20 MPa, which is about 0.1% of the Young's moudulus of Pglass.

7.5 Interpretation and Conclusion

Using the electrical conductivity as a test it was found that both the LDPE phase and the Pglass phase are continuous at a 50/50 vol.-% composition of the hybrid. This means the microstructure is co-continuous.

LDPE - hyb275_01
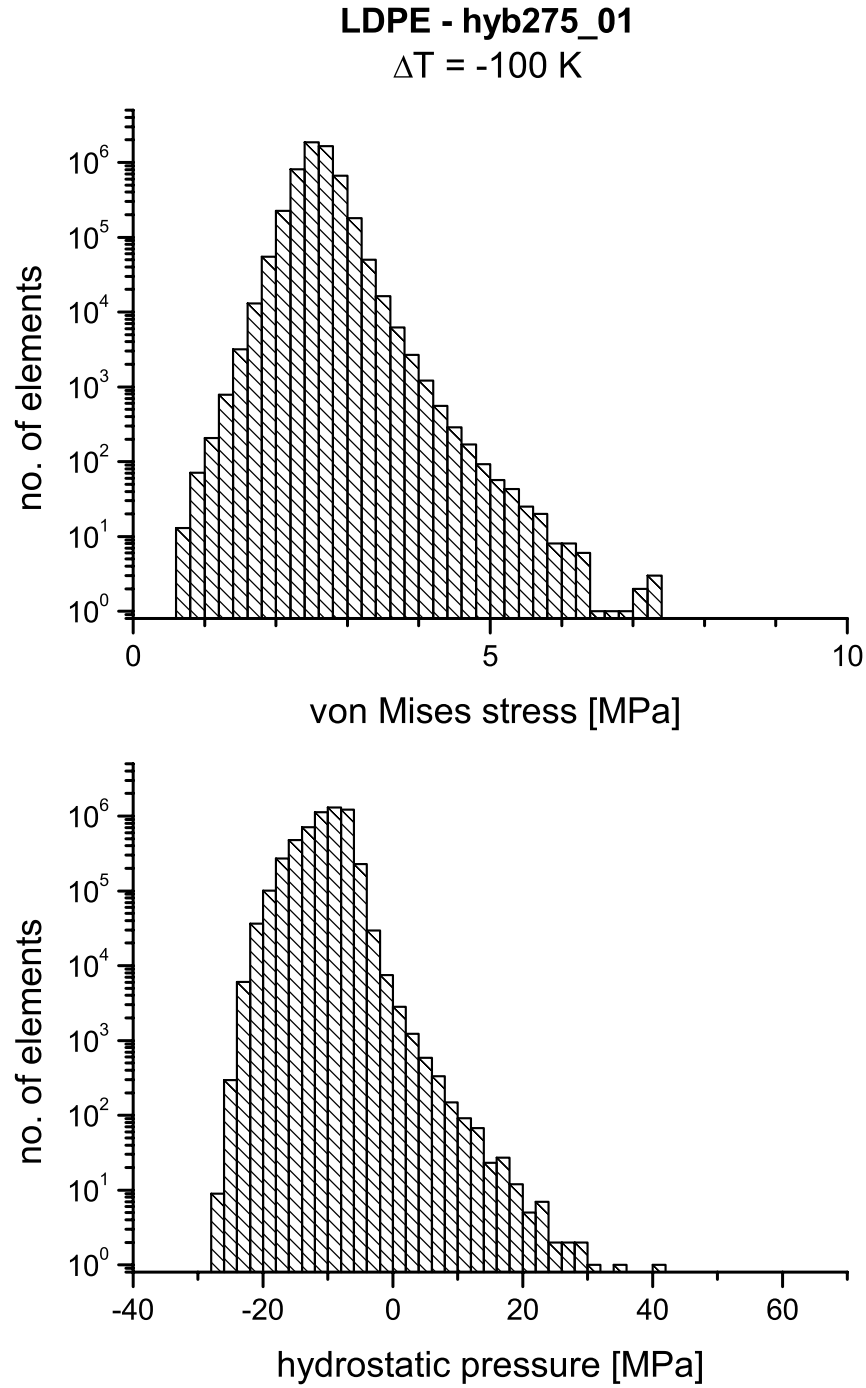
ΔT = -100 K

Figure 7.11: Local thermal stresses occuring in the LDPE phase of sample hyb275_01 from a temperature change of $\Delta T = -100$K. Distribution of local von Mises stress (top) and local hydrostatic pressure (bottom). The total number of elements is 5'529'900.
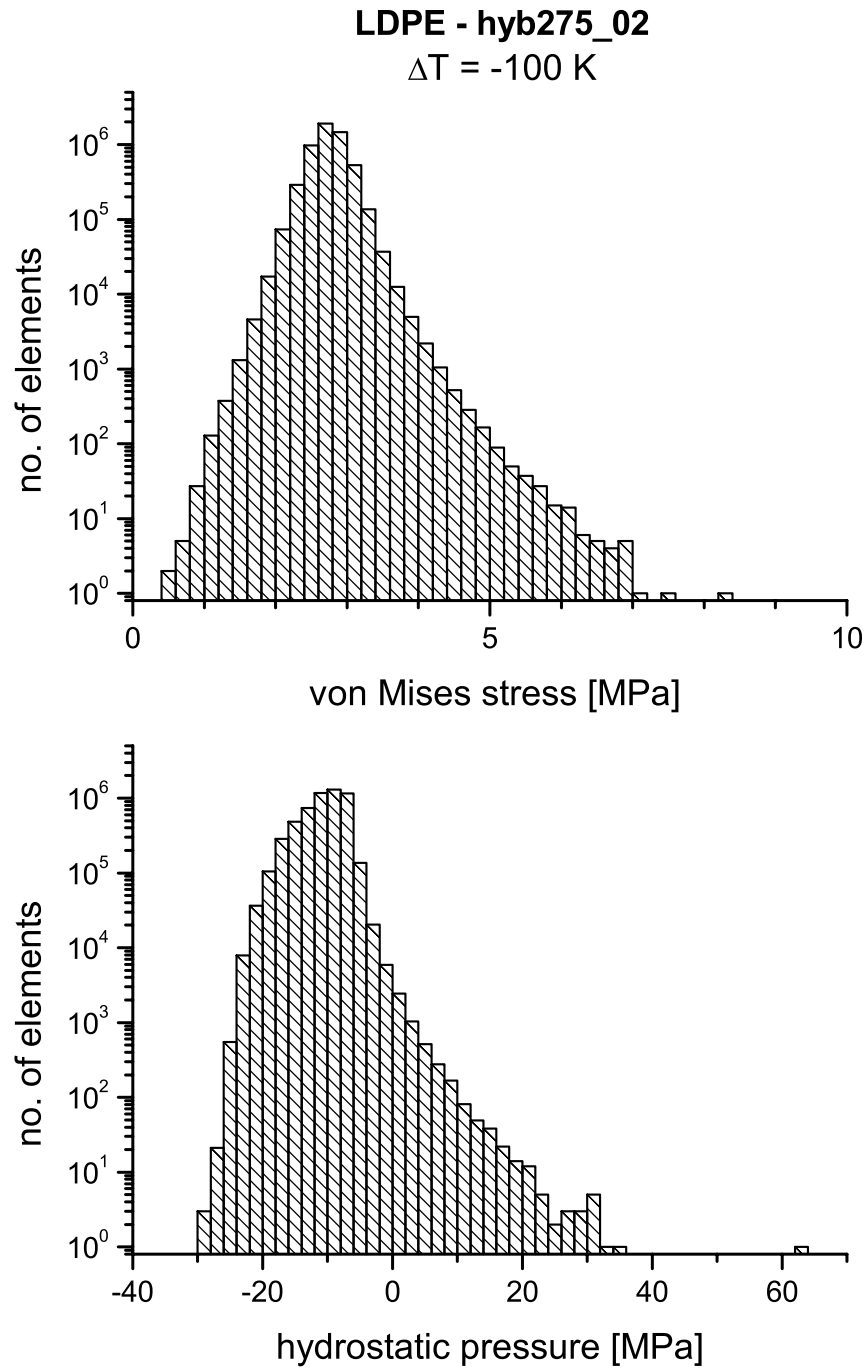
Figure 7.12: Local thermal stresses occuring in the LDPE phase of sample hyb275_02 from a temperature change of $\Delta T = -100$K. Distribution of local von Mises stress (top) and local hydrostatic pressure (bottom). The total number of elements is 5'461'397.

Figure 7.13: Local thermal stresses occuring in the Pglass phase of sample hyb275_01 from a temperature change of $\Delta T = -100$K. Distribution of local von Mises stress (top) and local hydrostatic pressure (bottom). The total number of elements is 5'470'100.
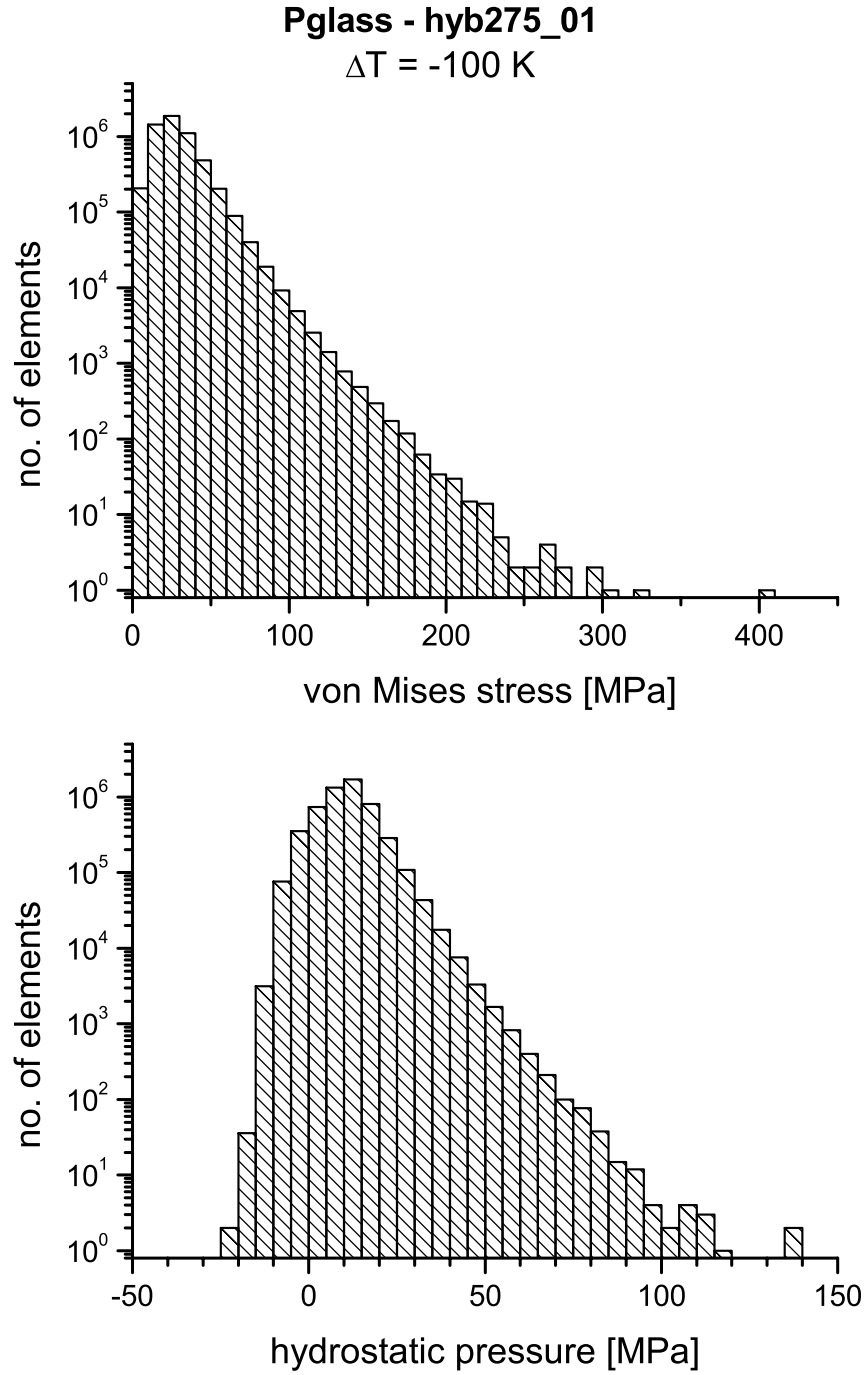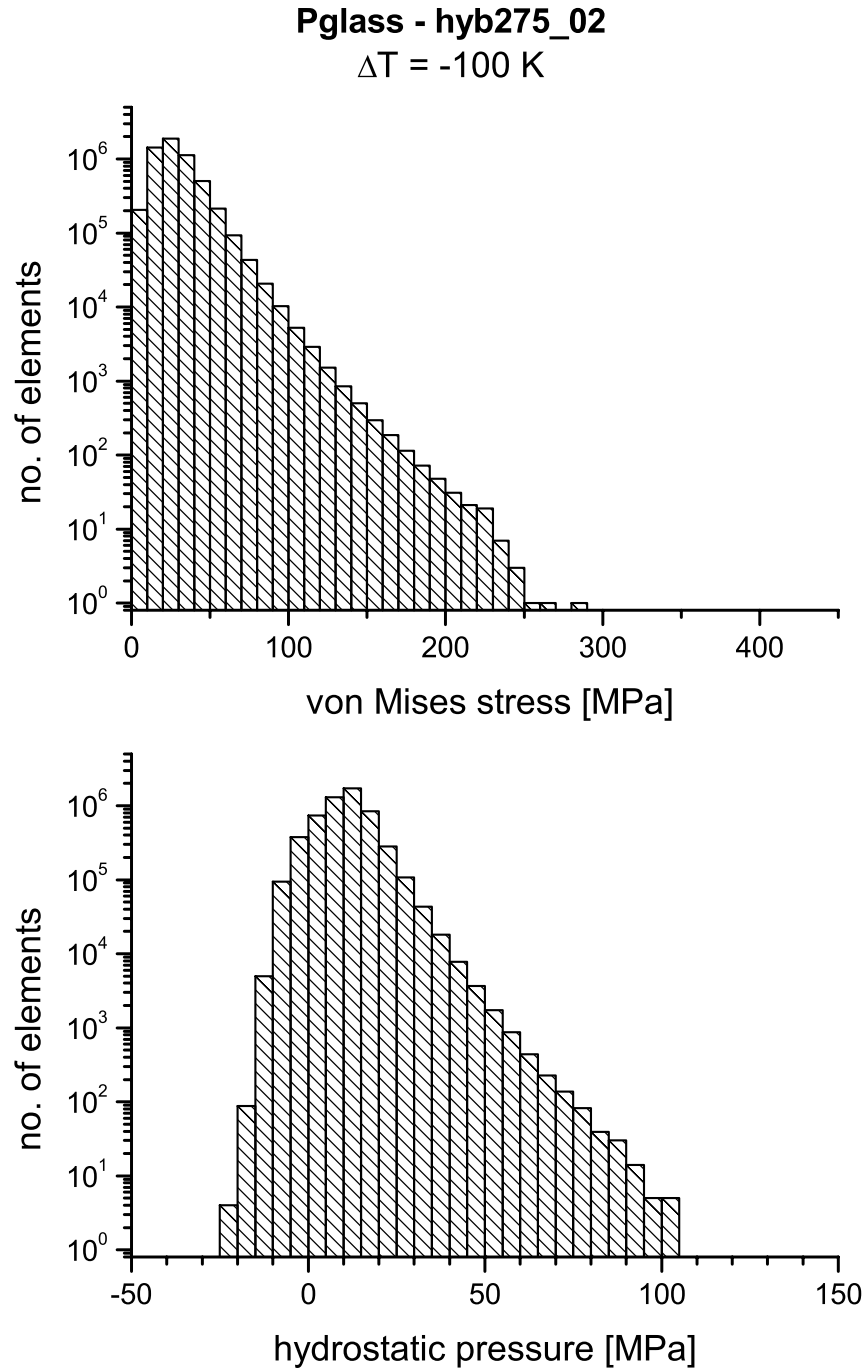
Figure 7.14: Local thermal stresses occuring in the Pglass phase of sample hyb275_02 from a temperature change of $\Delta T = -100$K. Distribution of local von Mises stress (top) and local hydrostatic pressure (bottom). The total number of elements is 5'538'603.

The numerically predicted stiffness of the hybrid is in the range that one would also expect from micro-mechanical models. However, this is six times higher than the experimentally observed stiffness of real samples. It is assumed that this discrepancy originates in some kind of damage that occurs upon cooling of the material from the melting / glass transition temperature to room temperature. The difference in thermal expansion coefficient leads to local stresses in the material which were analyzed. It was seen that high stresses occur only in a very small fraction of all elements but can reach levels that may well induce damage in the brittle Pglass.

A cascade process started by generating cracks in some elements could cause the failure of significantly more elements. However this cannot be seen in the 'static' analysis we did here.

8 Graphite/Aluminium Composites

Light metal infiltrated graphite composites exhibit an interpenetrating network type of microstructure. The co-continuous microstructure is intrinsic to the manufacturing process where porous graphite preforms are pressure infiltrated with an aluminium melt. The graphite / aluminium (C/Al) composites have a number of properties that make them good candidates for certain specific applications. Some of their major advantages are the low density, low coefficient of thermal expansion (CTE), and the temperature resistance of the carbon material. The metal phase is providing fracture toughness and improved thermal conductivity. Further assets are the electrical conductivity and self lubricating properties of the composite.

Prospective applications of such a composite material can be found in the transportation industry. The use is planned as piston material for internal combustion engines where a significant reduction in fuel and oil consumption can be expected. Another possible application is as current collectors for electrical locomotives.

C/Al composites have been studied in collaboration with Thomas Etter and Prof. Peter Uggowitzer of the Laboratory of Metal Physics and Technology at ETH Zürich. The material is studied in a European project involving materials manufacturers and the automotive industry. Extensive information can be found in the PhD thesis of Thomas Etter [88].

In the present thesis X-ray microtomography data was used to build a computer model of one such C/Al composite. The electrical conductivity and elastic properties of the material were then studied in the as produced state and after a cyclic thermal treatment. Conductivity degradation after the thermal treatment was investigated [22].

8.1 Composite Preparation

Graphite/aluminium (C/Al) composites with interpenetrating topology can be produced by the infiltration of a porous graphite preform with liquid aluminium alloys [89]. Due to the poor wettability between aluminium and graphite, external pressure is necessary to force the liquid metal into the preform. A short contact time between the melt and preform is a prerequisite to avoid the formation of detrimental carbides. This requires high pressure and fast cooling

rates, and can be achieved in practice by using the Indirect Squeeze Casting Process [90].

As a starting material an isotropic polycrystalline porous graphite with an open porosity of about 14.5 vol.-% was used as preform. These preforms were produced by cold isostatic pressing of special mesophase powders, subsequent controlled thermal decomposition and final high temperature treatment. Preforms were provided by Schunk Kohlenstofftechnik GmbH.

The porous preforms were infiltrated with a hypoeutectic AlSi7Ba (7 wt.-% Si, 0.25 wt.-% Ba) alloy. The addition of surface-active elements such as barium to the AlSi7 base alloy should facilitate the infiltration by lowering the surface tension of the liquid alloy. [91] The superheated aluminium melt (750℃) was pressed into preheated graphite preforms (680℃) with a hydraulic plunger and solidified under a pressure of about 75 MPa. By using a moderate preform temperature and a fast cooling rate, the formation of Al_4C_3 could be avoided. Infiltration work was done at LKR Ranshofen, Austria.

8.2 Experimental Material Characterization and Properties

A four-probe method was used by Etter to measure electrical conductivities [92]. In this method, a direct current is passed through the specimen between the outer probes. The resulting potential difference is measured between the inner probes.

Mechanical properties were measured in a 3-point bending test by Etter.

X-ray microtomography measurements were performed at the Materials Science Beamline [76] of the Swiss Light Source, Paul Scherrer Institut, Villigen, Switzerland using a monochromatic beam energy of 10 keV. The field of view (FOV) was 1.4 mm, and 1001 projections over an angle of 180 degrees were measured. The individual 2-D tomograms were reconstructed by a filtered backprojection procedure. The resulting effective size of the digital volume element (voxel) was $0.7 \times 0.7 \times 0.7 \, \mu m^3$. Tomography measurements and image reconstruction were done by Peter Wyss of EMPA Dübendorf, Switzerland.

Some properties of the studied C/Al composite are summarized in Table 8.1.

8.3 Electrical Conductivity and Representative Volume Element (RVE)

Fig. 8.1 a/b show typical optical micrographs of the C/AlSi7Ba composite, and Fig. 8.1 c/d show corresponding 2 D tomogram slices. As can be seen from the

Table 8.1: Experimental material properties. Thermophysical and mechanical properties of the monolithic phases and the corresponding composite: electrical conductivity σ_{el}, thermal conductivity λ, linear thermal expansion coefficient α(average over the range 100℃- 300℃), density ρ, four-point bending strength σ_c, and fracture toughness K_{IC} (n.d. not determined).

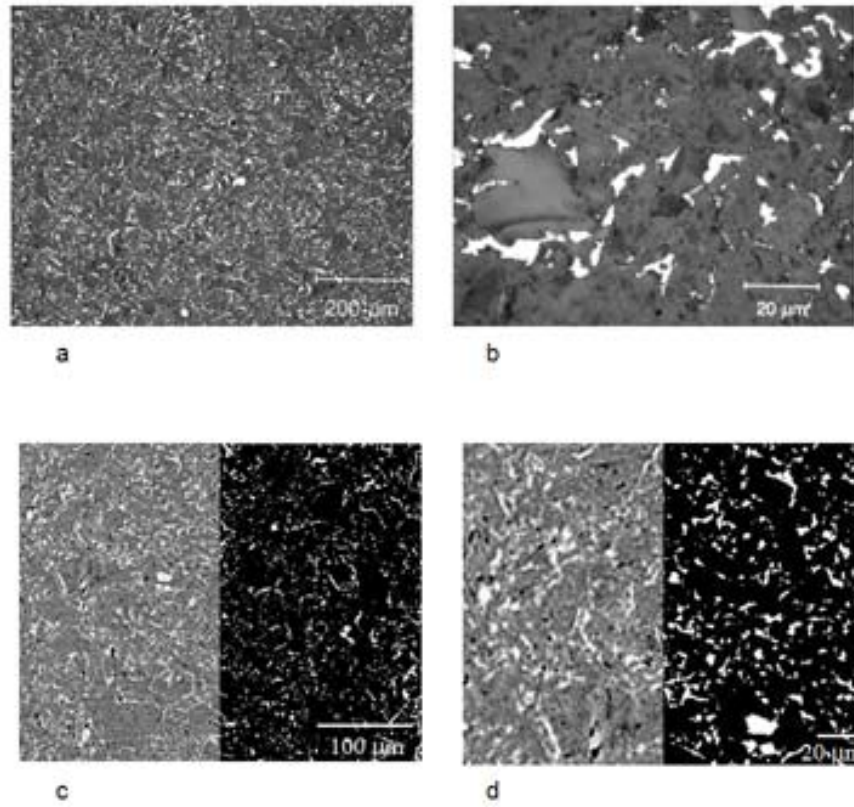|	Graphite preform	AlSi7Ba	C/Al composite
σ_{el} [$10^6/\Omega m$]	0.043 ± 0.001	24 ± 1	0.53 ± 0.03
λ [W/mK]	49 ± 1	183 ± 2	76 ± 2
α [$10^{-6}/K$]	6.39 ± 0.05	22.4 ± 0.4	9.1 ± 0.3
ρ [g/cm^3]	1.83	2.69	2.17
σ_c [MPa]	61 ± 2	n.d.	122 ± 5
K_{IC} [MPam$^{1/2}$]	0.94 ± 0.03	n.d.	1.93 ± 0.03

optical micrographs, the bright metal phase fills the pores homogeneously. The residual porosity as determined by mercury porosimetry was less than 1 vol.-%.

A segmentation procedure was used to assign each voxel (effective voxel size $0.7 \times 0.7 \times 0.7 \, \mu m^3$) of the tomography images to one of the three specific phases (graphite, aluminium, or pores) according to its grey level. Since there were no clear, high-contrast distinctions between the grey levels of the different phases, the segmentation was carried out according to a combination of visual judgement and the additional constraint that the porosity of the graphite preform as measured by mercury porosimetry is 15 vol.%. Therefore the volume contents of aluminium and pores should sum up to 15 vol.%. The right-hand sides of Fig. 8.1 c/d show examples of image segmentation where the aluminium phase is represented in white. In the next step the segmented images were used to create a 3-D finite element model directly, by mapping each voxel to one cubic finite element and assigning to it the corresponding phase conductivity value (Fig. 8.2).

The effective electrical conductivity of the composite was calculated by solving Laplace's equation with a position dependent, piecewise uniform local electrical conductivity $\sigma(\mathbf{r})$

$$\text{div}\sigma(\mathbf{r})\text{grad}\phi = 0 \tag{8.1}$$

on a cubic grid of serendipity family linear brick finite elements [2, 24]. In the direction in which the conductivity was determined, a zero potential on one side and that of unity on the opposite side was applied. In the two perpendicular directions periodic boundary conditions were used. An iterative Krylov subspace solver [25] was used and the effective composite properties were extracted by using a linear response relation between the volume averaged fluxes and the external potentials. In this study, we used computer models with up to about

Figure 8.1: Microstructure of the C/Al composite. **a/b**, Optical micrographs of C/AlSi7Ba composite (grey - graphite, white - aluminium, black - pores), and **c/d**, 2-D tomogram slices and Al segmentation of C/AlSi7Ba composite, pixel size 0.7μm. The brighter phase corresponds to aluminium (approx. 15 vol.-%).
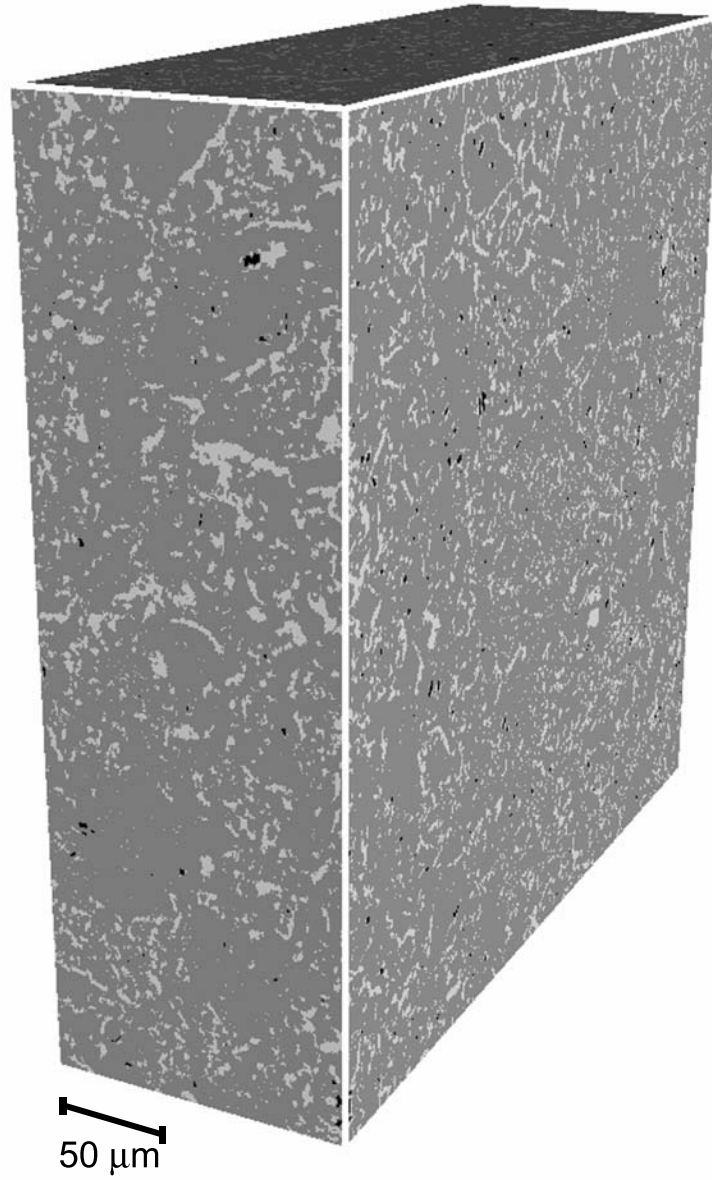
Figure 8.2: 3-D view of the finite element model. The microstructure was reconstructed from 3-D X -ray microtomography data and segmented into three phases. The volume has a size of $600 \times 600 \times 200$ voxels of a size of $0.7 \times 0.7 \times 0.7 \mu\mathrm{m}^3$ (dark grey - graphite, light grey - aluminium, black - pores).

10^8 elements. Typically, the CPU time needed for solving one model was a few hours on a single processor of an HP Superdome with PA8600 processors (clock rate 550 MHz).

The electrical conductivity as measured was $\sigma_{Al} = 24 \cdot 10^6/\Omega\text{m}$ for the bulk aluminium and $\sigma_{meas} = 0.043 \cdot 10^6/\Omega\text{m}$ for the porous graphite preform. For the numerical calculations, however, the conductivity of the dense graphite, σ_0 , rather than that of the porous graphite preform σ_{meas}, needs to be known. Unfortunately, the former cannot be measured directly. To circumvent this problem we used an alternative, reconstruction approach. We first made an initial estimate by using a linear mixing rule

$$\sigma_{meas} = \sigma_0(1 - f) \tag{8.2}$$

where f is the volume fraction of pores. This value was then refined in a series of auxiliary numerical calculations. For this, all aluminium containing voxels in the computer models considered were replaced by pores, i.e. elements with a zero electrical conductivity. A graphite phase conductivity value was then sought that would yield the correct conductivity for the porous preform. The correct value for dense graphite was found to be $0.053 \cdot 10^6/\Omega\text{m}$.

Hashin-Shtrikman variational bounds establish rigorous upper and lower bounds on the effective electrical conductivity $\langle\sigma\rangle$ of macroscopically isotropic composites with an arbitrary microstructure [93]

$$\sigma_1 + \frac{f}{\frac{1}{\sigma_2 - \sigma_1} + \frac{1-f}{3\sigma_1}} \leq \langle\sigma\rangle \leq \sigma_2 + \frac{1 - f}{\frac{1}{\sigma_1 - \sigma_2} + \frac{f}{3\sigma_2}} \tag{8.3}$$

where σ_1 is the electrical conductivity of the matrix, σ_2 is the electrical conductivity of the inclusion phase and f is the volume fraction of the inclusion phase. However, due to the large difference in electrical conductivity between the phases of more than two orders of magnitude these bounds are far apart in a simplified two phase system consisting of a graphite matrix and 15 vol.-% aluminium inclusions, which was considered here as a model system, i.e. $0.08 \cdot 10^6/\Omega\text{m}$ for the lower bound and $2.49 \cdot 10^6/\Omega\text{m}$ for the upper bound (indicated by dashed lines in Fig. 8.3).

When estimating effective material properties by numerical simulation techniques, it is imperative to identify the representative volume element (RVE) of that material, i.e. the volume that is sufficiently large to be representative of the material on a macroscopic scale. It has been shown, both theoretically [36] and numerically [1], that for composite materials with isolated inclusions (spheres, platelets etc.) the RVE is surprisingly small. We demonstrate this by applying the finite element procedure to a series of microstructures composed of different numbers of non-overlapping identical aluminium spheres randomly distributed

in a graphite matrix (1, 8, 27, 64, and 343 spheres respectively with an inclusion volume fraction $f = 0.15$). In an additional study it was clearly established that a resolution of 120^3 elements results in well converged numerical predictions for five different random microstructures of 64 spheres. For the different system sizes studied, the grid dimensions were chosen to result in the same number of elements per sphere diameter. Since the conductive inclusions do not percolate, the predicted electrical conductivities are quite close to the lower Hashin-Shtrikman bound (Fig. 8.3 b). But more remarkably, the individual estimates converge very rapidly to a single value, representative of the effective electrical conductivity of the macroscopic composite. Even for microstructures containing 27 spheres (grid size: 90^3 elements), the relative standard deviation of the 15 individual predictions is only 2 %, and with 64 spheres (grid size: 120^3 elements) the relative standard deviation is less than 1 %.

However, it is not immediately evident whether or not this remarkable feature would also pertain to interpenetrating composite materials. To elucidate this problem numerically, we randomly chose a certain number of subvolumes (typically ten for a given length scale) of predefined sizes (25^3, 50^3, 100^3, 200^3 voxels), out of the whole $200 \times 600 \times 600$ voxel microstructure measured, and numerically predicted the effective electrical conductivity of these subvolumes. The estimates obtained for individual models showed a rather large scatter (Fig. 8.3a). As one can estimate from Fig. 8.3a, the numerical predictions would tentatively converge only for very large simulation models of about 10^9 to 10^{10} elements. Such calculations are impractical at the moment, due to the current CPU time and memory limitations. A possible suggestion might be that by orientation averaging of the predictions for different directions one might improve the convergence behaviour. We found a small improvement with the smallest microstructures, but almost none with the larger ones.

Our results indicate that it is at present impossible to make rational numerical predictions for interpenetrating C/Al composites based on a single microstructure of a size that is still computationally manageable, since one would merely obtain a random result without any significance for the macroscopic effective properties of the material. However, as seen in Fig. 8.3, the ensemble average over the individual predictions obtained on a particular length scale converges remarkably rapidly to the experimentally measured conductivity value, already for very small, computationally tractable computer models.

It can be observed that all the individual predictions lie within the two Hashin-Shtrikman bounds, but for the smallest simulation cells (25^3 voxels) the largest and the lowest predicted values differ by a factor of about 15. This clearly demonstrates that it is impossible to achieve accurate predictions based on a single microstructure.

We have demonstrated that, because of the large representative volume element size, it is not sufficient to base material property predictions of interpene-
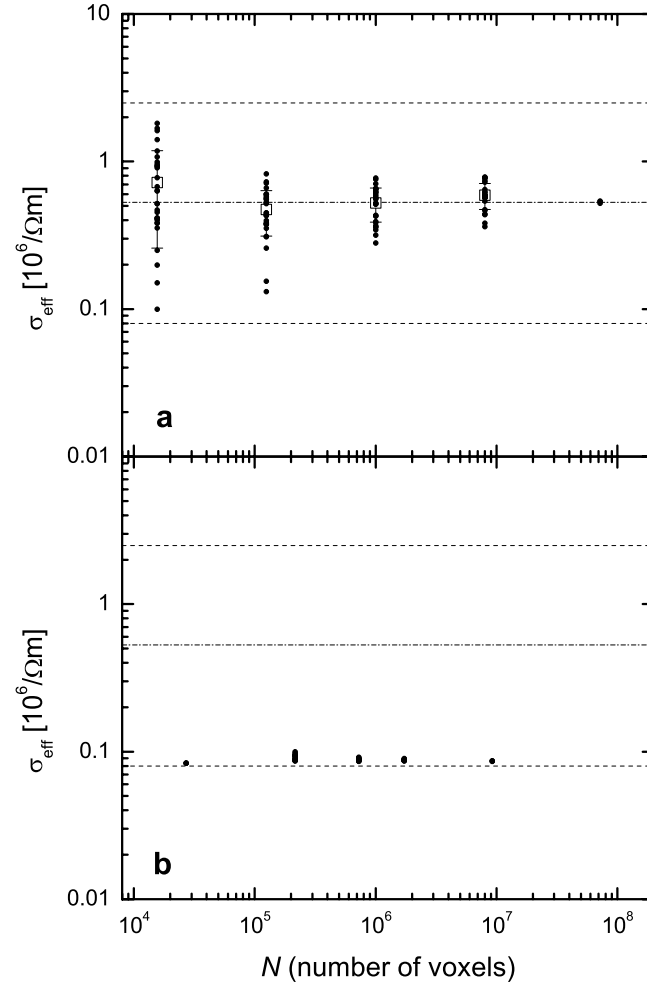
Figure 8.3: Numerical results. Predicted electrical conductivity depends on the size of the simulation cell dots represent individual numerical predictions, black open squares are the respective ensemble averages over the individual numerical predictions, error bars are calculated as the standard deviation, the dash-dot line is the experimentally measured conductivity $\sigma = 0.53 \cdot 10^6/\Omega\mathrm{m}$, the dashed lines show the upper and lower Hashin-Shtrikman bounds). In the interpenetrating C/Al composite **a**) the convergence towards the effective electrical conductivity of the macroscopic material is very slow, i.e. the representative volume element is extremely large, whereas for random microstructures of nonoverlapping spheres **b**) this convergence is much faster (1, 8, 27, 64, and 343 spheres).

trating phase composites on a single moderately sized simulation cell. However, despite the highly different conductivities of the phases, remarkably accurate predictions can nonetheless be achieved by carrying out ensemble averaging over a sufficient number of small models. This opens a pathway to studying the influence of microstructural changes, which can readily be simulated in the computer models, on the effective physical properties (electrical conductivity, thermal conductivity, dielectric constants) of such interpenetrating composites. Hence, it will in time be possible to optimise the topology of composites in such a way that certain desired properties may be obtained.

8.4 Electrical Conductivity of Thermally Aged Composites

For the planned use of the C/Al composites in internal combustion engines it is important to know about the behaviour of the composite material under a cyclic thermal load. Experimentally this was tested by applying 1000 cycles of heating the test sample from room temperature to 300℃ and cooling down to room temperature again in ambient air.

It was observed that the the electrical conductivity of the aged composite, is $\sigma_{age} = 0.43 \pm 0.03 \cdot 10^6/\Omega$m. This is about 20% lower as compared to the conductivity of the composite in the original state, $\sigma_{meas} = 0.53 \pm 0.03 \cdot 10^6/\Omega$m.

We asked the question whether this experimentally observed effect can be reproduced also in the simulation. To this end a sample of the same C/Al composite was thermally cycled as described above. Subsequently, microtomographic measurements were made under the same conditions and in the same measuring shift as the original sample.

The images were segmented as for the first sample assuming that the volume fraction of Aluminium was equally 14.5%. An ensemble of ten non-overlapping subvolumes with a size of 100^3 voxels was randomly chosen out of the total sample volume. For these 10 subvolumes the electrical conductivity was numerically calculated. The same phase properties as determined in Sec. 8.3 have been used.

Fig. 8.4 compares the predicted conductivities before and after the thermal cycling. The conductivity drops from $0.52 \cdot 10^6/\Omega$m to $0.45 \cdot 10^6/\Omega$m, which corresponds to a decrease of 13% from the original value is observed in the thermally treated sample.

Although the effect in the simulation is not as well expressed as it was observed experimentally, one can see a trend in the same direction. Naturally, one would ask what are the reasons for this effect. Possible explanations are that some of the aluminium channels break because of the difference in thermal expansion coefficient between the graphite and the aluminium and are therefore no langer

available for conducting the electrical current. Another reason, which has a somewhat similar effect, might be that pores develop within the aluminium phase or existing pores aggregate. This would equally reduce the conducting cross-sections of the aluminium channels or interrupt some of them.

Experimentally, it was observed that after the thermal cycling the length of the composite samples had increased by 0.1%. Most probably this increase in length results from a increase in volume of the sample.

By using the numerical method it should be tested whether newly occurring void spaces in the aluminium network are responsible for the observed decrease in the conductivity. The potential defects were "healed" in the model by replacing all pore elements by aluminium. As a control the same procedure was also applied to the model of the original composite (without thermal treatment).

The results of this procedure are presented in Fig. 8.5. The original composite (before TC) exhibited only a very small increase of the conductivity from the state with pores to the state where all the pores were filled with aluminium. To our surprise, however, the thermally cycled composite (after TC) was able to regain almost the same electrical conductivity as the original sample.

Indeed, it was possible to simulate a "healing" of the damage which occurred through the thermal cycling of the composite. This demonstrates that some kind of porosity in the aluminium phase is responsible for the decrease in the electrical conductivity. In the composite without thermal cycling, in contrast,
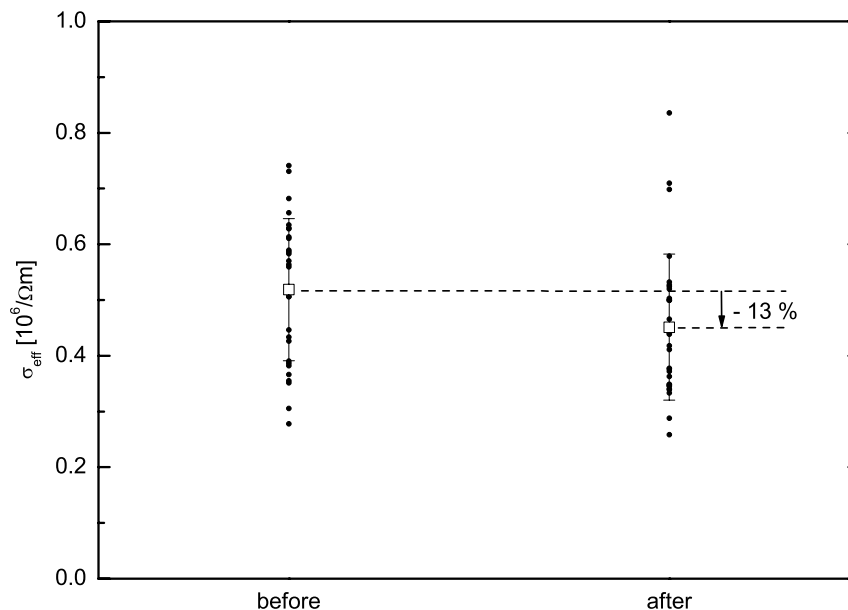
Figure 8.4: Electrical conductivity σ_{eff} of C/Al composite before and after thermal cycling. A decrease of 13% is observed.
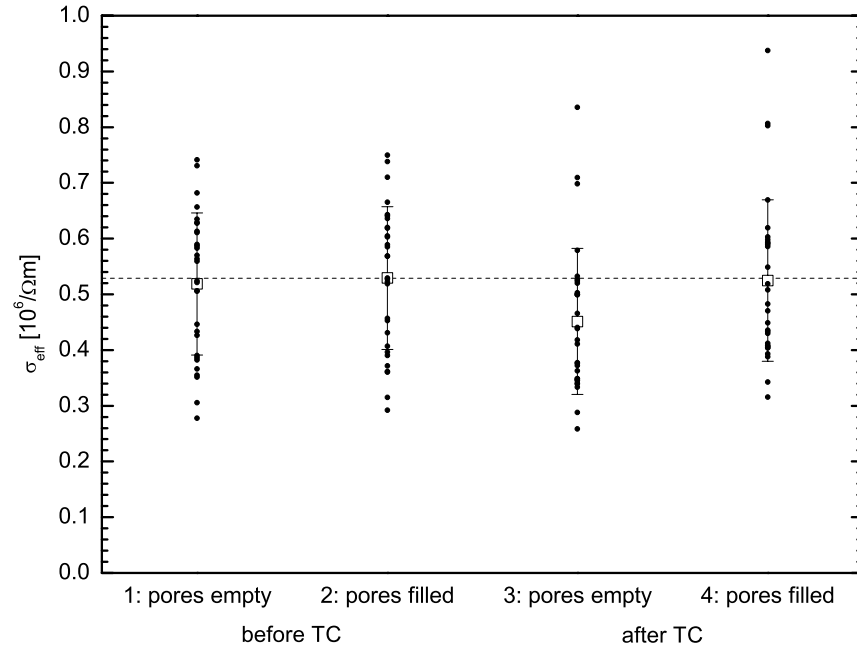
Figure 8.5: Filling the pores with aluminium results in a recovery of the initial electrical conductivity of the thermally cycled sample (right hand side, after TC). The conductivity of the untreated sample remains unchanged (left hand side, before TC).

Table 8.2: Elastic properties of the phases used for the finite element calculations. Young's modulus E, Poisson ratio ν, linear thermal expansion coefficient α, and density ρ.

	graphite	aluminium
E [GPa]	12.8	72.0
ν	0.18	0.33
α [10^{-6}/K]	6.2	20.4

the remaining pores are mainly closed pores. They do not contribute to the overall effective conductivity of the composite even when they are filled with aluminium.

8.5 Elastic Properties

In this section the numerical prediction of the effective elastic properties of the C/Al composites is discussed. The elastic properties of the two phases that were used for the calculations are summarized in Table 8.2.

The effective stiffness tensor of subvolumes of different size was numerically calculated with the finite element method described in Ch. 2. The subvolumes were of a size of 25^3, 50^3, 100^3, and 200^3, respectively. Numerical predictions for ten subvolumes of each size were made (nine subvolumes for 200^3).

In Fig. 8.6 the individual predictions for the effective Young's modulus for a deformation in the x-, y-, and z-direction are plotted against the number of elements of the simulation cell. The mean and the standard deviation are also plotted in this figure.

It is observed that the predictions for the Young's modulus converge quite fast. Already for a model size of 100^3 elements the scatter is very small (standard deviation 4%). The predicted Young's modulus converges to a value of 17.3 GPa.

As compared to the calculations of the effective electrical conductivity (Sec. 8.3), the convergence is much faster here. Other than with the electrical conductivity, where the values of the two phases differ by more than two orders of magnitude, the difference is much smaller here, i.e. a factor of six in the Young's modulus and about 1.5 in the Poisson's ratio. For this reason the effective properties of the composite seem to be less sensitive to small changes in the volume fraction of aluminium or the exact morphology of the metal channels.

From Fig. 8.6 it is obvious that a number of subvolumes with a size of 100^3 will give well converged predictions for the effective elastic properties of this
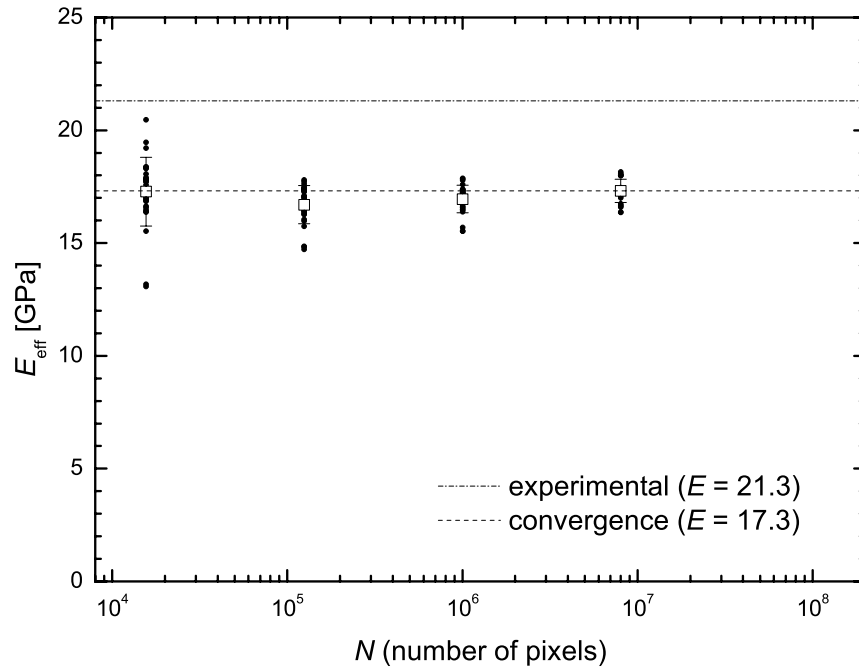
Figure 8.6: Individual numerical predictions of Young's modulus of subvolumes plotted vs. the number of elements (black dots). The mean (open boxes) and standard deviations (error bars) are indicated.

composite.

However, the absolute value of the predicted stiffness $E = 17.3\,\mathrm{GPa}$ is about 20% smaller than the experimentally measured $E = 21.3\,\mathrm{GPa}$ (determined in a three-point bending test).

The numerical prediction of the effective Young's modulus after thermal cycling based on ten subvolumes of 100^3 elements does not show any significant deviation from the value before thermal cycling (Fig. 8.7). This finding is in accordance with the experimental findings of Etter [88].

8.5.1 Elastic Properties of Model Structures

In order to better understand the achievable range of elastic properties in graphite-aluminium composites the elastic properties of some simple model structrures have been studied where the phase properties were the same as for the real C/Al composites (see Table 8.2). For the case of a lamella and of unidirectional cylinders (fibres), respectively, reliable bound estimates for the elastic properties of the composites exist. These solutions are compared to numerical calculations for the same model structures and to numerical results for the real composite structure based on the tomography data and to the experimentally
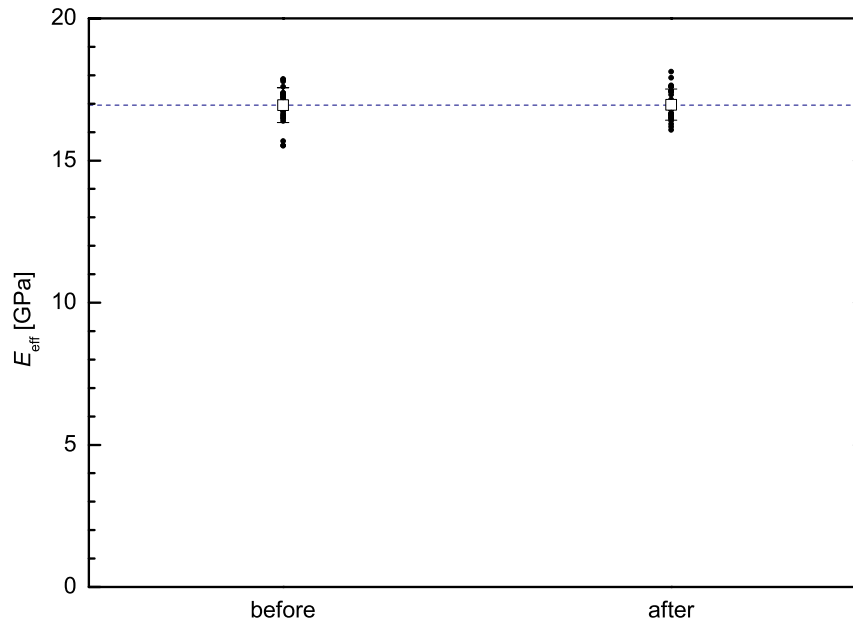
Figure 8.7: Virtually no change in the numerically predicted Young's modulus before and after thermal cycling. Based on ten subvolumes of 100^3 elements. Black dots are individual predictions, open squares are the arithmetic mean, and error bars are calculated as standard deviation.

Table 8.3: Upper and lower bounds on the effective stiffness E_{eff} of C/Al composites with a aluminium volume fraction of $f_{Al} = 0.15$. Values in GPa.

	E_{up}	E_{low}
Voigt-Reuss	21.7	14.6
Hashin-Shtrikman	18.5	15.8

measured values.

For the cases of a lamella and of parallel cylinders in the direction of the cylinder axis or in the plane of the lamella the so-called Voigt average modulus can be used. The effective modulus of the composite E_{eff} can then be written as

$$E_{eff} = f_i E_i + (1 - f_i) E_m \qquad (8.4)$$

where f_i is the volume fraction of the inclusions, E_i is Young's modulus of the inclusions and E_m is Young's modulus of the matrix.

In the perpendicular direction(s) the so-called Reuss average is given as

$$\frac{1}{E_{eff}} = \frac{f_i}{E_i} + \frac{1 - f_i}{E_m} \qquad (8.5)$$

With an aluminium volume fraction of $f = 0.15$ and the phase properties of Table 8.2 upper and lower bounds can be calculated (Table 8.3).

8.5.2 Numerical Predictions for Model Structures

For an aluminium lamella (Fig. 8.8, aluminium volume fraction $f = 0.15$) the numerical procedure predicts a stiffness of $E_{11} = 14.9$ GPa in the direction perpendicular to the plane of the lamella and of $E_{22} = E_{33} = 21.8$ GPa in the two in-plane directions. Orientation averaging of this prediction gives a value of $E = 17.6$ GPa for an isotropic material. For aluminum cylinders parallel to the z-axis (Fig. 8.9, $f = 0.15$) the modulus in the two perpendicular directions is numerically predicted as $E_{11} = E_{22} = 15.5$ GPa, while in the direction parallel to the cylinders the modulus is $E_{33} = 21.8$ GPa.

In these two cases the results of the numerical method are within the bounds. Furthermore two types of 3-D connected inclusions have been investigated. First, a simple cubic inclusion network with quadratic cross section was used as model structure (Fig. 8.10, $f = 0.156$). This forms an interpenetrating network with the matrix. The numerically predicted modulus for this structure is $E_{11} = E_{22} = E_{33} = 18.4$ GPa. Orientation averaging of the elasticity tensor shows that a comparable isotropic material would have a Young's modulus
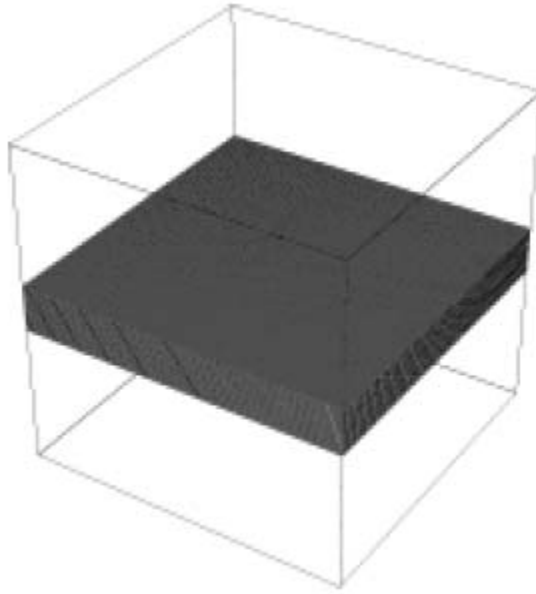
Figure 8.8: Model structure: lamella ($f = 0.15$).
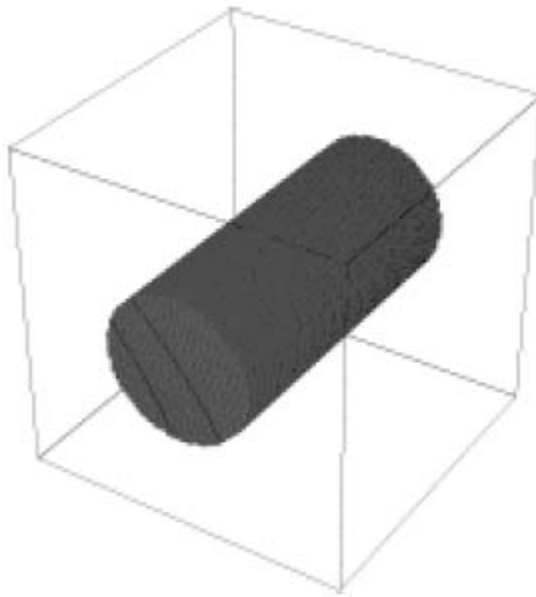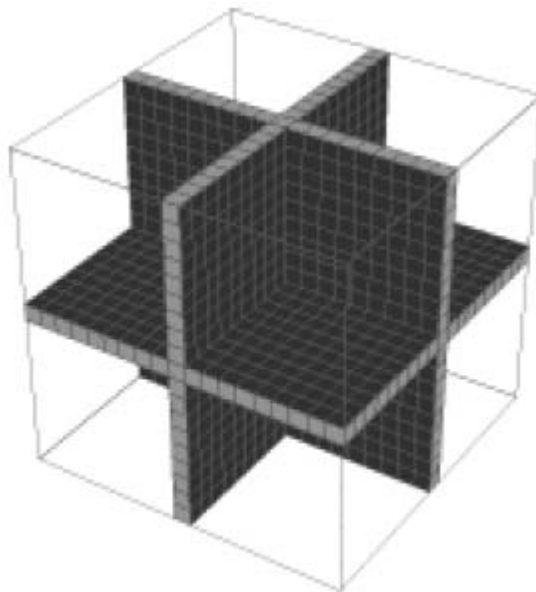

Figure 8.9: Model structure: cylinder ($f = 0.15$).

of $E = 17.2$ GPa. Second, a model structure consisting of three intersecting lamellae (Fig. 8.11, $f = 0.150$) has a numerically predicted stiffness of $E_{11} = E_{22} = E_{33} = 19.8$ GPa.
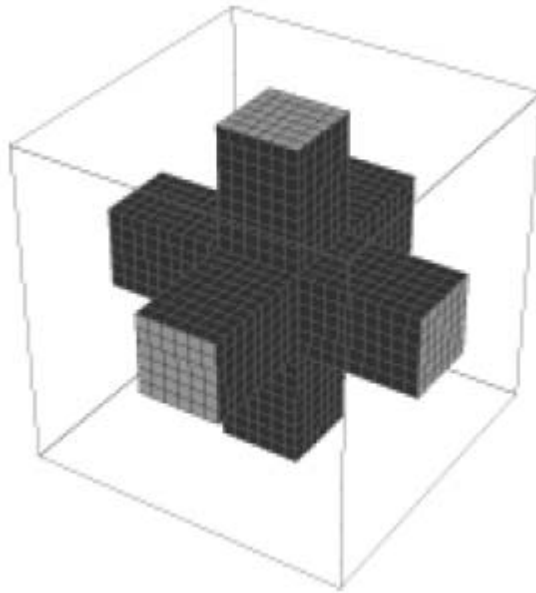
Figure 8.10: Model structure: simple cubic network ($f = 0.156$).

Figure 8.11: Model structure: intersecting lamellae ($f = 0.15$).

Table 8.4: Results of parameter study. Dependence of E_{eff} and ν_{eff} on E_{Graph} and ν_{Graph} was studied.

		ν_{Graph}					
		0.10		0.20		0.30	
	11.0	15.09	0.15	14.96	0.21	15.07	0.29
E_{Graph}	12.8	17.08	0.14	16.94	0.21	17.02	0.29
	15.0	19.45	0.15	19.29	0.22	19.39	0.29

8.5.3 Parameter Study

The determination of the elastic properties of the dense graphite is not straightforward. Experimentally only the properties of the porous graphite preforms can be measured. For the numerical calculations, however, the properties of the dense material are needed. We relied on the linear mixing rule $E_{porous} = (1 - p)E_{dense}$, where p is the volume fraction of the pores, to determine the Young's modulus of the dense graphite. It is not clear whether this method gives an accurate value for E_{dense}.

The Poisson's ratio of the dense graphite was estimated from literature values.

Because of the uncertainty connected to these two materials properties we investigated their influence on the composite properties. To this purpose a parametric study was done where the Young's modulus and the poissons ratio of the dense graphite were varied independently. For E_{Graph} values of 11.0, 12.8, and 15.0, and for ν_{Graph} values of 0.10, 0.20, and 0.30 were chosen, resulting in a matrix of 9 different combinations of parameters. The effective composite properties (E and ν) of one subvolume of the measured microstructure with a size of 100^3 elements were calculated with these parameter combinations (Table 8.4).

From the results in Table 8.4 it can be observed that the Poisson's ratio of the graphite, ν_{Graph}, influences the effective Poisson's ratio of the composite, ν_{eff}, i.e. ν_{eff} increases linearly with ν_{Graph}. A regression analysis showed that $\nu_{eff} = 0.07 + 0.72 \cdot \nu_{Graph}$ (correlation coefficient $R = 0.997$).

However, ν_{Graph} has only a very small effect on the effective Young's modulus of the composite E_{eff}. For $\nu_{Graph} = 0.20$ the resulting E_{eff} is slightly smaller than for the two other values, but the effect is negligible.

The ν_{eff} is unaffected by a change of E_{Graph} from 11.0 GPa to 15.0 GPa. E_{eff} depends linearly on E_{Graph} following the relation $E_{eff} = 3.13 + 1.08 \cdot E_{Graph}$ (correlation coefficient $R = 0.999$).

From the above we see that within the limits tested ($11.0 \leq E_{Graph} \leq 15.0$ and $0.1 \leq \nu_{Graph} \leq 0.3$) we can expect reasonable effective Young's modulus

even with an uncertainty in the Poisson's ratio of the graphite.

8.5.4 Discussion of Model Calculations

For the cases of aluminium lamellae and parallel cylinders the numerical predictions coincide well with the upper and lower bounds that were analytically calculated by the Voigt and Reuss average respectively. This shows that the result of the numerical procedure are accurate in principle. For inclusions that are connected in all three spatial dimensions the numerical procedure predicts equal moduli in all three directions that lie well between upper and lower bound as one would expect.

The stiffness numerically calculated for the real structure ($E_{eff} = 17.3$ GPa) is close to the value predicted for the simple cubic interpenetrating network ($E_{11} = E_{22} = E_{33} = 18.4$). In fact, orientational averaging of the stiffness tensor of this model structure gives a Young's modulus for an isotropic material of $E = 17.2$ GPa. Comparing this to the numerical prediction for the real structure measured by microtomography ($E_{eff} = 17.3$ GPa) indicates that the real microstructure is almost elastically isotropic. Surprisingly, the experimentally measured stiffness of the composite ($E_{eff} = 21.3$ GPa) is about 25 % higher than we would expect from the numerical prediction. It coincides basically with the upper (Voigt) bound (Table 8.3). This result is not well understood considering the other data since one would always expect, that for an isotropic "reinforcement" the stiffness is lower than the upper bound, which holds for unidirectional reinforcement.

The discrepancy observed might be due to inaccurate measurements of the composite stiffness. But more probable is the explanation that the phase properties used for the calculations (Table 8.2) are somewhat inaccurate. The stiffness of the graphite could not be measured directly. Therefore some uncertainty is connected with the value used. Furthermore, one should also think about the possibility that the aluminium alloy in the narrow channels may have a stiffness that is different from its bulk value.

8.6 Thermal Conductivity and Thermal Expansion Coefficient

The thermal conductivity of the porous preform and of the C/Al composite was calculated for ten subvolumes of $100 \times 100 \times 100$ voxels. The model of the porous preform was constructed by changing all metal containing elements in the composite to pore elements.

Predicted thermal conductivities (Fig. 8.12)show a relatively narrow distribution and are in reasonable accordance with the experimentally measured values.

The thermal expansion coefficient was numerically calculated for a number of subvolumes of the C/Al composite. Subvolumes were of different size, i.e. 25^3, 50^3, 100^3, and 200^3 voxels.

As compared to the experimentally measured value of $\alpha = 9.1 \cdot 10^{-6}\mathrm{K}^{-1}$ the numerical predictions are slightly too high (Fig. 8.13). This is due to the fact that stiffness values are predicted too low as compared to the measured value. The numerically calculated stiffness directly enters the calculation of the thermal expansion coefficient.

8.7 Discussion

The microstructure of C/Al composite with 15 vol.% metal content has been imaged by X-ray microtomography. The tomography data has been used to directly build a finite element model of the microstructure. Based on this model the effective electrical and heat conductivity as well as effective mechanical properties (Young's modulus and coefficient of thermal expansion) of the composite have been numerically predicted.

The predicted electrical conductivity values showed a wide scatter for different subvolumes of the sample. This lead to the conclusion that the representative
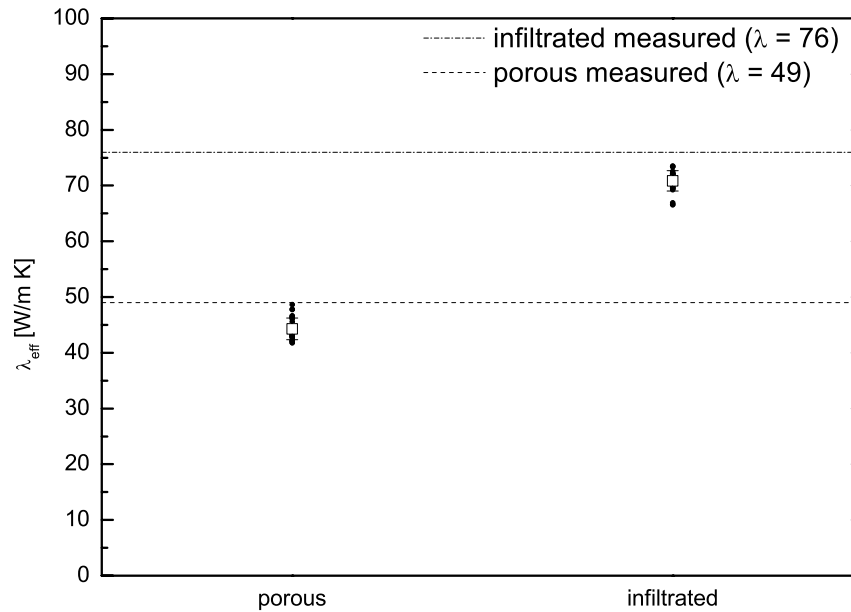
Figure 8.12: Thermal conductivity of the porous graphite preform and the C/Al composite. Numerical predictions for ten individual subvolumes of $100 \times 100 \times 100$ voxels, average and standard deviation are shown.
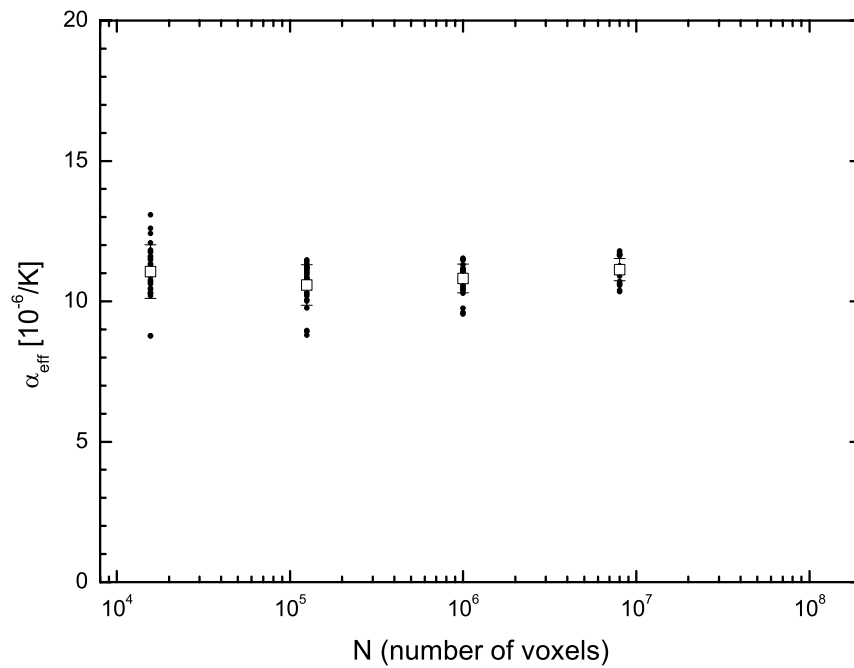
Figure 8.13: Thermal expansion coefficient of C/Al composite for subvolumes of 25^3, 50^3, 100^3, and 200^3 voxels. Numerical predictions for individual subvolumes, averages, and standard deviations are shown. The experimental value is $9.1 \cdot 10^{-6} \mathrm{K}^{-1}$.

volume element (RVE) of this kind of composites is very large for the electrical conductivity. However, we were able to show that the ensemble average over a sufficiently large number of subvolumes allows to make very accurate predictions of the effective electrical conductivity of the composite which are in very good accordance with the experimentally measured values.

The decrease of the electrical conductivity of the composite after thermal cycling which was observed experimentally could be well reproduced by the numerical procedure although not to its full extent.

For the Young's modulus and the thermal expansion coefficient good predictions have been achieved, however, the numerical predictions are not as accurate here as for the electrical conductivity. The convergence of the individual predictions is faster for the elastic properties. In order to understand the reasons for the discrepancy between the experimental and the numerical results some simple model structures have been investigated but a conclusive explanation has not been found.

9 Conclusions and Outlook

In the first part of this thesis the accuracy of direct numerical predictions for the thermoelastic properties of short fibre reinforced materials has been demonstrated. The often applied model of Halpin-Tsai has been shown to be systematically less accurate than the Tandon-Weng (Qiu-Weng) model. The Tandon-Weng model in turn is relatively accurate with glassy polymer matrices but less accurate for lower stiffness semi-crystalline matrix materials. For (anisotropic) carbon fibres the Qiu-Weng predictions are considerably less accurate than the corresponding predictions of the Tandon-Weng model for (isotropic) glass fibres.

We have shown that the following approach can deliver accurate as well as fast property predictions for short fibre composites with any arbitrary fibre orientation state. First, direct numerical finite element calculations are used to predict the properties of unidirectional composites. Subsequently, a fast arithmetic orientation averaging is applied to account for the (local) fibre orientation. This process is fast enough to be implemented into a mould filling simulation software that is able to predict the local fibre orientation and therefore, applying the scheme described above, also the local elastic properties of the short fibre reinforced composite.

In the second part, it has been been shown in this work that the principle of using 3D tomography data of composite materials to directly build 3D computer models is feasible. With such models finite element predictions of effective materials properties can successfully performed. It is therefore not necessary to use the cumbersome detour via surface triangulation and unstructured mesh generation.

With the finite element method of Ch. 2 fairly large computer computer models i.e. of a size of $200^3 = 8 \cdot 10^6$ elements can be solved within reasonable time. Some hours to a few days of CPU time are required.

Although the representative volume element (RVE) can be very large in this type of interpenetrating composites it is possible to realize good numerical predictions of the effective properties of the composite. The properties of a sufficiently large number of relatively small models is predicted. The ensemble average over all these predictions has been demonstrated to give a very good estimate for the effective properties of the composite.

Some improvements might be possible with the use of more sophisticated image analysis techniques. This would perhaps facilitate the image segementation and leave less uncertainty in that process.

More detailed statements about the possible damage mechanism in the LDPE/Pglass hybrids could be made if the "static" calculation of thermal stresses would be extended to a "dynamic" modeling of the damage process. With such a method the growth of damages might be simulated. Subsequently it would be possible to calculate the mechanical properties of the simulated damaged structure and to see whether this can reproduce the real damage process.

It would be instructive to extend the study to different microstructures e.g. with other volume contents of metal or a different morphology. A follow-up study with some other types of C/Al composites has been started.

The investigation of the local thermal stresses in the C/Al composites may help to understand the mechanism that leads to the observed degradation of properties of the composite upon thermal cycling.

Guided modification of the microstructure with subsequent property predictions may help to optimize the composite microstructure in order to realize some desired properties.

Bibliography

[1] Gusev, A. A. *J. Mech. Phys. Solids* **1997**, *45*, 1449–1459.

[2] Gusev, A. A. *Macromolecules* **2001**, *34*, 3081–3093.

[3] Gusev, A. A. *Physical Review Letters* **2004**, *93*(3), 034302.

[4] Hine, P. J.; Duckett, R. A.; Davidson, N.; Clarke, A. R. *Compos. Sci. Technol.* **1993**, *47*, 65–73.

[5] Hine, P. J.; Lusti, H. R.; Gusev, A. A. *Compos. Sci. Technol.* **2002**, *62*, 1445–1453.

[6] Lusti, H. R.; Hine, P. J.; Gusev, A. A. *Compos. Sci. Technol.* **2002**, *62*(15), 1927–1934.

[7] Hine, P. J.; Lusti, H. R.; Gusev, A. A. *Compos. Sci. Technol.* **2004**, *64*, 1081–1088.

[8] Gusev, A. A.; Lusti, H. R. *Adv. Eng. Mater.* **2002**, *4*(12), 927–931.

[9] Gusev, A. A.; Heggli, M.; Lusti, H. R.; Hine, P. J. *Adv. Eng. Mater.* **2002**, *4*(12), 931–933.

[10] Gusev, A. A.; Rozman, M. G. *Computational and Theoretical Polymer Science* **1999**, *9*, 335–337.

[11] Gusev, A. A.; Hine, P. J.; Ward, I. M. *Compos. Sci. Technol.* **2000**, *60*, 535–541.

[12] Gusev, A. A.; Lusti, H. R. *Adv. Mater. (Weinheim, Fed. Repub. Ger.)* **2001**, *13*(21), 1641–1643.

[13] Gusev, A. A.; Karmilov, I. A. *Macromol. Theory Simul.* **2002**, *11*(3), 247–249.

[14] Gusev, A. A.; Guseva, O. A. *Adv. Eng. Mater.* **2003**, *5*(10), 713–715.

[15] Lusti, H. R.; Karmilov, I. A.; Gusev, A. A. *Soft Mater.* **2003**, *1*(1), 115–120.

[16] Lusti, H. R. *Property Predictions for Short Fiber and Platelet Filled Materials by Finite Element Calculations;* Diss. ETH No. 15078: Zürich, 2003.

[17] Wissler, M.; Lusti, H. R.; Oberson, C.; Widmann-Schupak, A. H.; Zappini, G.; Gusev, A. A. *Adv. Eng. Mater.* **2003**, *5*(3), 113–116.

[18] Lusti, H. R.; Gusev, A. A. *Modell. Simul. Mater. Sci. Eng.* **2004**, *12*, S107–S119.

[19] Fredrickson, G. H.; Ganesan, V.; Drolet, F. *Macromolecules* **2002**, *35*, 16–39.

[20] Reber, R. *Micro- and Macromechanical Properties of Knitted Fabric Reinforced Composites (KFRC) with Regard to Environmental Exposure;* Diss. ETH No. 13080: Zürich, 1999.

[21] Maire, E.; Buffière, J.-Y.; Salvo, L.; Blandin, J. J.; Ludwig, W.; Létang, J. M. *Adv. Eng. Mater.* **2001**, *3*(8), 539–546.

[22] Heggli, M.; Etter, T.; Wyss, P.; Uggowitzer, P. J.; Gusev, A. A. *Adv. Eng. Mater.* **2005**, *7*(4), 225–229.

[23] *Palmyra 2.5;* MatSim GmbH, Zürich, Switzerland: http://www.matsim.ch.

[24] Zienkiewicz, O. C.; Taylor, R. L. *The Finite Element Method*, Vol. 1: The Basis; Butterworth-Heinemann: Oxford, 5th ed., 2000.

[25] Saad, Y. *Iterative methods for Sparse Linear Systems;* PWS Publishing Co.: Boston, MA, 1996.

[26] *Gridder 1.0;* MatSim GmbH, Zürich, Switzerland: http://www.matsim.ch.

[27] Whiteside, B. R.; Coates, P. D.; Hine, P. J.; Duckett, R. A. *Plastics, Rubbers and Composites* **2000**, *29*(1), 38–45.

[28] Gupta, M.; Wang, K. K. *Polym. Compos.* **1993**, *14*(5), 367–382.

[29] VerWeyst, B. E.; Tucker III, C. L.; Foss, P. H.; O'Gara, J. F. *Intern. Polymer Processing* **1999**, *XIV*(4), 409420.

[30] Kallien, L. H.; Steinbach, J. In *18. CAD-FEM Users' Meeting*, Friedrichshafen, 2000.

[31] Camacho, C. W.; Tucker III, C. L.; Yalvaç, S.; McGee, R. L. *Polym. Compos.* **1990**, *11*(4), 229–239.

[32] Tucker III, C. L.; Liang, E. *Compos. Sci. Technol.* **1999**, *59*(5), 655–671.

[33] Takao, Y.; Taya, M. *J. Compos. Mater.* **1987**, *21*, 140–156.

[34] Halpin, J. C.; Jerine, K.; Whitney, J. M. *J. Compos. Mater.* **1971**, *5*, 36–49.

[35] Eduljee, R. F.; McCullough, R. L. In *Structure and Properties of Composites*; Chou, T. W., Ed., Vol. 13 of *Materials Science and Technology;* VCH: Weinheim, 1993; page 625.

[36] Drugan, W. J.; Willis, J. R. *J. Mech. Phys. Solids* **1996**, *44*(4), 497–524.

[37] Davidson, N. C.; Clarke, A. R.; Archenhold, G. *J. Microsc.* **1997**, *185*(2), 233–242.

[38] Bubb, S. L. *PhD thesis;* University of Leeds, 2001.

[39] Allan, P. S.; Bevis, M. J.; Gibson, J. R.; May, C. J.; Pinwell, I. E. *Journal of Materials Processing Technology* **1996**, *56*, 272–281.

[40] Clarke, A. R.; Davidson, N.; Archenhold, G. A. In *Micro '90 Conference*, pages 305–308, London, UK, 1990. Adam Hilger Ltd., Boston.

[41] *Palmyra 2.3;* MatSim GmbH, Zürich, Switzerland: http://www.matsim.ch.

[42] Ito, T.; Suganuma, T.; Wakashima, K. *J. Mater. Sci. Lett.* **1999**, *18*, 1363–1365.

[43] Christensen, R. M. *Mechanics of Composite Materials;* Krieger Publishing Company: Malabar, Florida, reprint ed., 1991.

[44] Eshelby, J. D. *Proc. R. Soc. London, A* **1957**, *241*(1226), 376–396.

[45] Mori, T.; Tanaka, K. *Acta. Metall.* **1973**, *21*(5), 571–574.

[46] Tandon, G. P.; Weng, G. J. *Polym. Compos.* **1984**, *5*(4), 327–333.

[47] Qiu, Y. P.; Weng, G. J. *International Journal of Engineering Science* **1990**, *28*(11), 1121–1137.

[48] Halpin, J. C. *J. Compos. Mater.* **1969**, *3*, 732.

[49] Russell, W. B. *Z. Angew. Math. Phys.* **1973**, *24*(4), 581–600.

[50] Hill, R. *J. Mech. Phys. Solids* **1971**, *11*(1), 129.

[51] Cook, A. H. PhD thesis, University of Leeds, **1997**.

[52] Tucker III, C. L.; Advani, S. G. In *Flow and Rheology in Polymer Composites Manufacturing*; Advani, S. G., Ed., Vol. 10 of *Composite Materials Series;* Elsevier: Amsterdam, 1994.

[53] Lee, Y. H.; Lee, S. W.; Youn, J. R.; Chung, K.; Kang, T. J. *Materials Research Innovations* **2002**, *6*, 65–72.

[54] Advani, S. G.; Tucker III, C. L. *J. Rheol.* **1987**, *31*(8), 751–784.

[55] Babuska, I.; Szabó, B. In *The Mathematics of Finite Elements and Applications*; Whiteman, J. R., Ed.; Wiley: New York, 1997.

[56] Halpin, J. C.; Pagano, N. J. *J. Compos. Mater.* **1969**, *3*, 720.

[57] Levin, V. M. *Mech. Tverd. Tela* **1968**, *88*, 25.

[58] Goussev, O. A.; Peter, R.; Rozman, M. G.; Gusev, A. A. *Journal of Applied Physics* **2000**, *88*(7), 4013–4016.

[59] Gusev, A. A.; Slot, J. J. M. *Adv. Eng. Mater.* **2001**, *3*(6), 427–429.

[60] Baeurle, S. A.; Fredrickson, G. H.; Gusev, A. A. *Macromolecules* **2004**, *37*(15), 5784–5791.

[61] Radon, J. *Berichte Sächsische Akademie Wissenschaften* **1917**, *69*, 262–277.

[62] Hounsfield, G. N. *A Method of and Apparatus For Examination of a Body by Radiation Such as X or Gamma Radiation;* Great Britain Patent 1283915, 1972.

[63] Elliott, J.; Dover, S. *J. Microsc.* **1982**, *126*, 211–213.

[64] Müller, R.; Matter, S.; Neuenschwander, P.; Suter, U. W.; Rüegsegger, P. *Mater. Res. Soc. Symp. Proc.* **1997**, *461*, 217–223.

[65] Spanne, P.; Thovert, J. F.; Jacquin, C. J.; Lindquist, W. B.; Jones, K. W.; Adler, P. M. *Physical Review Letters* **1994**, *73*(14), 2001–2004.

[66] Mees, F.; Swennen, R.; van Geet, M.; Jacobs, P. In *Applications of X-ray Computed Tomography in the Geosciences*; Mees, F., Swennen, R., van Geet, M., Jacobs, P., Eds., Vol. 215 of *Special Publications;* Geological Society: London, 2003; pages 1–6.

[67] Anderson, S. H.; Wang, H.; Pleyton, R. L.; Gantzer, C. J. In *Applications of X-ray Computed Tomography in the Geosciences*; Mees, F., Swennen, R., van Geet, M., Jacobs, P., Eds., Vol. 215 of *Special Publications;* Geological Society: London, 2003; pages 135–149.

[68] Schneebeli, M.; Sokratov, S. A. *Hydrol. Process.* **2004**, *18*, 3655–3665.

[69] Al-Raoush, R. I.; Willson, C. S. *Journal of Hydrology* **2005**, *300*, 44–64.

[70] Flisch, A.; Lüthi, T.; Zollikofer, C.; Ponce de León, M. In *ASNT Industrial Computed Tomography Topical Conference*, Huntsville, AL, 1996.

[71] Lüthi, T.; Flisch, A.; Wyss, P. *Insight* **1998**, *40*(3), 196–197.

[72] Peix, G.; Duvauchelle, P.; Freud, N. In *X-Ray Tomography in Material Science*; Baruchel, J., Buffière, J.-Y., Maire, E., Merle, P., Peix, G., Eds.; Hermes Science Publications: Paris, 2000; pages 15–27.

[73] Kak, A. C.; Slaney, M. *Principles of Computerized Tomographic Imaging;* IEEE Press: New York, 1988.

[74] Feldkamp, L. A.; Davis, L. C.; Kress, J. W. *J. Opt. Soc. Am.* **1984**, *1*(6), 612–619.

[75] Stampanoni, M. *A novel approach towards hard X-ray submicrometer computer tomography with synchrotron radiation;* Diss. ETH Nr. 14884: Zürich, 2002.

[76] Stampanoni, M.; Borchert, G.; Wyss, P.; Abela, R.; Patterson, B.; Hunt, S.; Vermeulen, D.; Rüegsegger, P. *Nuclear Instruments & Methods in Physics Research, Section A: Accelerators, Spectrometers, Detectors, and Associated Equipment* **2002**, *491*(1), 291–301.

[77] Stampanoni, M.; Borchert, G. L.; Abela, R.; Patterson, B.; Vermeulen, D.; Rüegsegger, P.; Wyss, P. *Acta Phys. Pol., B* **2002**, *33*(1), 463–469.

[78] Baruchel, J.; Boller, E.; Cloetens, P.; Ludwig, W.; Peyrin, F. In *X-Ray Tomography in Material Science*; Baruchel, J., Buffière, J.-Y., Maire, E., Merle, P., Peix, G., Eds.; Hermes Science Publications: Paris, 2000.

[79] *SLS webpage;* http://sls.web.psi.ch/view.php/beamlines/index.html, 30.05.2005.

[80] *ImageJ 1.31v;* National Institutes of Health, USA: http://rsb.info.nih.gov/ij/.

[81] Tischendorf, B. C.; Harris, D. J.; Otaigbe, J. U.; Alam, T. M. *Chem. Mater.* **2002**, *14*, 341–347.

[82] Tick, P. A. *Tin-phosphorus oxyfluoride glass containing aromatic organic compound;* United States Patent 4,379,070, 1983.

[83] Adalja, S. B.; Otaigbe, J. U.; Thalacker, J. *Polym. Eng. Sci.* **2001**, *41*(6), 1055–1067.

[84] Adalja, S. B.; Otaigbe, J. U. *Polym. Compos.* **2002**, *23*(2), 171–181.

[85] Morris, B. A.; Vansant, J. D. *The Influence Of Sealent Modulus On The Bending Stiffness Of Multilayer Films;* 30.05.2005.

[86] Hashin, Z.; Shtrikman, S. *J. Mech. Phys. Solids* **1962**, *10*, 335–342.

[87] Hashin, Z.; Shtrikman, S. *J. Mech. Phys. Solids* **1963**, *11*, 127–140.

[88] Etter, T. *Material-physical description of interpenetrating graphite/aluminium composites produced by liquid metal infiltration;* Diss. ETH No. 16096: Zürich, 2005.

[89] Mattern, A.; Huchler, B.; Staudenecker, D.; Oberacker, R.; Nagel, A.; Hoffmann, M. J. *Journal of the European Ceramic Society* **2004**, *24*, 3399–3408.

[90] Long, S.; Beffort, O.; Moret, G.; Thevoz, P. *Aluminium* **2000**, *76*, 82–89.

[91] Lang, G. *Aluminium* **1974**, *50*, 731–734.

[92] Dharmasena, K. P.; Wadley, H. N. G. *J. Mat. Res.* **2002**, *17*, 625–631.

[93] Hashin, Z.; Shtrikman, S. *Journal of Applied Physics* **1962**, *33*, 3125–3133.

Acknowledgments

First of all, I would like to express my greatest gratitude to PD Dr. Andrei Gusev for his personal and scientific support. The discussions with him have been a constant source of scientific inspiration and he let me share his broad scientific experience.

Then I want to thank Prof. Ulrich W. Suter for initially accepting me as his PhD student, for guiding me to a direction of research which suits my interests and for his constant support. Prof. Hans Christian Öttinger I want to thank for accepting me as a member of his research group after the closing of the Suter group. I thank both Prof. Suter and Prof. Öttinger for accepting to be co-referees for this thesis.

I acknowledge the collaboration with the following partners who have contributed their interesting problems and have therefore provided the simulations with a "real life" background: Dr. Peter Hine, University of Leeds, UK, and Dr. Hans Rudolf Lusti, ETH Zürich, in the short fibre composite project, Prof. Joshua Otaigbe and Kevin Urman, University of Southern Mississippi, Hattiesburg, USA, with polymer/Pglass hybrids, and Prof. Peter Uggowitzer and Dr. Thomas Etter, Metal Physics and Technology, ETH Zürich, with infiltrated graphite/aluminium composites.

A number of people have supported this work with their technical expertise and I want to thank them for their help. Peter Wyss, EMPA Dübendorf, has contributed his thorough knowledge and experience in the field of X-ray microtomography. He was responsible for the tomography measurements and the data reconstruction. Gabriel Isman, MatSim GmbH, Zürich, has always immediately responded and efficiently helped when I had any special wishes concerning software. Harald Lehmann and Marc Petitmermet kept the computer infrastructure running. Werner Schmidheiny has helped with sample preparation and Martin Colussi showed me how to make DMTA measurements. From Hans-Ruedi Lusti and Ilya Karmilov I could inherit some useful computer tools.

Furthermore, I would like to thank Christina Graf, Vappu Hämmerli, Patricia Horn, Petra Jans, Diana Surber, and Sylvia Turner for their help with administrative matters.

Many others of the former Suter group and of the Öttinger group and from outside have contributed in some way or another to a good working atmosphere, some with advice some by sharing their lunch time with me, namely Albrecht, André, Aurora, Asja, Brigitte, Christian, Christian, Clarisse, David,

Dennis, Fredy, Helmut, Henrik, Jan, Johannes, Jörg, Jürg, Maged, Marc, Marco, Markus, Martin, Michael, Lera, Pascal, Salvo, Santosh, Silvia, Thomas, Thomas, Trishool, Ulrich, Vikas, Vishwa, Werner - and all those I forgot to mention here.

Christoph, Manfred und Valeska danke ich für ihre Freundschaft und für die ausgezeichnete Küche.

Einen ganz besonderen Dank möchte ich Esther aussprechen, dass sie sich mitgefreut, mitgelitten, mitgeärgert, mich motiviert, gepusht hat – oder was immer jeweils nötig war, während diese Arbeit entstanden ist.

Last, not least, danke ich ganz herzlich meinen Eltern Waltraut und Andreas für ihre Liebe und ihre Unterstützung, wann immer ich sie gebraucht habe, während der letzten 32 Jahre.

Publications

Heggli, M., Etter, T., Wyss, P., Uggowitzer, P.J., Gusev, A.A. *"Aging of Electrical Conductivity in C/Al Interpenetrating Composites: X-ray Microtomography and Numerical Study"*, in preparation.

Heggli, M., Urman, K., Otaigbe, J.U., Gusev, A.A. *"Phase Continuity and Elastic Properties of a Polymer/Phosphate Glass Hybrid"*, in preparation.

Heggli, M., Urman, K., Otaigbe, J.U., Gusev, A.A. *"Numerical Prediction of Potential Gas Barrier Properties of Polymer/Phosphate Glass Hybrids"*, in preparation.

Heggli, M., Etter, T., Wyss, P., Uggowitzer, P.J., Gusev, A.A. *"Approaching Representative Volume Element Size in Interpenetrating Phase Composites"*, Adv. Eng. Mater. **2005**, 7, 225-229.

Heggli, M., Tirelli, N., Zisch, A., Hubbell, J.A. *"Michael-type Addition as a Tool for Surface Functionalization"*, Bioconjug. Chem. **2003**, 14, 967-973.

Gusev, A.A., Heggli, M., Lusti, H. R., Hine, P.J. *"Orientation Averageing for Stiffness and Thermal Expansion of Short Fiber Composites"*, Adv. Eng. Mater. **2002**, 4, 931-933.

Curriculum Vitae

Personal Data

Name	Martin Heggli
Date and place of birth	September 28, 1973 in Luzern, Switzerland
Place of origin	Luzern and Müswangen (LU)
Nationality	Swiss

Education

1980 - 1986	Primary schools in Luzern and Adligenswil (LU)
1986 - 1993	High School: *Realgymnasium*, Kantonsschule Luzern, Luzern
1993	*Matura* Type C
1994 - 2000	Studies in Materials Science at the Swiss Federal Institute of Technology (ETH), Zürich
November 1999 - April 2000	Diploma thesis under the supervision of Dr. N. Tirelli and Prof. Dr. J.A. Hubbell, Institute of Biomedical Engineering, Swiss Federal Institute of Technology (ETH) and University of Zürich, Zürich, Title: *Functionalization of Microspheres for Biomedical Applications*

April 2000	Graduation as *Diplom-Werkstoffingenieur ETH*
December 2000 - September 2005	PhD student, Departement of Materials Science, ETH Zürich. Advisor: PD Dr. Andrei A. Gusev

Professional Experience

October 1997 - May 1998	Internship at ABB Corporate Research Ltd., Baden-Dättwil, Subject: *ZnO-Varistor Composites as Surge Arrestors*
July 1998 - August 1998	IAESTE internship at the Institute of Polymer Technology, Technical University of Tampere, Finland, Subject: *Aging of Two-Component Injection Moulded Parts*
March 2000 - June 2000	PC supporter, SWX Swiss Exchange, Zürich
March 2003 - July 2005	Teaching assistant in *Physical Foundations of Materials Science*, *Polymer Physics*, and *Finite Elements in Solids and Structures* courses, Department of Materials, ETH Zürich
December 2000 - September 2005	Research assistant in the groups of Polymer Chemistry and Polymer Physics, ETH Zürich

Awards

1993	*Sidler-Perovic Award* for second best Matura
2000	*SVMT-Award* for best Diploma Thesis (Schweizerischer Verband für Materialtechnik)